Fall 12-21-2019

Removel of Polluntants from Aqueous Solution Via Graphene Oxide/Magnesium Oxide Nanocomposites

Mahdi Heidarizad
Southern Methodist University, mheidarizad@smu.edu

REMOVAL OF POLLUTANTS FROM AQUEOUS SOLUTION VIA GRAPHENE OXIDE/MAGNESIUM OXIDE NANOCOMPOSITES

Approved by:

_____
Prof. Andrew N. Quicksall, Chair
Associate Professor of CEE

_____
Prof. Khaled Abdelghany
Professor of CEE

_____
Prof. John Easton
Senior Lecturer of CEE

_____
Prof. Wenjie Sun
Assistant Professor of CEE

_____
Prof. Jaewook Myung
Assistant Professor of CEE

REMOVAL OF POLLUTANTS FROM AQUEOUS SOLUTION VIA GRAPHENE OXIDE/MAGNESIUM OXIDE NANOCOMPOSITES

A Dissertation Presented to the Graduate Faculty of

Bobby B. Lyle School of Engineering

Southern Methodist University

in

Partial Fulfillment of the Requirements

for the degree of

Doctor of Philosophy

with a

Major in Civil and Environmental Engineering

by

Mahdi Heidarizad

M.S., Tarbiat Modares University, 2010

December 21, 2019

ACKNOWLEDGMENTS

This work could not have been accomplished by the wisdom of my wonderful advisor, Dr. Andrew N. Quicksall, along with his many colleagues in the Department of Civil and Environmental Engineering here at SMU. Also, I would like to thank my former advisor Dr. Sevinc Sengor for the opportunity to perform this research. I am thankful to the members of my PhD dissertation committee, Dr. Khaled Abdelghany, Dr. John H. Easton, Dr. Wenjie Sun, and Dr. Jaewook Myung.

I am also forever grateful to my family, my parents, and my siblings. I owe my deep gratitude to my sweet wife, Nadere for her motivation and hard work.

I am grateful to my friends: Ahmad Bakhtiari, Mahmoud Bakhtiari, Majid Yavari, Majid Heidari, Soheil Mortezaeifar, Ricardo Araujo, Mamdouh Mubarak, Jumana Haj Abed, Anse Danesh, Amir Hossein Zmanian, Farnaz Nourbakhsh, Meysam Akbari, Jafar Ghorbanian, Masoud Mohammadpour, Yasaman Kowsari, Ata Khiabani, Hediye Ashrafi, Hamed Nikfarjam, Laelsadat Badakhshanian, Hossein Zahedi, Nahid Mirzaei, Arefe Safaei, Soheil Sohrabi, Amin Mansourifar, Ali Vafaemehr, Shide Bakhtiari, Pouria Razaghi, Paula Walvoord, Juman Hadad, Rafal Czajkowski, Mohamed Charafeddine, Mahmoud Badi, Areej Bashir, Obada Alhaj, Essa Haddad, Faris Altamimi, Nabeel Khan, Fahed Alhaj, Yukun Cao, Jianing Li, Marziye Badinlou, Ahmad Tayyebi, Mostafa Leili, Bastam Ghanbari, Vahid Jabbari, Anil Koklu, Alper Celebi, Andres Ruzo, Behzad Taheri, Hossein Hashemi, Vahid Sadri, Zara Tayebi, Parisa Farahmand, Amir Kiaee, Masoud Harooni.

Heidarizad, Mahdi M.S., Tarbiat Modares University, Tehran, 2010
B.S., Shahid Beheshti University, Tehran, 2006

Removal of Pollutants from Aqueous Solution via Graphene Oxide/Magnesium Oxide Nanocomposites

Advisor: Professor Andrew N. Quicksall

Doctor of Philosophy conferred December 21, 2019

Dissertation completed August 19, 2019

In this study, a series of graphene oxide/magnesium oxide nanocomposites (GO/MgO NCs) were synthesized and applied for the removal of Methylene Blue (MB) from aqueous solutions. The prepared NCs were characterized using scanning electron microscopy, transmission electron microscopy, X-ray diffraction, X-ray photoelectron spectroscopy, and thermogravimetric analysis. The results showed that MgO particles were successfully layered on GO. The impacts of different experimental variables on the removal of MB including GO/MgO NCs dosage, pH, contact time, and initial MB concentration were investigated.

Thereafter, we investigated the mechanism and kinetics of ozonation processes in the presence of GO/MgO NCs as a catalyst for the degradation of phenol. The generation of reactive oxygen species such as hydroxyl radicals ($^{\bullet}OH$) and singlet oxygen ($^1O_2$) was studied during catalytic ozonation using tert-butyl alcohol and sodium azide as radical scavengers. The mechanism of phenol degradation under catalytic ozonation and reaction pathways were studied.

Finally, we studied response surface methodology (RSM) coupled with a central composite design (CCD) to investigate process parameters affecting the removal of phenol in ozonation processes using GO/MgO NCs as a catalyst. Analysis of variance (ANOVA) was performed to determine the significant differences between the independent variables.

TABLE OF CONTENTS

LIST OF FIGURES

LIST OF TABLES

This is dedicated to my parents and my wife.

CHAPTER 1

Introduction

Wastewaters from industries can be toxic and negatively affect human and environmental health [1]. A variety of physical, chemical and biological methods are available for eliminating contaminants from wastewater [2–5]. Among these technologies, adsorption is commonly used because of its low cost, simple operation and design requirements, and low residual product generation [1,6]. In the last few years, nanomaterials, as a new adsorbent, has been investigated for the removal of different pollutants from water and wastewater, such as dyes, metals and metalloids, antibiotics, microbial pollutants, pharmaceuticals and phenolic compounds [7–9]. Various organic dyes are aromatic compounds which are used in different industrial fields [10]. These dyes are soluble in water; therefore, they can easily partition to the aqueous environment and, as a result, cause many environmental and health hazards [11].

Recently, new carbonaceous adsorbents have received the most attention due to their high adsorption capacity. Graphene is one of the most interesting advanced carbon-based nanomaterials with a two dimensional honeycomb sp^2 carbon lattice, large theoretical surface area (2630 m^2/g), good chemical stability, high transparency, large electron mobility, high thermal conductivity and remarkable elasticity [12–16]. Therefore, graphene is considered a favorable material for various applications such as sensors, transistors, catalysis, and environmental pollution treatment [17–20]. Graphene oxide (GO) is a single sheet form of graphite with a high specific surface area which contains various oxygenated surface functional groups [21]. These functional groups lead to the negative surface charge, hydrophilicity and easy dispersion of GO in aqueous solutions [22]. These

properties make GO a great candidate for the removal of different pollutants by adsorption. Due to its high surface area and functionalities, GO can be used as an excellent platform to grow various nanoparticles.

In this study, first, we synthesized a new nano-composite as an adsorbent for adsorption of dye from wastewater. We synthesis graphene oxide from graphite powder and modified it with magnesium oxide (MgO). The characteristics of the new nano-adsorbent were investigated by different methods. Thereafter, we used methylene blue (MB) as an organic dye to study the adsorption ability of GO/MgO NCs in a set of experiments. We investigated:

- If MgO can improve GO adsorption capacity
- How pH can affect adsorption of MB by GO/MgO NCs
- Effect of different experimental conditions on the removal of MB
- GO/MgO adsorption capacity compared to other GO-based adsorbents
- And isotherms and kinetics of the adsorption of MB by GO/MgO NCs

On the other hand, some organic compounds, because of their characteristics or low efficiency of the adsorption, are poorly removed by adsorption processes. Due to a high degradation efficiency for various classes of organic compounds, simplicity of application and functionality at atmospheric temperature and pressure, advanced oxidation processes (AOPs) have been considered to be viable and promising alternatives to other technologies for removal of toxic compounds [23]. For an AOP, highly reactive radicals (mainly $^{\bullet}OH$) are generated; these molecules can oxidize organic compounds into inorganic final products and/or to less toxic and more biodegradable intermediates. Hence, an AOP is considered an efficient and flexible technique for the treatment of toxic wastewaters.

During the past two decades, several AOPs have been developed and investigated for use in the water and wastewater treatment industry [24,25]. In these processes, reactants such as ozone are the main active species for oxidizing organic contaminants to dominantly, carbon dioxide and water [26]. Ozonation alone, however, is relatively slow and can hinder AOPs practical application [27]. To overcome this problem, several attempts for process modification have been assessed in the literature. Catalytic ozonation, including heterogeneous and homogeneous catalytic ozonation, are developed to ameliorate ozonation performance by the generation of reactive oxygen species (ROS) [28–32].

A variety of catalysts have been developed for catalytic ozonation such as activated carbon, metal oxides, and metals on supports [23,33–36]. Recently, new carbonaceous materials, such as graphene, have been the focus of intense research because of their unique characteristics [37].

At the second part of this study, we applied GO/MgO NCs as a catalyst in AOPs for the oxidation of phenol from wastewater. In this part and in a batch set of experiments, we used ozone as an oxidizer and GO/MgO NCs as a catalyst to removal phenol in 100 mL synthesized wastewater that contains 500 mg/L phenol. In this part, we studied:

- If GO/MgO NC is an effective catalyst in the ozonation process for removal of phenol
- Reactive oxygen species generated during the catalytic ozonation process
- How experiment variables can affect the ozonation process
- Mechanism of phenol degradation in catalytic ozonation process and reaction pathways
- Kinetic of degradation of phenol in catalytic ozonation using GO/MgO as a catalyst

In the third part of this study, we investigated the interaction between parameters in the catalytic ozonation of phenol and produce a set of data to analyze and optimize the process. In this

classical experimental design, removal of the phenol in a catalytic oxidation process measured without considering the interaction between parameters that can effect on the phenol removal. Hence, each parameter has been studied individually, which gives less information on the relationship between experimental parameters. In the following study, we evaluate the relationship between independent parameters as a function for the removal of phenol. For this aim, the design of experiments (DOE) combined with response surface methodology apply. DOE gives a meaningful comparison between classical experimental design and statistically designed experiments. DOE is a planned approach for determining cause and effect relationships. DOE helps to reduce the number of experiments or trials and simultaneously change all factors that affect the results. In the last part of this study, our focus can be written as follows:

- Using the design of experiments combined with other technics to design required experiments for modelling and optimization
- Using computer software to analyze the results of experiments
- Statistical techniques apply to generate an empirical model for the phenol removal in the catalytic advanced oxidation process

Finally, we suggest a couple of investigations that can be done in the future using the results of the current study. In the last section of the dissertation, we suggest studying the cost-effectiveness of new nanomaterial production at an industrial scale. Additionally, removal of one or more emerging contaminants from aqueous solution using newly synthesized material would greatly demonstrate the breadth of application.

CHAPTER 2

Synthesis of graphene oxide/magnesium oxide nanocomposites with high-rate adsorption of methylene blue

1.1 Introduction

Wastewaters generated from industrial activity contain a variety of potentially toxic and environmentally harmful compounds. These compounds present an increasingly serious threat to human and environmental health [1]. Organic dyes are aromatic compounds that are commonly used in various fields of industry, such as textile, pulp and paper, printing, food, plastic, and tanneries [10]. These dyes can easily be transported within the aqueous environment because of their high solubility in water, and as a result may pose many serious ecological, environmental, and health hazards [11]. Various conventional methods have been proposed for the removal of dyes from wastewater including physical, chemical, and biological technologies[38–41]. Among the various pollutant-removal technologies, adsorption is the most commonly used due to its low cost, simple operation and design requirements, low residual product generation, and its lack of interaction with toxic substances [1,42]. Recently, nanomaterials, as new adsorbents, have been investigated for the removal of various pollutants from water and wastewater, such as dyes, heavy metals, antibiotics, microbial pollutants, arsenic, pharmaceutical and phenolic compounds [7–9] [9], [10], [11]. Nanomaterials provide enhanced removal efficiencies compared to more traditional adsorbents due to their unique chemical and physical characteristics.

Recently, new carbonaceous adsorbents have received the most attention due to their high adsorption capacity. Graphene is one of the most interesting advanced carbon-based nanomaterials with a two dimensional honeycomb sp^2 carbon lattice, large theoretical surface area (2630 m^2/g), good chemical stability, high transparency, giant electron mobility, high thermal conductivity and

remarkable elasticity [12–16]. Therefore, graphene is considered a favorable material for various applications such as sensors, transistors, catalysis, and environmental pollution treatment [17–20]. Graphene Oxide (GO) is an oxidized derivative of graphene which contains epoxide, hydroxyl, and carboxyl groups [21]. These functional groups lead to the negative charge, hydrophilicity and easy dispersion of GO in aqueous solutions [22]. These properties make GO a great candidate for the removal of different pollutants by adsorption. Due to its high surface area and functionalities, GO can be used as an excellent platform to grow various nanoparticles. In addition, GO helps prevent agglomeration on nanoparticles.

Magnesium oxide (MgO) is an alkaline earth metal oxide with a destructive sorbent, high surface reactivity, high adsorption capacity, and ease of production [10,43]. Recently, MgO nanoparticles (MgO NPs) have been used for the removal of dyes, catechol, phenol, fluoride, and formaldehyde from wastewater [10,11,23,44,45]. Thus, considering the synergistic advantage and decoration of MgO NPs over the GO platform, GO/MgO nanocomposites (NCs) can be considered as a potential adsorbent for the removal of pollutants.

In this paper, for the first time to the best of our knowledge, we synthesized graphene oxide/magnesium oxide nanocomposite adsorbents and demonstrated its application for the successful removal of MB dye from aqueous solutions. We investigated the impact of different experimental conditions on the removal of MB by GO/MgO NCs and discussed the mechanism of MB interaction with the adsorbent.

1.2 Materials and methods

1.2.1 Materials

Graphite powder (< 20 μm, MW: 12.01) was purchased from Sigma-Aldrich. Magnesium Chloride Hexahydrate ($MgCl_2 \cdot 6H_2O$), Sulfuric Acid (H_2SO_4), Hydrochloric Acid (HCl),

Hydrogen Peroxide 30% (H_2O_2), Potassium Permanganate ($KMnO_4$), Sodium Nitrate ($NaNO_3$), Sodium Hydroxide Solution (NaOH) and Methylene Blue ($C_{16}H_{18}ClN_3S$) were obtained from Fisher Scientific. All chemicals used in the experiments were analytical grade.

1.2.2 Preparation of GO

The GO was prepared according to the modified Hummers method [46]. Briefly, 2 g of graphite powder was mixed with 50 mL sulfuric acid (98 wt.%) and 2 g sodium nitrate in a 500 mL flask in an ice bath at 0 °C. While vigorously stirring, 6 g of potassium permanganate was gradually added to the flask, and stirring was maintained for 2 h where after 100 mL of DI water was added to the solution. The solution temperature was rapidly increased to 98 °C and maintained for 30 min. Then 100 mL of deionized water was added and the temperature was increased rapidly to 98 °C and kept for 30 min. 300 mL DI water was then added to the flask. Following that, 20 mL of hydrogen peroxide (30 wt.%) solution was added, causing the color of the mixture to turn to yellow. The mixture was filtered and washed with hydrochloric acid (5%) solution and DI water several times to eliminate any residuals. Ultimately, GO was synthesized by sonication of the dispersion for 60 min and drying at 60 °C.

1.2.3 Preparation of MgO NPs

MgO nanoparticles were synthesized by Sol-gel Method. This method has been successfully used for MgO nanoparticle synthesis and has been proved to be efficient with respect to its simplicity, cost effectiveness and providing unique surface adsorption characteristics [47]. In this study, 100 g of magnesium chloride hexahydrate was dissolved in 500 mL of DI water in a 1 L flask, and 50 mL of sodium hydroxide solution (1 N). The solution was stirred for 4 h to generate the magnesium hydroxide. The solution was then centrifuged (5000 rpm - 7 min) to separate the $Mg(OH)_2$ gel from the suspension. $Mg(OH)_2$ gel was washed a few times with DI

water and dried at 100 °C for 24 h. Finally, MgO nanoparticles were synthesized by calcination at 550 °C for 2 h.

1.2.4 Preparation of GO/MgO NCs

Three different ratios of GO/MgO NCs (5:1, 1:1, and 1:5) were synthesized by impregnation. Briefly, 0.3 g of GO was added in a baker with 300 mL DI water and sonicated for 60 min. Different amounts of Mg oxide nanoparticles (NPs) (i.e., 0.06 g, 0.3 g, and 1.5 g) were added to the dispersion baker. After 30 min of sonication, the suspension was collected by centrifuging and dried at 60 °C.

1.2.5 Preparation of methylene blue (MB) solution

MB has a molecular weight of 319.85 g/mol. It is water-soluble, and blue in color (λ max 664 nm). A standard solution (1000 mg/L) was prepared by dissolving accurately weighed amount of MB in a known volume of DI water. The experimental solutions were prepared by diluting the standard solution of MB with DI water to give the appropriate concentration of the desired solutions.

1.2.6 Characterization

A series of GO/MgO NCs in different ratios (5:1, 1:1, and 1:5) were prepared by the sonication method. The surface morphology of the GO, MgO, and GO/MgO was characterized by scanning electron microscopy (SEM) images by Hitachi S-4800 ultra-high-resolution and transmission electron microscopy (TEM) with an ultrahigh-resolution microscope and an accelerated voltage of 300 kV, a point-to-point resolution of 0.18 nm and a lattice resolution of 0.10 nm. Powder X-ray diffraction (XRD) patterns were obtained by Rigaku Ultima III X-ray diffraction system. The system was configured with a vertical Theta: Theta wide angle goniometer, high intensity Cu x-ray tube (1.54 Å wavelength), and a scintillation counter detector. The scans

were carried on in 2θ with a range of 5° to 80° and 1 s count time per step. Fourier Transform Infrared (FTIR) spectroscopy was used for analysis of chemical bonds from 4000 to 400 cm^{-1} wave number range by using Perkin Elmer Frontier spectrometer at room temperature. X-ray photoelectron spectroscopy (XPS) was performed with PHI 5000™ to determine elements contained in prepared powders and their chemical states. Thermogravimetric analysis (TGA) of GO/MgO NCs was performed with a TA Instrument TGA-SDT 2960 using 10°/min heating rate under 100 mL/min nitrogen gas flow. Chemical stability of GO/MgO NCs was investigated in various pH values (i.e., pH = 1, pH = 3, and pH = 7). For this purpose 0.1 g/L of NCs in different ratios (5:1, 1:1, and 1:5) were dispersed in water solution while stirring with a magnetic stirrer in 125 mL flasks at room temperature. After 2 h, the solution was filtered by 0.2 μm NYL syringe filter. Then, the concentration of Mg ions was measured by colorimetric methods as described previously [48].

1.2.7 Dye adsorption experiments

The initial and final concentrations of MB solutions were determined by measuring absorbance changes at their respective absorption maxima and sampling at regular intervals, using UV–Visible spectrophotometer (Thermo Scientific, Evolution 201) at the MB maximum adsorption wavelength (664 nm). All dye adsorption experiments were carried out in 125 mL flasks with constant stirring. 100 mL of the 20 mg/L MB solutions were mixed with an appropriate amount of -adsorbent and stirred for defined contact times in an ambient condition. The dye removal efficiency (%) at time t was calculated by Equation (1-1) as follows:

$$removal\ (\%) = \frac{C_0 - C_t}{C_0} \times 100 \qquad (1\text{-}1)$$

where C_0 and C_t are initial and at time t concentrations of MB (mg/L), respectively. The influences of experimental parameters, dosage of powder (0.1–1 g/L), contact time (5–60 min), and initial

dye concentration (5–100 mg/L) on the removal of MB were studied in the batch mode of operation. All adsorption experiments were run in duplicates and the mean values were reported. The pH of each solution was adjusted by adding diluted HNO_3 or NaOH and measured with an Orion 5 Star Series Meter.

1.2.8 Isothermal study

The adsorption isotherms were used for evaluation of equilibrium data. It is necessary to fit the equilibrium absorption data with different adsorption isotherms to analyze an absorption process [30]. Hence, the more common isotherm models, Langmuir and Freundlich models were used in this study. The amount of methylene blue adsorption at equilibrium q_e (mg/g) was calculated by using the mass balance Equation (1-2):

$$q_e = \frac{(C_0 - C_e)V}{m} \tag{1-2}$$

where C_0 and C_e are initial and equilibrium concentrations of MB (mg/L), respectively, V is the volume of the solution (L), and m is the mass of adsorbent, GO, MgO, or GO/MgO NCs (g).

1.3 Results and discussion

1.3.1 Characterization of GO, MgO, and GO/MgO NCs

The SEM images of GO, MgO and NCs are shown in Figure 1.1(a) shows that MgO powders are porous and agglomerated consistent with previous studies [10,11]. GO obtained from modified Hummers method is shown in Figure 1.1(b), with a layer of wrinkled graphene oxide sheet at a low magnification. 3D nanostructures of GO/MgO NCs that are synthesized by the sonication method are shown in Figure 1.1 (c, d, and e), for the three different ratios of 1:5, 1:1 and 5:1, respectively, depicting that the surfaces of GO are covered by MgO. Compared to GO/MgO NC 1:5 ratio, there are smaller amounts of MgO on GO surface in 1:1 and 5:1 ratios. It

is evident from the SEM images that MgO particles were anchored heterogeneously on the GO sheets. GO sheets show agglomerated leaf-like structure.

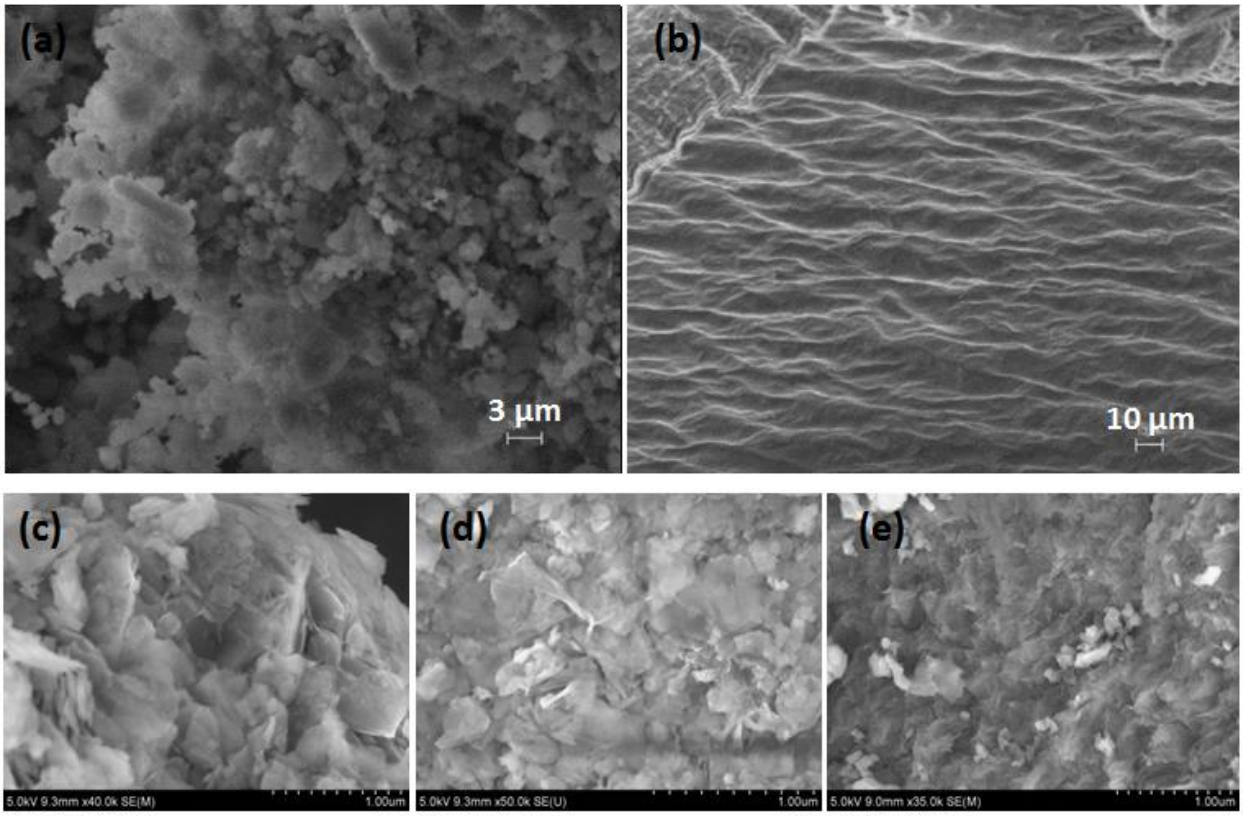

Figure 1.1 SEM images: (a) MgO, (b) GO, and GO/MgO NCs for ratios (c) 1:5, (d) 1:1, and (e) 5:1

TEM images of MgO NPs distributed on the graphene oxide sheets are shown in Figure 1.2 (a–c) for the three different NC ratios. The figures show that MgO NPs are smaller than 20 nm. Similarly, to the SEM images, dispersion of MgO NPs on GO sheets is not completely uniform. The figures also show that MgO NPs are sitting tightly on GO nano-sheets.

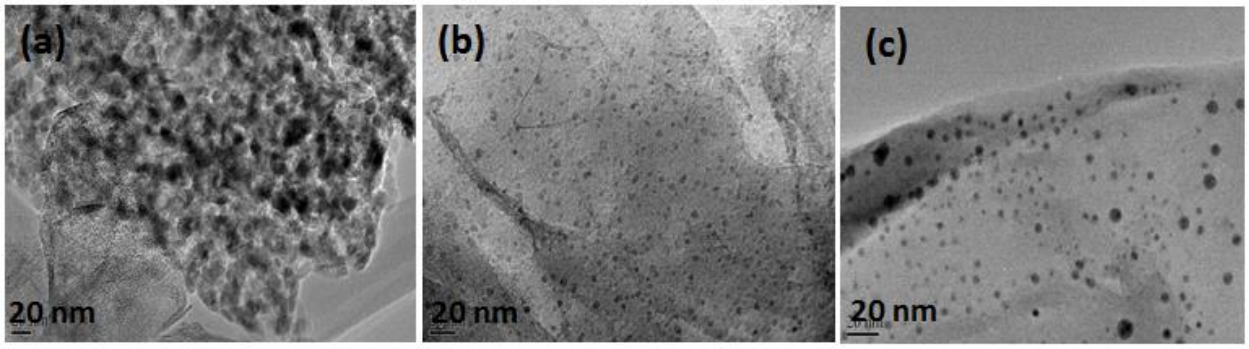

Figure 1.2 TEM images for GO/MgO NCs for ratios (a) 1:5, (b) 1:1, and (c) 5:1

XRD patterns of graphite, GO, MgO, and GO/MgO NCs are shown in Figure 1.3. As shown in Figure 1.3(a), the diffraction peak for graphite is at 2θ = 26.40°, while the diffraction peak for GO is at 2θ = 11.2°. This change in the peak shows that the oxidation process decreases peak intensity and it demonstrates the typical loose layer-like structure of GO. The GO peak is due to the abundant oxygen-containing functional groups on the surface of GO [49]. The presence of GO, MgO, and $Mg(OH)_2$ in the NC powders can also be observed. As shown in Figure 1.3(b), the peaks positioned at 2θ = 36.8°, 42.8°, 62.3°, 74.5°, and 78.4° belong to MgO. In addition, the diffraction peaks at the 2θ value of 18.4°, 32.8°, 38.0°, 50.9°, 58.7°, 68.4°, and 72.1° are matched with $Mg(OH)_2$. $Mg(OH)_2$ was produced during modification of GO by MgO through a sonication process in DI water. The diffraction peak for GO at 2θ = 11.2° decreased as the ratio of MgO was increased in the NCs and it almost disappeared in the GO/MgO 1:5 ratio.

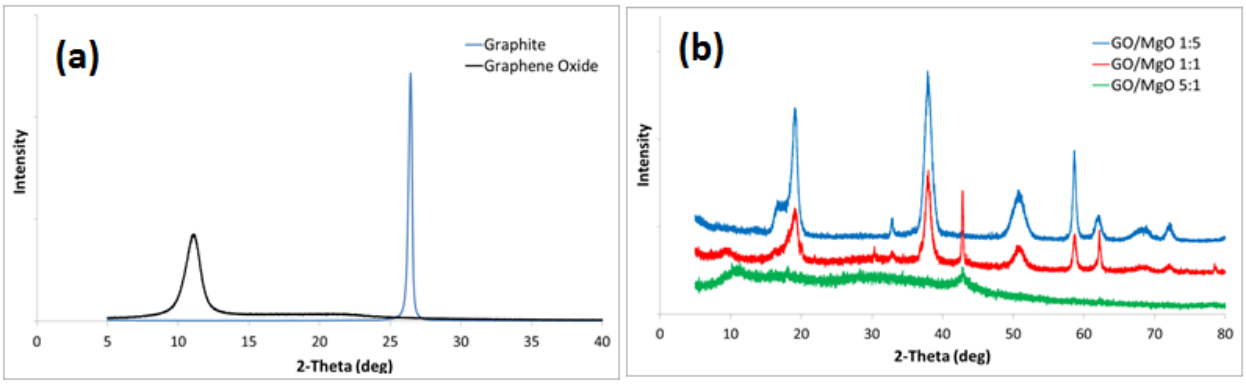

Figure 1.3 XRD patterns: (a) Graphite and Graphene Oxide, (b) GO/MgO NCs for ratios 1:5, 1:1, and 5:1

In order to investigate the functional groups of GO, MgO, MB, and GO/MgO NCs, FTIR spectroscopy was used in the wavenumber range of 4000–400 cm^{-1}. The results are shown in Figure 1.4. In Figure 1.4(a), the sharp peak around 3700 cm^{-1} on MgO and GO/MgO NCs is related to the presence of hydroxyl groups. For MgO NPs, the hydroxyl group comes from the reaction between the surface of MgO NPs with water vapor in air or defects [47]. The intensity of this peak decreases with a decrease in the MgO ratio in GO/MgO NCs. For GO and GO/MgO NCs, the broad band in the range of 3100–3500 cm^{-1} is assigned to the appearance of the stretching of O− H [8]. The FTIR of GO is in good agreement with other reported studies [15,50,51]. The peaks at 1730 cm^{-1} and 1630 cm^{-1} correspond to C=O and C=C stretching. The bands located at 1388 cm^{-1} and 1068 cm^{-1} are ascribed to C-OH stretching and –O-C stretching vibrations mode of sp2 carbon skeletal, respectively. Figure 1.4(b) shows the infrared spectra of the MB and GO/MgO NCs after adsorption. For MB, peaks detected at 1604 cm^{-1} and 1494 cm^{-1} can be attributed to stretching vibrations of the aromatic rings. The peak at 1400 cm^{-1} can be attributed to C-N stretching, and the peak at 1358 cm^{-1} reflects -CH_3 symmetric deformation 36 [34]. Similar bands appeared in the infrared spectra of GO/MgO NCs after adsorption with some shift from 1604 cm^{-1} to 1594 cm^{-1} for GO/MgO 1:5 ratio, and to 1589 cm^{-1} for GO/MgO 1:1 and 5:1 ratios.

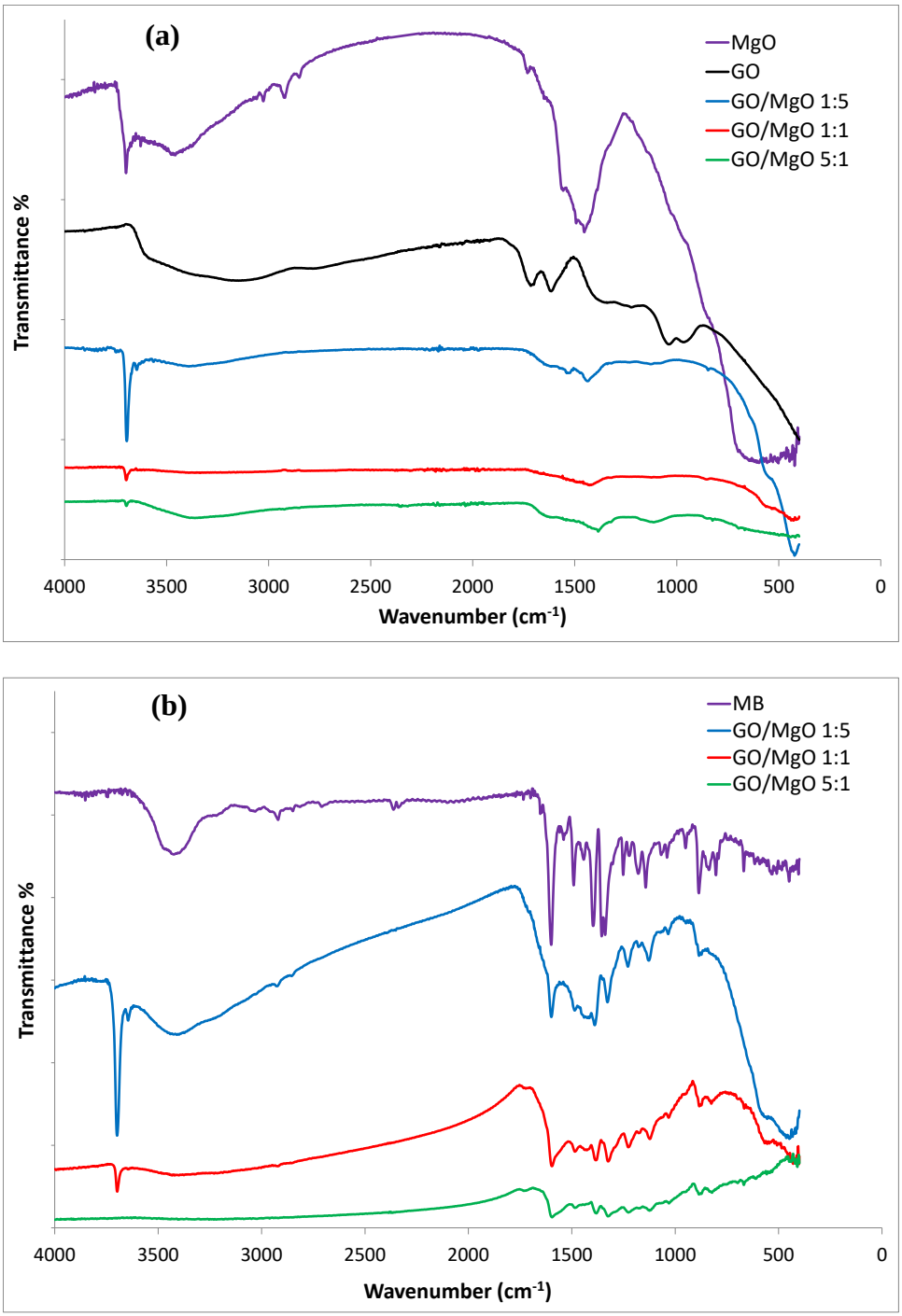

Figure 1.4 FTIR spectra: (a) MgO, GO, and GO/MgO NCs before adsorption; (b) MB and GO/MgO NCs after adsorption

In addition, the peak at 1494 cm^{-1} shifted to around 1488 after adsorption for all ratios. Similar results have been reported previously [52]. These shifting bands for aromatic rings suggest

that there may be π–π interaction between the aromatic rings of MB and the GO/MgO NCs. The sharp peak around 3700 cm^{-1} disappeared after adsorption in GO/MgO 5:1, which is due to the interaction between hydroxyl groups on the surface of the adsorbent and MB.

The full scan XPS spectrum of GO/MgO NCs before and after adsorption of MB is given in Figure 1.5. Similar to FTIR results, the intensity of the Mg peaks (Mg 1s, Mg KLL, Mg 2S, and Mg 2p) increases with the increase of Mg ratio in the NCs, whereas the intensity of C peaks (C KLL and C1s) decreases (Figure 1.5(a)). After adsorption of MB on the NCs, there are new peaks for S and N, which correspond to MB as shown in Figure 1.5(b).

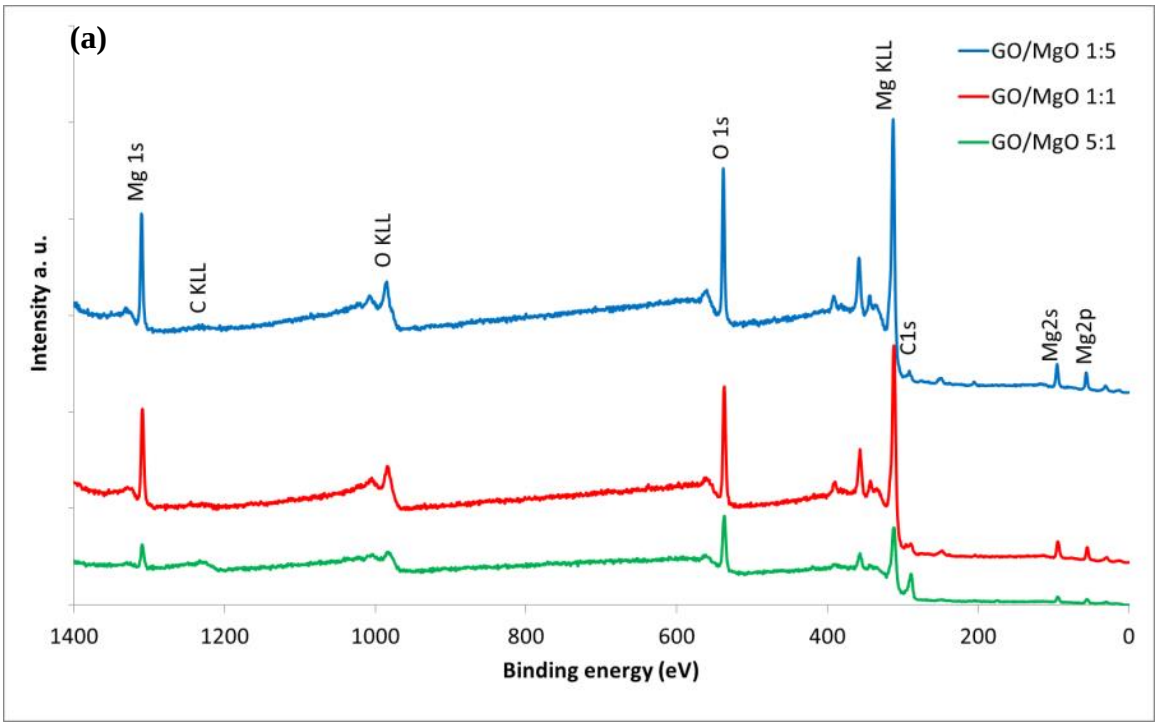

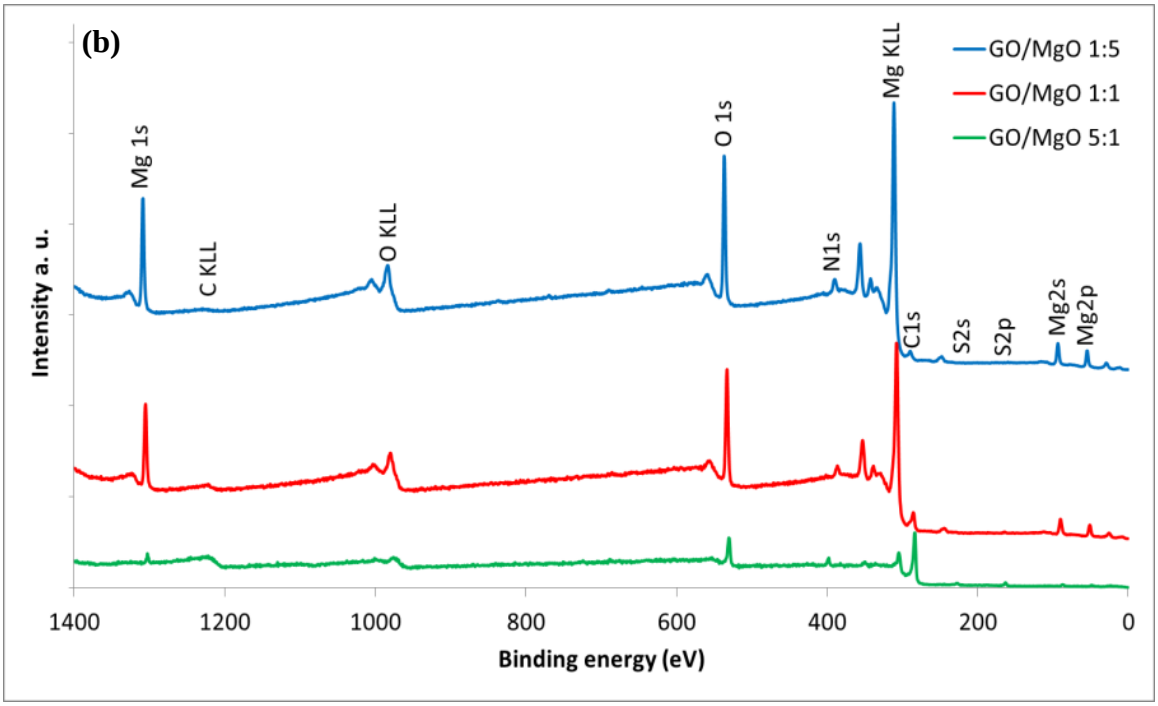

Figure 1.5 XPS spectrum of GO/MgO NCs (a) before and (b) after adsorption

In order to study the thermal stability of GO/MgO NCs, TGA was performed up to 900 °C and the results are shown in Figure 1.6. As seen from the results, an initial weight loss up to 110° was observed for all NC ratios, which is mainly due to dehydration [53]. For GO/MgO NC ratio 1:5, the major weight loss took place between 290 and 450 °C. The 25% weight loss in this temperature range is mainly due to the decomposition of $Mg(OH)_2$ [54]. On the other hand, GO/MgO NC with 1:1 ratio lost 17% in this range as a result of $Mg(OH)_2$ decomposition. This weight loss is not as sharp as that with the GO/MgO NC 1:5 ratio, which is due to the decomposition of oxygen-containing functional groups within GO [55] in addition to $Mg(OH)_2$ decomposition. For GO/MgO NC 5:1 ratio, the weight loss is 7% between 290 and 450 °C. Due to the existence of higher amounts of GO within the GO/MgO 5:1 NC, decomposition of labile oxygen-containing functional groups such as hydroxyl or epoxy (within GO) is more considerable in the range of 150–500 °C [56] compared to the decomposition of $Mg(OH)_2$.

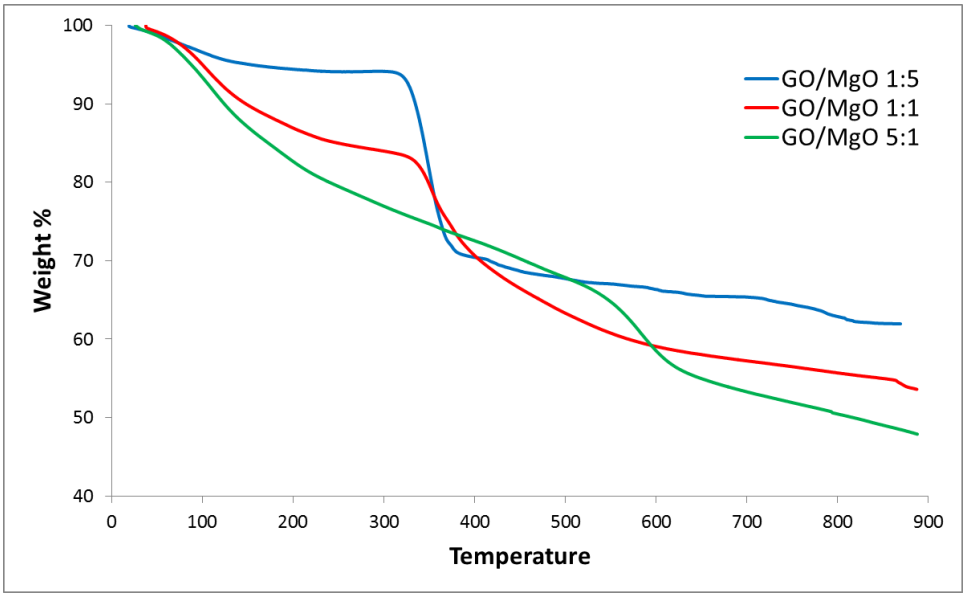

Figure 1.6 Thermogravimetric analysis of GO/MgO NCs

Table 1.1 shows the percentage of Mg ions in each ratio (5:1, 1:1, and 1:5) of GO/MgO NCs and pure MgO solutions at different pHs. Almost all of the Mg ions in all ratios of NCs are dissolved in the solution at pH 1. The solubility of Mg decreased with the increase in pH. As seen from the results (e.g., pH = 3 and pH = 7), GO/MgO NC with 5:1 ratio has the lowest concentration of Mg ions dissolved in solution as compared to other ratios with lower amounts of GO within the NC. This is because of the partial wrapping of MgO by graphene oxide that can acts as a barrier for MgO against acids. Similar results were reported for the ZnO-Graphene composite and the PbS-Graphene composite [15,57]. The comparison of the results of NCs to MgO also shows the higher acid resistance of the synthesized NC material over pure MgO, due to the lower observed solubility of Mg in NCs demonstrating higher stability of Mg with increased pH.

Table 1.1 Percentage of Mg concentration at effluent solution of GO/MgO NCs at different pH

Adsorbent	**pH=1**	**pH=3**	**pH=7**
GO/MgO 1:5	99.13 ± 1.07 %	76.14 ± 1.2 %	47.35 ± 0.15 %
GO/MgO 1:1	100 ± 1.03 %	74.3 ± 1.03 %	25.79 ± 0.83 %
GO/MgO 5:1	100 ± 0.34 %	66 ± 1.2 %	17.1 ± 0.15 %

1.3.2 Dye adsorption

Adsorption of MB by GO/MgO NCs, GO, and MgO was investigated under different experimental conditions: dosage of adsorbent, contact time, and initial MB concentration. The effect of each of these variables on the adsorption of MB is described in detail below.

1.3.2.1 Effect of dosage

The effect of GO, MgO, and GO/MgO NC dosage (0.1–1 g/L) on the removal of MB (20 mg/L) was studied at pH of 7. The remaining dye concentration was measured after 20 minutes of stirring the suspension. The results showed that for all GO/MgO ratios, the efficiency of adsorption increased with the increase of dosage of adsorbents (Figure 1.7(a)). This is attributed to the increase in the availability of adsorbent surface area and active sites provided at higher dosage [10,58]. According to Figure 1.7(a), the optimum adsorbent dosages for adsorbing 20 mg/L of MB were as follows: 1 g/L for MgO, 0.6 g/L for GO, 1 g/L for GO/MgO 1:5 ratio, 0.6 g/L for GO/MgO 1:1 ratio, and 0.6 g/L for GO/MgO 5:1 ratio. These dosages were used in the following experiments.

1.3.2.2 Effect of contact time

The effect of contact time on the adsorption of MB on GO, MgO, and GO/MgO NCs was investigated in the range of 1–60 minutes for the removal of 20 mg/L MB concentration at pH 7. Figure 1.7(b) shows that the MB removal percentage increased quickly with the increase of contact time. The adsorption of MB onto GO and GO/MgO NCs increased rapidly in the first 10 min, then was more gradual. More than 55% of the dye was removed in the first minute for GO and all ratios of GO/MgO NCs. This could be due to the high number of available adsorption sites at the beginning of the adsorption process, which then later became saturated. According to the results seen in Figure 1.7(b), at all times, GO/MgO NC with 5:1 ratio had the highest removal percentage, whereas MgO had the lowest value. Although the removal efficiency of NC with 1:1 ratio was higher than the 1:5 ratio and GO, it was still slightly lower than the NC with 5:1 ratio. The results showed that for GO, and all GO/MgO NCs ratios, almost all of the MB dye was removed in 20 minutes after which there was no significant increase in the adsorption efficiency of MB. On the other hand, pure MgO removed only 8% of MB after 20 minutes; this percentage did not improve over time. As a result, 20 minutes contact time was chosen as the optimum time for the experiments to study the effect of initial MB concentration.

1.3.2.3 Effect of initial concentration of MB

Since MB is used in different industries, dye concentration in wastewater is variable. As a result, it is important to study the adsorption efficiency of adsorbents for different initial MB concentrations. In this study, MB concentrations in the range of 5–100 mg/L were prepared and the performance of dye removal was studied at pH of 7 after 20 min. As shown in Figure 1.7(c), almost all of the 5, 10, 15, and 20 mg/L initial concentrations were removed in 20 minutes for GO

and all GO/MgO NC ratios. After 20 mg/L concentration, the efficiency of adsorption decreased gradually. GO/MgO NC with 5:1 ratio had the highest capacity for removal of MB compared to other NC ratios or GO, where the adsorption efficiencies for initial concentrations of MB at 30, 50, and 100 mg/L were 92%, 77%, and 53%, respectively. On the other hand, the NC 1:5 ratio had the lowest efficiency among the GO/MgO NCs for MB removal with the observed adsorption efficiencies of 81%, 59%, and 33%, for initial MB concentrations of 30, 50, and 100 mg/L, respectively. The efficiency of MB removal by the NC with 1:1 ratio was remarkably less than the 5:1 ratio, but close to 1:5 ratio, where the removal efficiencies for these last two ratios were not noticeable. Pure GO, compared to NC ratios 1:1 and 1:5 removed MB at higher efficiency, while the removal efficiency was lower compared to the NC with 5:1 ratio. The results, therefore, indicated that the initial dye concentration significantly affected the MB removal efficiency onto the adsorbents and the adsorption of MB was mainly occurring on the GO sites compared to the MgO sites which are consistent with FTIR results. Similar results were obtained [59] for superior adsorption ability of GO compared to $Mg(OH)_2$. Figure 1.7(d) and 2.7e illustrate the comparative behavior of GO and GO/MgO NCs in water. Although GO is completely dispersed in water because of the presence of polar functionalities as well as the formation of hydrogen bonds between GO and water molecules (Figure 1.7(d)), the GO/MgO NCs precipitate to the bottom of the tube (Figure 1.7(e)) which may be due to the interaction between the functional groups of GO with MgO particles. Since MgO particles are heavy, these interactions cause the composite to settle down. An illustration of an aqueous solution of 20 mg/l MB dye before (Figure 1.7(f)) and after (Figure 1.7(g)) treatment with GO/MgO NCs is also shown. The GO/MgO NC was successfully applied for removal of MB while rendering GO easily settled in aqueous solutions. Illustration of (d) GO being completely dispersed in water; (d) addition of the synthesized GO/MgO NC material

separating GO from water by precipitating to the bottom of the tube; (e) before and (e) after treatment of 20 mg/L MB solution in water by GO/MgO NC material after 20 minutes contact time at pH 7.

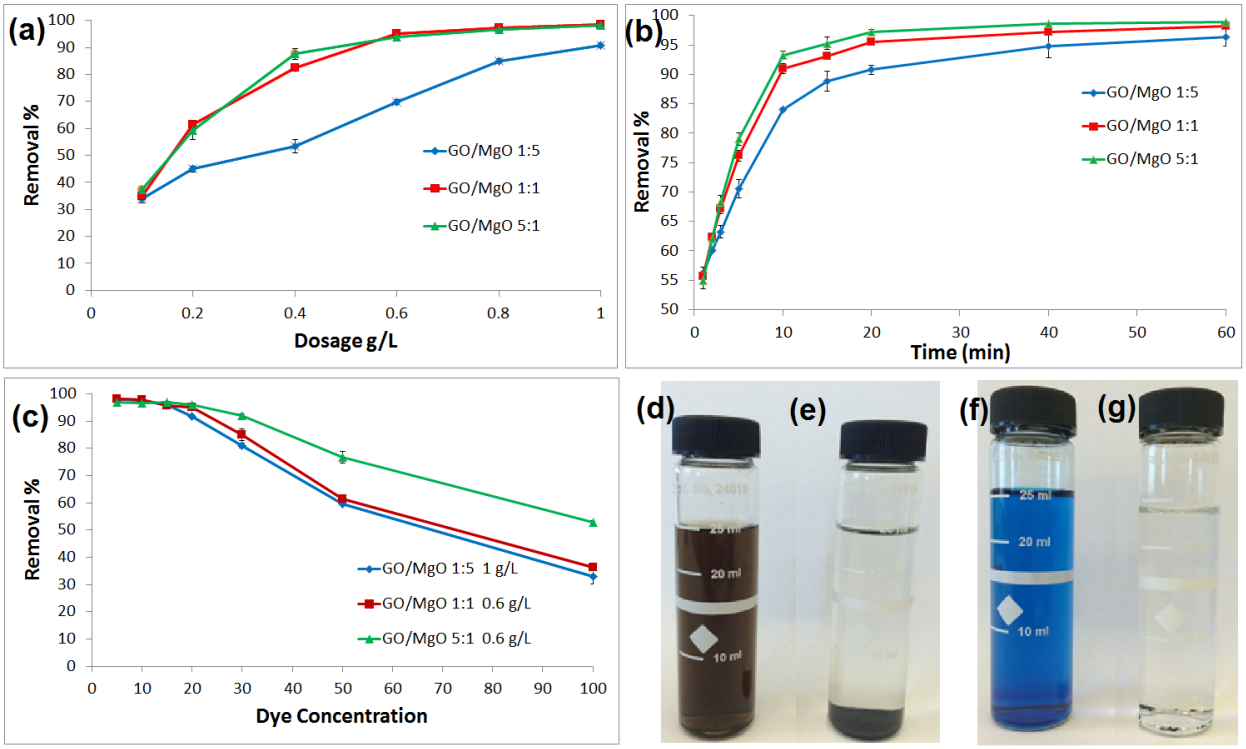

Figure 1.7 Removal of MB (20 mg/L) at pH 7 based on (a) GO/MgO NC dosage after 20 min; (b) contact time; (c) initial MB concentration after 20 min for different ratios of 1:5, 1:1, and 5:1

1.3.3 Adsorption isotherms, effect of pH and adsorption mechanism

Adsorption isotherms were studied to determine the adsorption mechanisms. Among all isotherm models, Langmuir and Freundlich equations are the most commonly used [60].

The Longmuir model is based on the assumption that adsorption is a monolayer adsorption on a homogenous surface of adsorbent, and is described as Equation (1-3):

$$\frac{C_e}{q_e} = \frac{C_e}{q_m} + \frac{1}{q_m K_l} \qquad (1\text{-}3)$$

where C_e (mg/L) is the equilibrium concentration of MB, q_e (mg/g) is the amount of MB adsorbed per unit weight of GO/MgO NCs, q_m (mg/g) is the maximum theoretical MB adsorbed, and K_L (L/mg) is the Longmuir constant related to the affinity of binding sites. The Langmuir isotherm plots C_e/q_e versus C_e are used to calculate the q_m and K_l values from the slopes and intercepts of the plots.

The Freundlich model is based on the assumption of multilayer adsorption on adsorbent and is described as Equation (1-4):

$$logq_e = logk_f + \frac{1}{n} logC_e \quad (1\text{-}4)$$

where k_f (mg/g) and n are the Freundlich constants indicating the capacity of the adsorbent for the adsorbate and strength of adsorption, respectively. The Freundlich isotherm plots log q_e versus log C_e, are used to calculate the k_f and n values.

The fitted results for the Longmuir and Freundlich isotherms are shown in Figure 1.8. Table 1.2 shows the parameters of Langmuir and Freundlich adsorption isotherms for MB adsorption onto GO and GO/MgO NCs with the three different NC ratios at three different pH values and MgO at pH of 7.

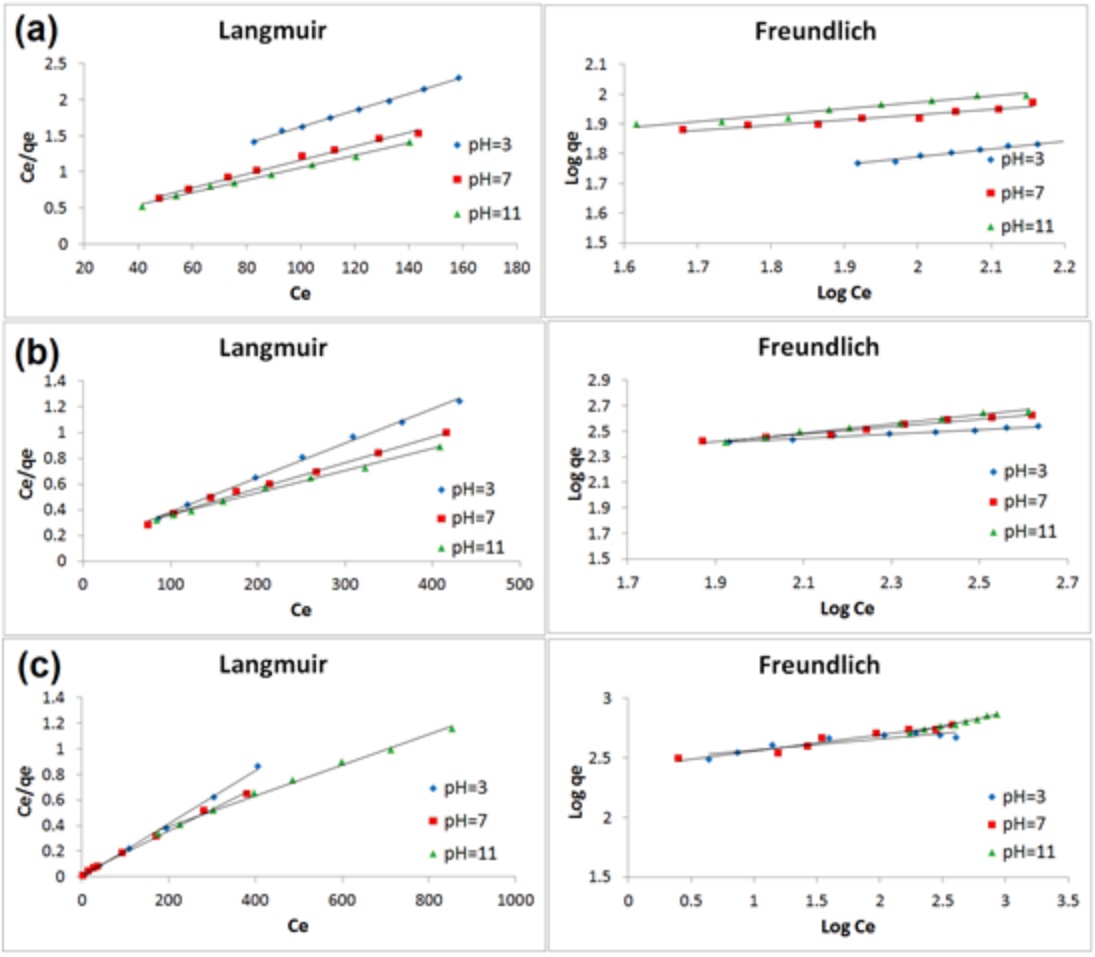

Figure 1.8 Adsorption isotherms of MB on GO/MgO NCs for ratios (a) 1:5, (b) 1:1, (c) 5:1, GO, and MgO at different pH

Table 1.2 shows the correlation coefficients (r^2) of the Langmuir isotherms are greater than the ones calculated by Freundlich isotherms for adsorbents, indicating that the adsorption of MB onto GO, MgO, and GO/MgO NCs would take place in a monolayer adsorption. The maximum adsorption capacity, q_m, of the MB onto all adsorbents, in different pHs is given in Table 1.2. Maximum adsorption capacity for GO/MgO is observed to be the highest for 5:1 ratio, whereas the GO/MgO 1:5 ratio had the lowest amount of adsorption capacity among the NCs. It can be concluded that GO/MgO NCs with 1:1 and 5:1 ratios had higher adsorption capacities of MB removal in comparison with pure GO and MgO. This synergetic effect can be attributed to the

efficient dispersion of MgO on GO sheets, inhabitation of agglomeration of MgO NPs, and suppression of stacking and bundling of GO sheets. Similar synergetic outcomes were also observed for GO nanosheets with different composites [53,61]. Our results showed that the efficiency of adsorption of MB was dependent on the pH of the solution.

Table 1.2 Langmuir and Freundlich isotherm parameters for MB sorption onto GO/MgO NCs, GO, and MgO at different pH

Adsorbent	pH	Initial Concentration (mg/L)	Langmuir			Freundlich		
			q_m (mg/g)	k_L (L/g)	R^2	n	k_f (L/g)	R^2
	3	200	87	0.024	0.9979	3.77	18.14	0.9752
GO/MgO 1:5	7	200	104	0.048	0.9908	5.71	38.11	0.9215
	11	200	114	0.045	0.9959	4.69	35.18	0.9571
	3	500	370	0.022	0.9970	5.7	120.61	0.9766
GO/MgO 1:1	7	500	500	0.012	0.9916	3.45	74.15	0.9662
	11	500	588	0.009	0.9953	2.76	53.38	0.9897
	3	500	476	4.2	0.9985	10.66	297.37	0.8242
GO/MgO 5:1	7	500	588	0.090	0.9973	7.37	264.12	0.9378
	11	1000	833	0.007	0.9944	4.5	163.72	0.9868
	3	700	285	0.0413	0.998	18.58	169.2	0.6892
GO	7	700	333	0.089	0.9989	47.39	287.07	0.3462
	11	700	333	0.306	0.9966	178.5	314.8	0.0113
MgO	7	50	9.27	0.043	0.9902	2.907	1.65	0.9653

Figure 1.8 Adsorption isotherms of MB on GO/MgO NCs for ratios (a) 1:5, (b) 1:1, (c) 5:1, GO, and MgO at different pH also presents the influence of the initial pH of the solution on the adsorption of MB onto GO and GO/MgO NCs in the pH ranges of 3.0, 7.0, and 11.0. According to the results, the highest and the lowest adsorption capacity of the MB with GO and GO/MgO

NCs belongs to pH 11.0 and pH 3.0, respectively. For better understanding of the pH effect, the pH of point of zero charge (pH_{pzc}) of GO/MgO NCs was determined according to the pH drift procedure [62], where the pH_{pzc} for GO/MgO ratios 5:1, 1:1, and 1:5 were determined to be ~ 9.7, 10.5, and 10.5, respectively (inset in Figure 1.9). On the other hand, the pH_{pzc} for pure GO and MgO is 3.9 [63] and 12.4 [10], respectively. At pH below pH_{pzc}, the adsorbent surface has a positive charge and at pH above pH_{pzc} the surface has a negative charge. Therefore, electrostatic attraction can be the dominant mechanism of adsorption between GO or GO/MgO NCs and MB when pH is above pH_{pzc}. For pH values below pH_{pzc}, other adsorption mechanisms such as hydrogen bonding [62] and π–π interaction [64] may attribute to the adsorption.

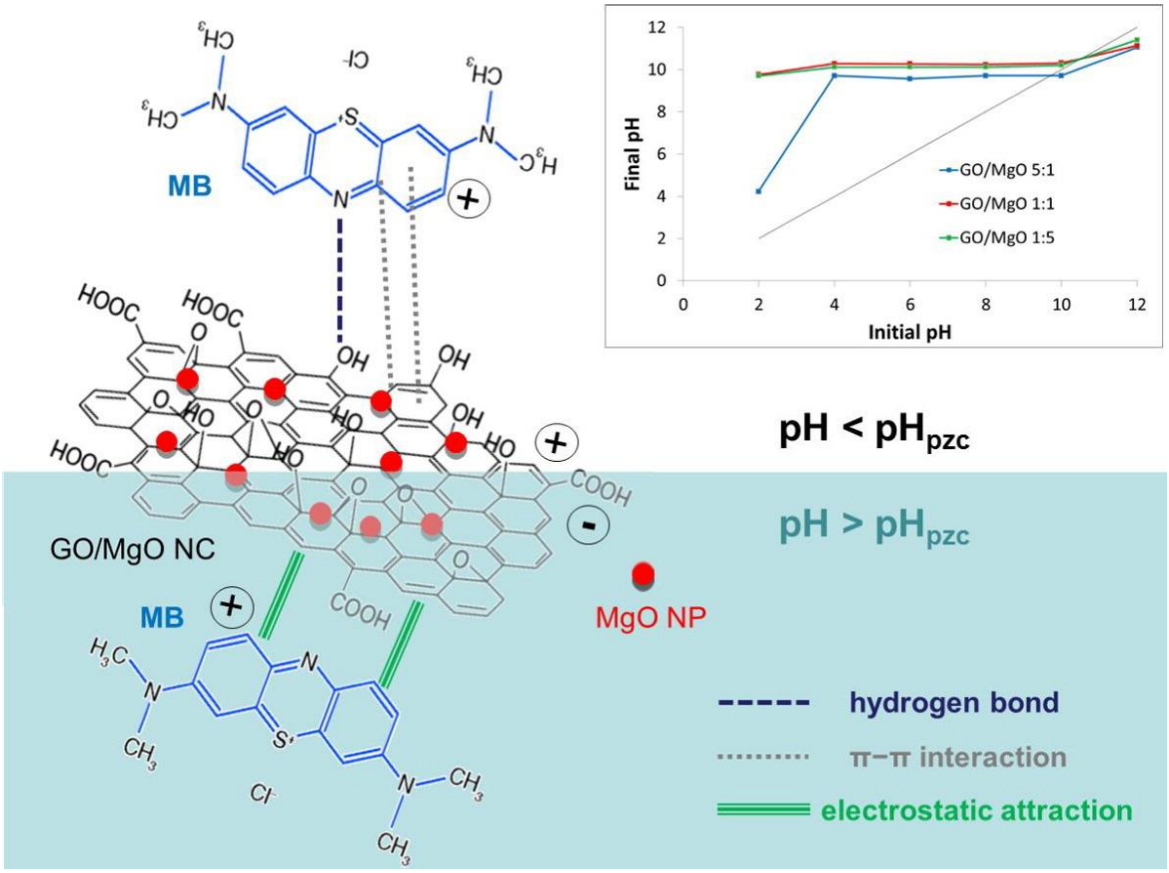

Figure 1.9 Schematic illustration of probable adsorption mechanisms of MB by GO/MgO NC below and above pH_{pzc}

Figure 1.9 illustrates probable adsorption mechanisms of MB by GO/MgO NCs when pH was above and below pH_{pzc}. Comparably, the same pH-regulated behavior was observed in different studies on MB[22,65–67] .

Table 1.3 Comparative summary of MB adsorption by various GO-based adsorbents

Adsorbent	q_e (mg/g)	Temperature °C	pH	Reference
Graphene	204	60	NR[a]	[68]
Graphene	185	40	NR[a]	[68]
Graphene	153	20	NR[a]	[68]
GO	240	25	6	[69]
GO	730	0	8	[65]
GNS/Fe3O4	43.8	24	NR[a]	[67]
GO	43.5	30	5.3	[51]
MCGO	95.16	30	5.3	[51]
GO	144.9	25	5.4	[70]
GO/CA	181.1	25	5.4	[70]
GO/MgO 1:5	114	Ambient	11	This study
GO/MgO 1:1	588	Ambient	11	This study
GO/MgO 5:1	833	Ambient	11	This study
GO	333	Ambient	11	This study
MgO	9.27	Ambient	7	This study

A comparative summary of the adsorption capacities of the various GO-based adsorbents reported in the literature for the removal of MB is given in Table 1.3. It is seen that the adsorption capacity of the GO/MgO is greatest for the 5:1 ratio (833 mg/g) compared to other ratios tested in this study (588 mg/g for 1:1 ratio and 114 mg/g for 1:5 ratio) and GO (333 mg/g), as well as compared to other graphene-based composite adsorbents listed for MB removal. This high

adsorption capacity shows that GO/MgO NCs is an applicable adsorbent for the efficient removal of MB from wastewater.

1.3.4 Kinetics studies

In order to investigate the mechanism of the adsorption process, two most common kinetic models: pseudo-first-order equation and pseudo-second-order equation were employed to analyze the experimental data for all GO/MgO ratios at an initial concentration of 20 mg/L MB. Figure 1.10 presents the adsorption kinetics of MB onto GO, MgO, and GO/MgO NCs using the two models. The pseudo-first order equation [71] is represented as Equation (1-5):

$$\frac{1}{q_t} = \frac{k_1}{q_e t} + \frac{1}{q_e} \qquad (1\text{-}5)$$

where q_e (mg/g) and q_t (mg/g) are the amounts of MB adsorbed on adsorbents at equilibrium and at time *t*, respectively, and k_1 (1/min) is the pseudo-first-order constant. The parameters values of the kinetic models are given in Table 1.4 Pseudo-first order and pseudo-second order adsorption constants. The results show that the experimental q_e is not close to the calculated q_e and the coefficient of determination r^2 is low indicating a poor fit with the pseudo-first-order kinetic model.

The pseudo-second-order equation [72] is expressed as Equation (1-6):

$$\frac{t}{q_t} = \frac{1}{k_2\, q_e^2} + \frac{t}{q_e} \qquad (1\text{-}6)$$

where k_2 (g/mol min) is the equilibrium rate constant of the pseudo-second-order equation. As seen in Table 1.4, the coefficient of determination r^2 in the pseudo-second-order model is greater than 0.999 in all GO/MgO NC ratios. Also, the experimental q_e is close to the calculated q_e, illustrating a strong pseudo-second-order model fit for the MB adsorption onto the GO, MgO, and GO/MgO NCs tested in this study.

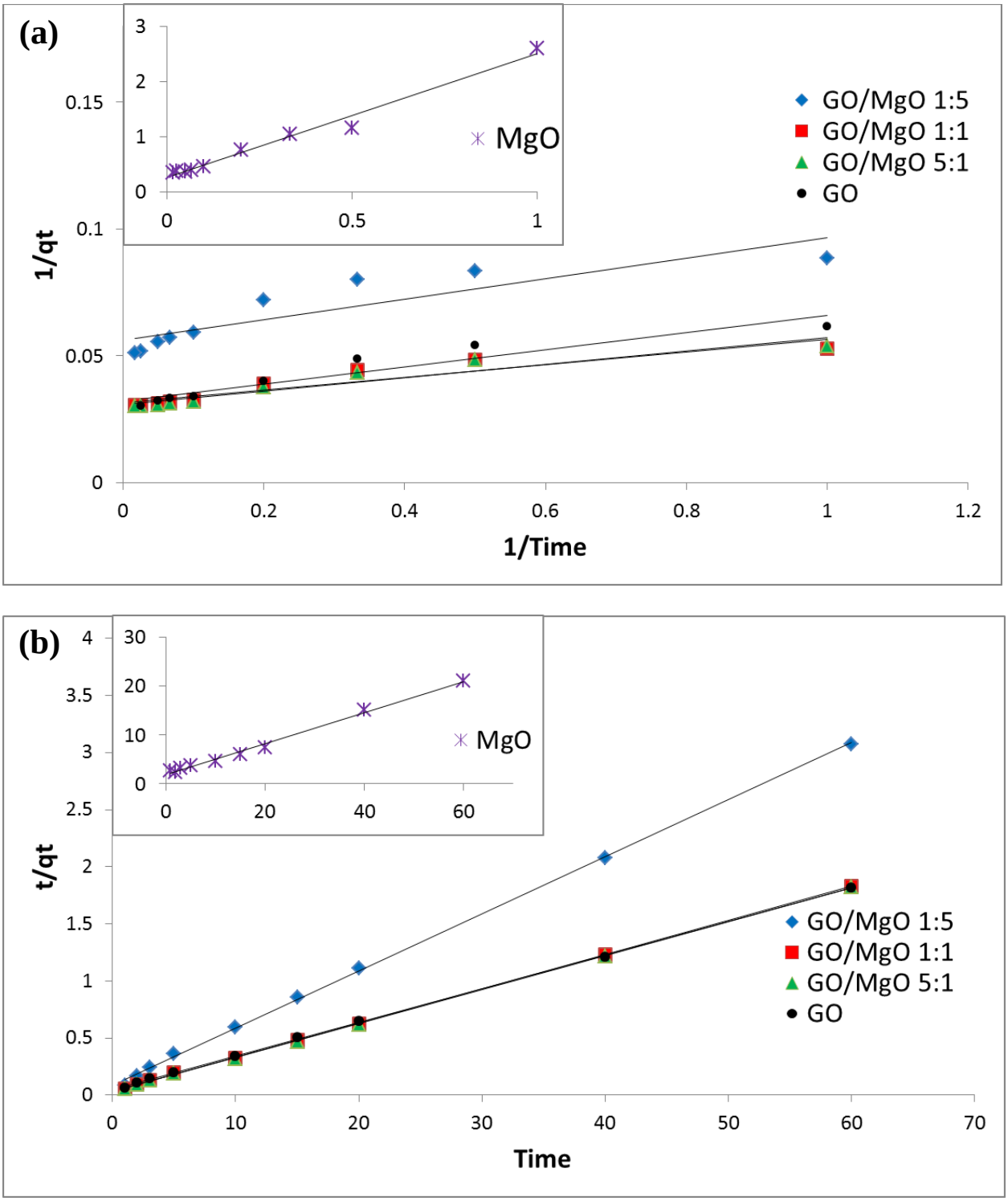

Figure 1.10 (a) Pseudo-first order kinetics and (b) pseudo-second order kinetics for adsorption of MB by GO, MgO, and GO/MgO NCs

Table 1.4 Pseudo-first order and pseudo-second order adsorption constants

GO/MgO Ratio	$q_{e,exp}$ (mg/g)	pseudo-first order model			pseudo-second order model		
		$q_{e,cal}$ (mg/g)	k_1 (1/min)	R^2	$q_{e,cal}$ (mg/g)	k_2 (1/min)	R^2
1:5	21	7.39	0.0163	0.8821	20	0.0029	0.9995
1:1	34	9.26	0.0183	0.7474	33.67	0.0290	0.9998
5:1	34	8.29	0.0196	0.6895	33.44	0.0259	0.9998

1.4 Conclusions

In this study, the graphene oxide/magnesium oxide adsorbent is synthesized and its application for the removal of MB dye from aqueous solutions is demonstrated. The TEM characterization of adsorbents showed that MgO NPs are successfully decorated over GO surface. FTIR results confirmed the synthesis of hybrid composite materials by the formation of chemical bonding between MgO and GO. The synthesized GO/MgO NC showed an improvement in MB adsorption capacity compared to either pure GO or MgO. The GO/MgO nanocomposite with 5:1 ratio demonstrated the highest adsorption capacity as 833 mg/g at pH 11 for removal of MB. The adsorption analysis showed that the adsorption of MB was mainly occurring onto the GO rather than the MgO sites within the composite. The synthesized NCs are promising adsorbents and can be further tested for the successful removal of other pollutants from water and wastewater.

Acknowledgements

We gratefully acknowledge two anonymous reviewers for their valued constructive review comments. This work has been partially supported by the US Environmental Protection Agency People, Prosperity, and the Planet (USEPA P3) Program under Grant No. SU-836141“Synthesis

of Graphene Oxide/Magnesium Oxide Nanoparticles and Its Application for Removal of Emerging Contaminants in Drinking Water". We also thank Dr. Andrew Quicksall's lab for access to FTIR instrument; Dr. David Son's lab at SMU Department of Chemistry for access to TGA instrument; Roy Beavers' lab at SMU Department of Earth Sciences for access to SEM and XRD instruments; Dr. Jean-François Veyan's lab at UT Dallas Materials Science and Engineering for access to XPS instruments; and Dr. Jiechao Jiang's lab at UTA Characterization Center for Materials and Biology for access to SEM and TEM instruments.

CHAPTER 3

Contrasting GO/MgO nanocomposite catalyzed phenol ozonation pathways

2.1 Introduction

In recent years there has been extensive attention given to Advanced Oxidation Processes (AOPs), such as ozonation, for removal of organic contaminants from water and wastewater due to high oxidation potential [24,25]. In these processes, reactants such as ozone are the main active species for oxidizing organic contaminants to carbon dioxide and water or, alternatively, convert them into readily biodegradable compounds [26]. However, the direct oxidation by ozone alone is relatively slow and can hinder its practical application [27]. To overcome this problem, several attempts for process modification have been assessed in the literature. Catalytic ozonation (CO), including heterogeneous catalytic ozonation[28] and homogeneous catalytic ozonation[30], has been developed to ameliorate ozonation performance through the generation of reactive oxygen species (ROS) such as hydroxyl radicals ($^{\bullet}OH$), superoxide radical ($^{\bullet}O_2^-$), and singlet oxygen ($^1O_2$) [32].

A variety of catalysts have been developed for catalytic ozonation such as activated carbon [33,34], metal oxides [23], and metal on supports [36]. Recently, new carbonaceous materials, such as graphene, have been the focus of intense research because of their unique characteristics including chemical stability, high transparency, electron mobility, high thermal conductivity and elasticity [37]. Considering these characteristics, graphene has been applied as a catalyst support for different metal oxides such as MnO_2, TiO_2, Fe_3O_4, and Co_3O_4 [27,73,74]. Magnesium oxide

(MgO), however, has sparingly been addressed in the literature as a catalyst backed on graphene. MgO has been shown to be a promising catalyst for heterogeneous ozonation in wastewater treatment due to its high efficient activity, structural stability, ease of production, environment friendliness, and nontoxicity [75,76]. In our previous study [37,77], we showed an improvement of methylene blue adsorption by graphene oxide when it is modified with magnesium oxide (GO/MgO). We demonstrated that the adsorption capacity of GO increases from 333 mg/g to 833 mg/g. Considering the attractive merits of GO/MgO nanocomposite (GO/MgO NCs), an investigation on the effect of GO/MgO NCs, as a catalyst, on oxidation of organic pollutants is essential.

In the present work, we investigate the catalytic effects and mechanism of the GO/MgO NCs in the ozonation process (O_3/GO/MgO) through the study of the fate O_3 decomposition and ROS generation. Classical quenching tests were carried out to investigate the dominate ROS generated in the process of O_3/GO/MgO. Furthermore, we investigate the catalytic effect of GO/MgO NCs during ozonation at different experimental conditions such as pH, GO/MgO dosage, and ozone dosage.

Wastewater from many industries such as petrochemical, pharmaceutical, refineries, oil field activities, and coal processing contains high concentrations (6-500 mg/L) of phenol that needs removal before discharge to the environment [45,78]. Phenol is a toxic substance that can cause several problems for human health and the environment [45]. Different conventional methods have been proposed for the removal of phenol from wastewater including chemical and biological treatment [73,79]. Biological processes are more favourable due to cost-effectiveness, and simplicity of implementation and operation [80]. But, phenol can inhibit degradation reactions at

concentrations above 50 mg/L in wastewater [81]. Therefore, using AOPs for mineralization of phenol in high concentration is required to remove phenol in wastewater.

2.2 Experimental Methods

2.2.1 Materials

All chemicals and reagents used in this study were analytical grades. Phenol solution (90%), Starch Indicator (0.5% w/v), Potassium Iodide (99%), Sodium Nitrate, Magnesium Chloride Hexahydrate, Sulfuric Acid (98%), Hydrochloric Acid, Sodium Thiosulfate (0.1 N), Potassium Permanganate, tert-Butyl Alcohol (99.5%), Sodium Azide, Sodium Hydroxide Solution, and Hydrogen Peroxide (30%) were purchased from Fisher Scientific. Graphite powder (< 20 μm) was obtained from Sigma-Aldrich.

2.2.2 Synthesis of graphene oxide

GO was synthesized from graphite by using modified Hummers Method [82,83] as described by Heidarizad and Şengör [37]. Briefly, 2 g of graphite powder and 50 mL of sulfuric acid were placed in a 500 mL beaker in an ice bath on a magnet stirrer. Then 2 g of sodium nitrate was added to the beaker. While keeping the temperature less than 10 °C, 6 g of potassium permanganate was slowly added to the suspension. After stirring for 2 h, the solution temperature was rapidly increased to 98 °C by adding 100 mL of DI water to the beaker and maintained for 30 min. Thereafter, 300 mL of DI water was added to the beaker and allowed to cool to room temperature. Following that, 20 mL of hydrogen peroxide solution was added while maintaining stirring for 30 min. The mixture was filtered and washed with hydrochloric acid (5%) and DI water

several times. After sonication and centrifugation of the dispersion, GO was dried with a freeze dryer (LABCONCO, FreeZone 2.5).

2.2.3 Synthesis of MgO

MgO nanoparticles were synthesized by the Sol-gel method described elsewhere [37,84]. In brief, 100 g of magnesium chloride hexahydrate and 50 mL DI water were placed in a 1000 mL beaker and stirred for a few minutes. After dissolving all magnesium chloride hexahydrate in DI water, 50 mL of 1 N sodium hydroxide was added. The solution was maintained under stirring for 4 h for the generation of magnesium hydroxide. The suspension was then centrifuged and washed several times with DI water. MgO was dried at 100 °C in an oven overnight. Ultimately, final nanoparticles of MgO were obtained by calcination in a furnace at 600 °C for 2 h.

2.2.4 Synthesis of GO/MgO NCs

In this study, GO/MgO NCs was synthesized by wet impregnation method as reported by Heidarizad and Şengör [37,77]. In short, 500 mg of GO and 500 mL of DI water were added to a 1000 mL beaker and sonicated for 2 h. Then, 100 mg of MgO was added to the suspension and sonicated for 30 min more. Thereafter, the suspension was centrifuged. Finally, dry GO/MgO NCs were obtained via freeze drying.

2.2.5 Solids Characterization

Fourier Transform Infrared (FTIR) spectroscopy was used for the analysis of chemical bonds from 4000 to 450 cm^{-1} wavenumber by using a Perkin Elmer Frontier spectrometer with a diamond GladiATR Vision (PIKE Technologies) accessory at room temperature. Thermogravimetric Analysis (TGA) and Derivative Thermogravimetric (DTG) of GO and GO/MgO NCs were performed with a TA Instruments TGA-SDT 2960 using 10°/min heating rate under 20 mL/min nitrogen gas flow at a range of 30-800 °C and approximate sample starting weight of 5 mg.

2.2.6 Experimental apparatus and procedure

Figure 2.1 shows the schematic of the catalytic ozonation experimental setup. The experimental set up included an air pump (Whisper 40), air dryer, a three stages air filter, flow meter, an ozone generator (5000BF Ozone Generator, Oxidation Technologies), a magnet stirrer, a 250 mL gas washing bottle with porosity C (25-50 micron) 25 mm disc as reactor, valves and tubing. All experiments were carried out in the reactor with the constant stirring to prevent the catalyst from precipitation. 100 mL of the 500 mg/L phenol synthesized wastewater was ozonated with an appropriate amount of catalyst for defined times under the hood at ambient temperature. The effectiveness of different processes and operational variables including adsorption of GO/MgO nanocomposites, single ozonation, catalytic ozonation of O_3/MgO, O_3/GO, O_3/GO/MgO, catalyst dosage, and ozone dosage were investigated.

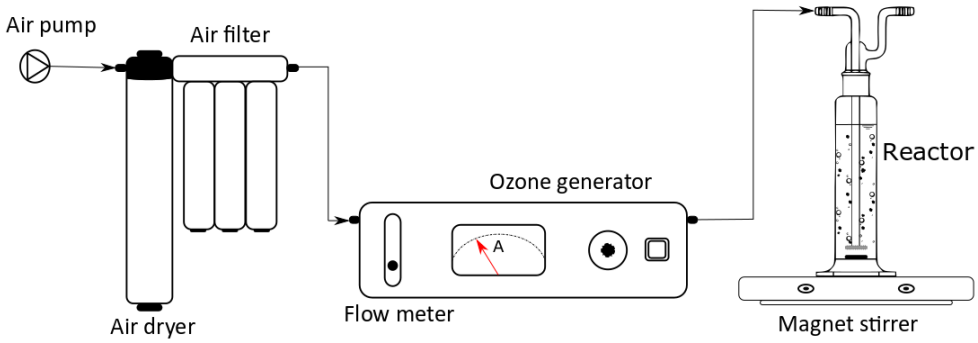

Figure 2.1 The schematic of the catalytic ozonation experimental setup

2.2.7 Analytical methods

The concentration of phenol was measured using UV–Visible spectrophotometer by measuring the maximum absorption wavelength at 500 nm. The removal of phenol was evaluated based on the phenol removal efficiency (%) at time t is calculated by the following Equation (2-1):

$$Phenol\ removal\ efficiency\ \% = (C_0 - C_t)/C_t \quad (2\text{-}1)$$

where C_0 and C_t are initial and at time t concentrations of phenol (mg/L), respectively. The concentration of ozone in inlet gas flow was determined by sparging the target stream into a KI solution (2%) and analyzing the solution using iodometric titration [48]. The concentrations of phenol were measured based on the colorimetric method by measuring the maximum absorption wavelength at 500 nm using Thermo Scientific, Evolution 201 UV–Visible spectrophotometer. All experiments were run in duplicates and the mean values were reported.

2.3 Results and discussion

2.3.1 The catalytic effect of GO/MgO on ozonation process

Catalytic ozonation effects by GO/MgO NCs were examined for oxidization of phenol. Control experiments were carried out to identify self-adsorption of GO/MgO NCs, ozonation only, catalytic ozonation using an equal amount of GO, and an equal amount of MgO for removal of phenol. Figure 2.2 shows the degradation of phenol by different processes in the presence of ozone. As presented in Figure 2.2, GO/MgO NCs can remove an insignificant amount of phenol by adsorption at different times, suggesting that self-adsorption could have little impact on phenol

removal. The adsorption properties of the catalyst are important when discussing the mechanism of catalytic ozonation. Mostly, to understand the process of the removal of a contaminant which could carry out via adsorption and/or oxidation process during ozonation. Additionally, the high adsorption ability of the catalyst for the pollutant can cause permanent blockage of the catalysts active sites and the decrease of their catalytic activity [85]. Ozone alone can oxidize phenol and break it down. Catalytic ozonation of phenol using an equal amount of GO and MgO as those in GO/MgO NCs were also carried out as control experiments. As seen in Figure 2.2, phenol removal was improved marginally when GO or MgO was used individually as a catalyst, revealing that GO and MgO at an equal amount of the GO/MgO NCs could generate some ROS for the oxidation of organic pollutants. On the other hand, GO/MgO NCs as a catalyst significantly increased phenol degradation. The results show the removal of phenol in catalytic ozonation with 0.2 g/L of GO/MgO NCs as a catalyst was increased from 30.8% to 54.7% and from 61.5% to 76.9% at 20 minutes and 60 minutes, respectively.

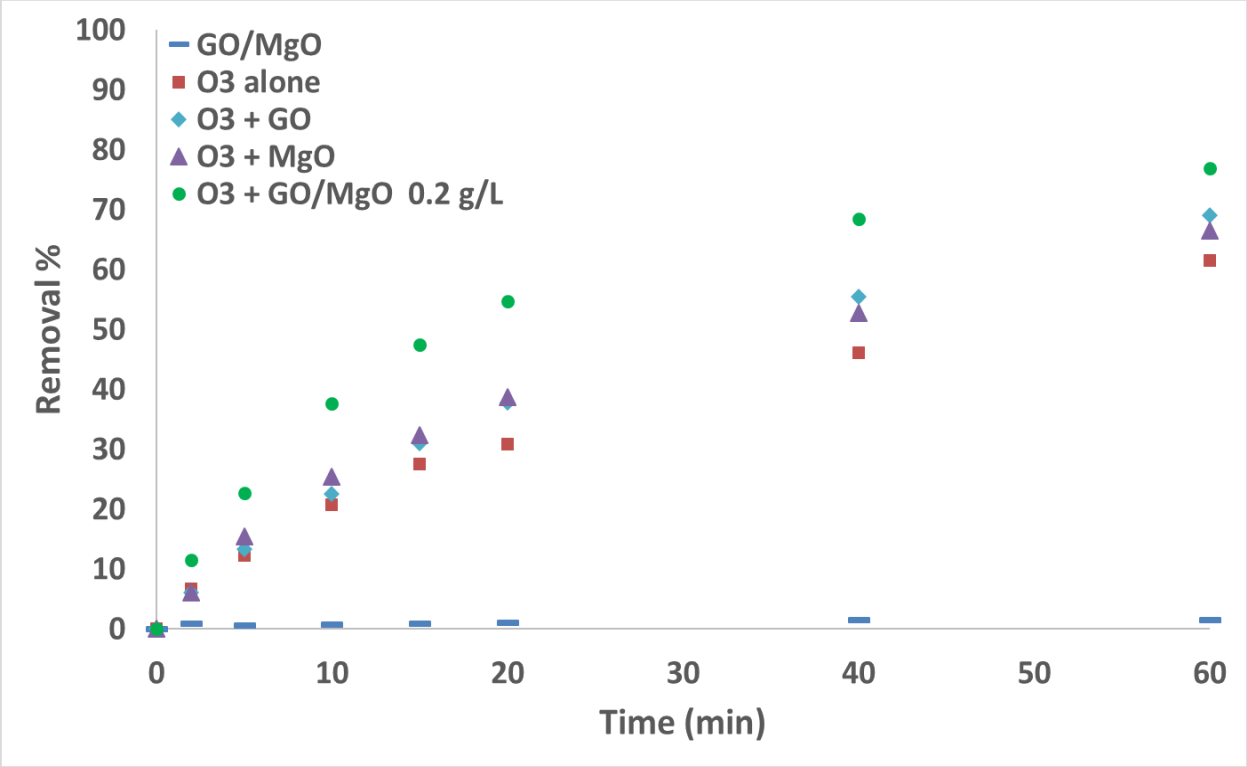

Figure 2.2 Removal of phenol in solution by ozonation and catalytic ozonation for 60 min. (experimental conditions: the flowing rate of O_3: 85 mg/h, phenol concentration: 500 mg/L, Volume: 100 mL, Temperature: 20 °C, and pH: uncontrolled.

2.3.2 Probing reactive oxygen species in catalytic ozonation using GO/MgO NCs as a catalyst

Ozone-based AOPs can simultaneously degrade organic pollutants during direct oxidation with ozone molecules and/or catalytic reaction by radical oxidation, either homogeneously or heterogeneously [23,86]. Via direct oxidation, ozone can attack phenol's ring and break it down. The —OH group in the phenol molecule is electron donating and causes activation of the aromatic ring by increasing its electron density. In addition, because of a high delocalization of electrons on aromatic compounds, phenol shows improved reactivity toward ozone[26].

To understand the indirect oxidation of phenol in this catalytic ozonation using GO/MgO NCs as a catalyst, different scavengers were used to emphasize ROS production. It is known that

$^{\bullet}OH$, $^{\bullet}O_2^-$, and $^1O_2$ are the dominant ROS species in catalytic ozonation and vary depending on catalyst [85]. tert-Butanol (t-BA), is a classical quenching agent for hydroxyl radicals with the reaction rate of 6×10^8 $M^{-1}s^{-1}$ [75], although t-BA reacts with ozone quite slowly at the reaction rate of $3 \times 10^{-5}M^{-1}s^{-1}$ [87]. For quenching $^1O_2$, sodium azide (NaN_3) is widely used as the scavenger with a reaction rate of 2×10^9 $M^{-1}s^{-1}$, that is also an effective probe for $^{\bullet}OH$ with a reaction rate of 1×10^9 $M^{-1}s^{-1}$ because of their close reaction rates [88].

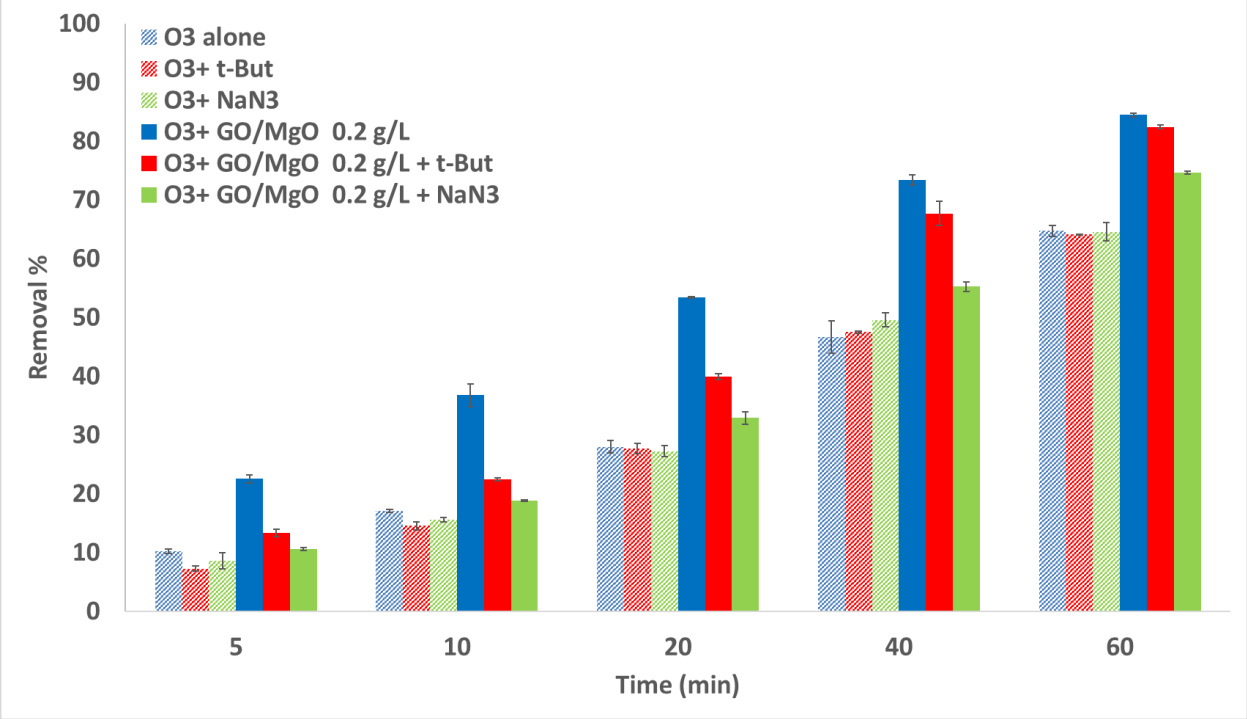

Figure 2.3 Influence of different radical scavengers on the degradation of phenol in ozonation and catalytic ozonation

The quenching tests are revealed in Figure 2.3 for the removal of phenol at different times. As is shown in Figure 2.3, the effect of the t-BA and NaN_3 on the removal of phenol is very low and negligible when ozone is the only oxidant. On the other hand, when 12 mM NaN_3 or 12 mM t-BA was added, for instance, the removal of phenol at 20 minutes in catalytic ozonation dramatically decreased from 53.39 % to 32.88 % and 39.91 %, respectively. The remarkable

decrease in the removal of phenol suggests that both •OH and $^1O_2$ are the main reactive species for the GO/MgO NCs promoted catalytic ozonation process.

2.3.3 Mechanism of phenol degradation in catalytic ozonation process and reaction pathways

The different possible mechanisms involved in phenol degradation via catalytic ozonation using GO/MgO can occur in both the bulk solution and catalyst surfaces. Ozone is an electrophilic oxidant that can directly oxidize phenol molecules solubilized in the solution resulting in some degradation of phenol (Equation (2-2))[45].

$$O_3 + phenol \rightarrow CO_2 + H_2O + \text{intermediates} \quad (2\text{-}2)$$

The pH of the point of zero charge (pH_{pzc}) of GO/MgO NCs is determined to be 9.7 [77]. The pH values of the solutions increased from pH =7 to pH ≥ 7.6 within the first minutes of catalyst addition. Similar results have been reported by previous research [89]. At pH = 7 and higher, phenolate is the dominant species that can react with ozone six orders of magnitude faster than phenol [90]. The electrophilic attack of ozone can take place on the *ortho* and *para* positions of the aromatic ring of phenol [91]. If the attack occurs on the *ortho* position, $^1O_2$ will release and catechol and hydroquinone are generated as products (Figure 2.4, reaction pathway 1) [92]. Phenols quench $^1O_2$ with very low rate constants that have no significant effect on $^1O_2$ yield [93].

Different pathways are proposed when ozone attacks on the *para* position [94]. The first pathway is the cleavage of $^1O_2$ from a primary ozonide (Figure 2.4, reaction pathway 2). The other pathway leads to the generation of benzoquinone and hydrogen peroxide (Figure 2.4, reaction pathway 3). It is reported that hydroquinone and p-benzoquinone are the main by-products of direct

and catalytic ozonation of phenol [26,95]. Since these intermediates are scavengers for $^{\bullet}O_2^-$ [88], it can be confirmed that $^{\bullet}OH$ and $^1O_2$ are the main reactive species in ozonation of phenol using GO/MgO NCs as a catalyst.

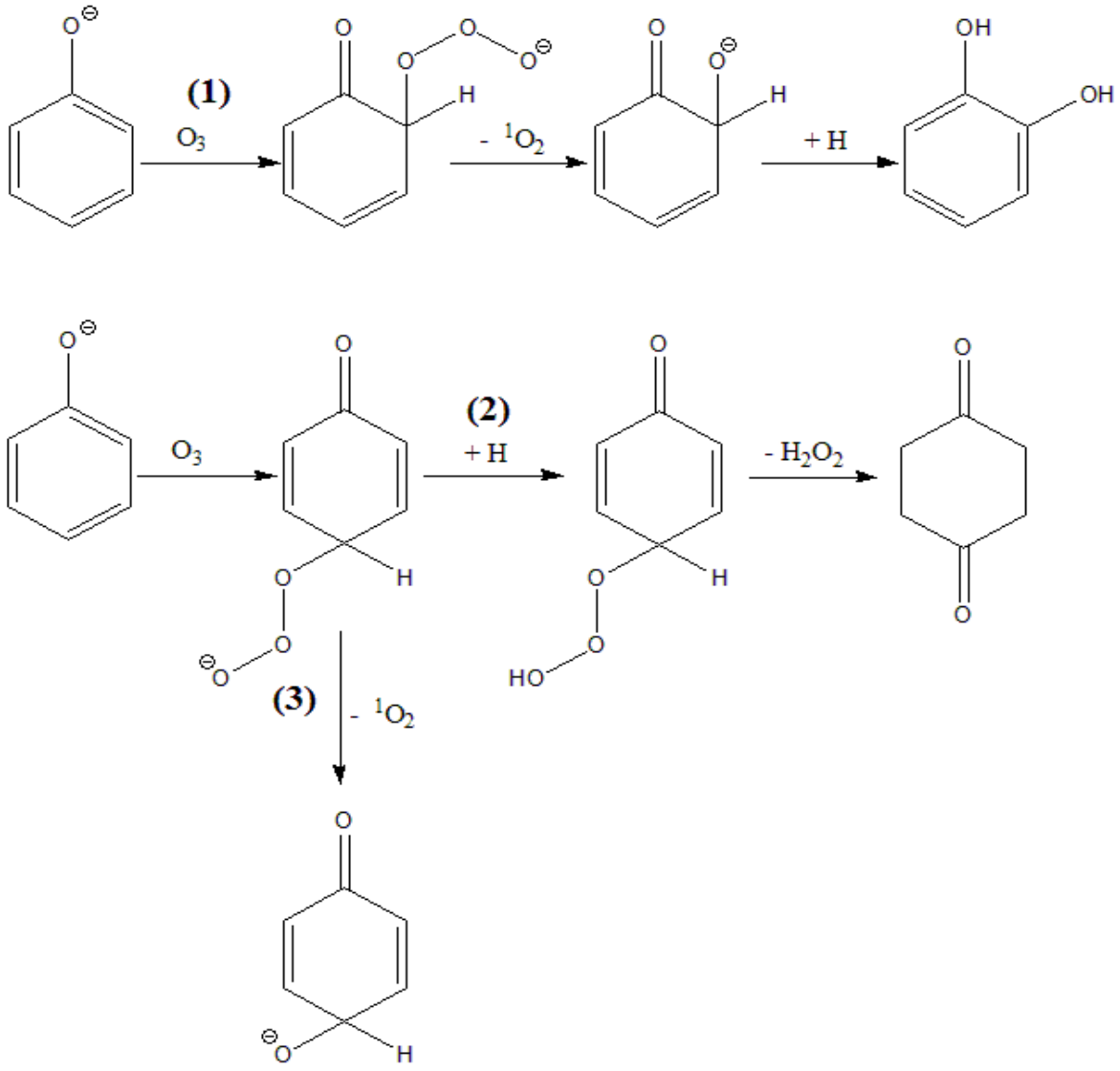

Figure 2.4 Proposed reaction pathways when ozone attacks on *ortho* and *para* positions of the phenol. (ChemDraw Pro 8.0)

GO could also help to achieve the local enrichment of ozone molecules on its surface by an association of the high delocalized π electrons on the basal planes [73] and multiple containing

oxygen groups [96] on the surface of GO that can interact with ozone and generate a large amount of hydroxyl radicals. Delocalized π electrons on the surface of GO have a high affinity toward the ozone molecules and form an electron acceptor-donor complex with H_2O molecules (Equations (2-3)-(2-6)) yielding hydroxyl ions, and subsequently initiate the adsorbed ozone decomposes into the surface bound —O radicals [85]. Ozone decomposition surface reaction for pH = 2-6 (Eqs.4-6) and pH > 6 (Equations (2-7)-(2-9)) are shown below:

$$GO_{\pi} + 2H_2O \rightleftarrows GO_{\pi} - H_3O^+ + OH^- \quad (2\text{-}3)$$

$$O_3 + GO \rightleftarrows O_3 - GO \quad (2\text{-}4)$$

$$O_3 - GO \rightleftarrows O - GO + O_2 \quad (2\text{-}5)$$

$$O_3 + O - GO \rightleftarrows 2O_2 + GO \quad (2\text{-}6)$$

$$OH^- + GO \rightleftarrows OH - GO \quad (2\text{-}7)$$

$$O_3 + OH - GO \rightleftarrows {}^{\bullet}O_3 - GO + {}^{\bullet}OH \quad (2\text{-}8)$$

$${}^{\bullet}O_3 - GO \rightleftarrows {}^{\bullet}O - GO + O_2 \quad (2\text{-}9)$$

GO contains various oxygen-containing functional groups that could interact with ozone and yield hydroxyl radicals. In order to investigate the functional groups of GO and GO/MgO NCs, ATR-FTIR spectroscopy was used in the wavenumber range of 4000-450 cm^{-1} and the results are shown in Figure 2.5(a).

The broad band in the range of 3100-3500 cm^{-1} corresponds to the O—H stretching [97]. The peaks located at 1225 cm^{-1}, 1055 $cm^{-1,}$ and 1720 cm^{-1} are assigned to C—OH, C—O, and C=O stretching, respectively. Other peaks that appear at 1390 cm^{-1} and 1630 cm^{-1} were observed to attribute to C—O and C=C bonds of the sp^2 carbon skeletal [51,98]. Similarly, after coating

MgO on the surface of GO, the same functional groups mentioned above were found around the corresponding wavenumber with weaker intensity. The sharp band around 3700 cm^{-1} on MgO was related to the presence of hydroxyl groups that comes from the reaction between the surface of MgO NPs with water or defects [47]. On the other hand, after the catalytic ozonation process using GO/MgO NCs as a catalyst, some peaks such as 1055 cm^{-1} and 1390 cm^{-1} (C—O) were not detected. Therefore, it can be concluded that these oxygen-containing groups over GO could interact with ozone and generate ROS. Liu et al. [96] used GO as a catalyst in the synergistic removal of DEET. He reported that oxygen-containing functional groups on GO could interact with ozone and yield abundant $^{\bullet}OH$.

TGA and DTG were employed to investigate the chemical composition and thermal stability of GO and GO/MgO NCs before and after the catalytic ozonation process. As shown in Figure 2.5(b), an initial weight loss for the GO curve at a temperature below 130°C could be ascribed to the removal of the physically adsorbed water molecules [53]. This weight loss is more visible on the DTG curve for GO. The mass loss for a temperature between 180-300 °C is ascribed to the decomposition of labile oxygen-containing functional groups, such as hydroxyl, epoxy, and carboxyl groups between layers of GO [99]. TGA and DTG curves of GO are very sharp at those temperatures. The curve of GO/MgO NCs before the catalytic ozonation process displays an initial decomposition above 220 °C and the maximum weight loss occurs at 630 °C, presumably due to pyrolysis of the labile oxygen-containing functional groups and the decomposition of the carbon structures [100–102]. The catalyst after the catalytic ozonation process showed very high thermal stability and the total weight lost was about 35% compared to 53% for the catalyst before the catalytic ozonation process. As is shown in Figure 2.5(b) for GO/MgO after the catalytic

ozonation, no sharp dip on the DTG curve is observed. Previous reports indicate that this smaller mass-loss can be due to the absence of most oxygen functional groups [103,104].

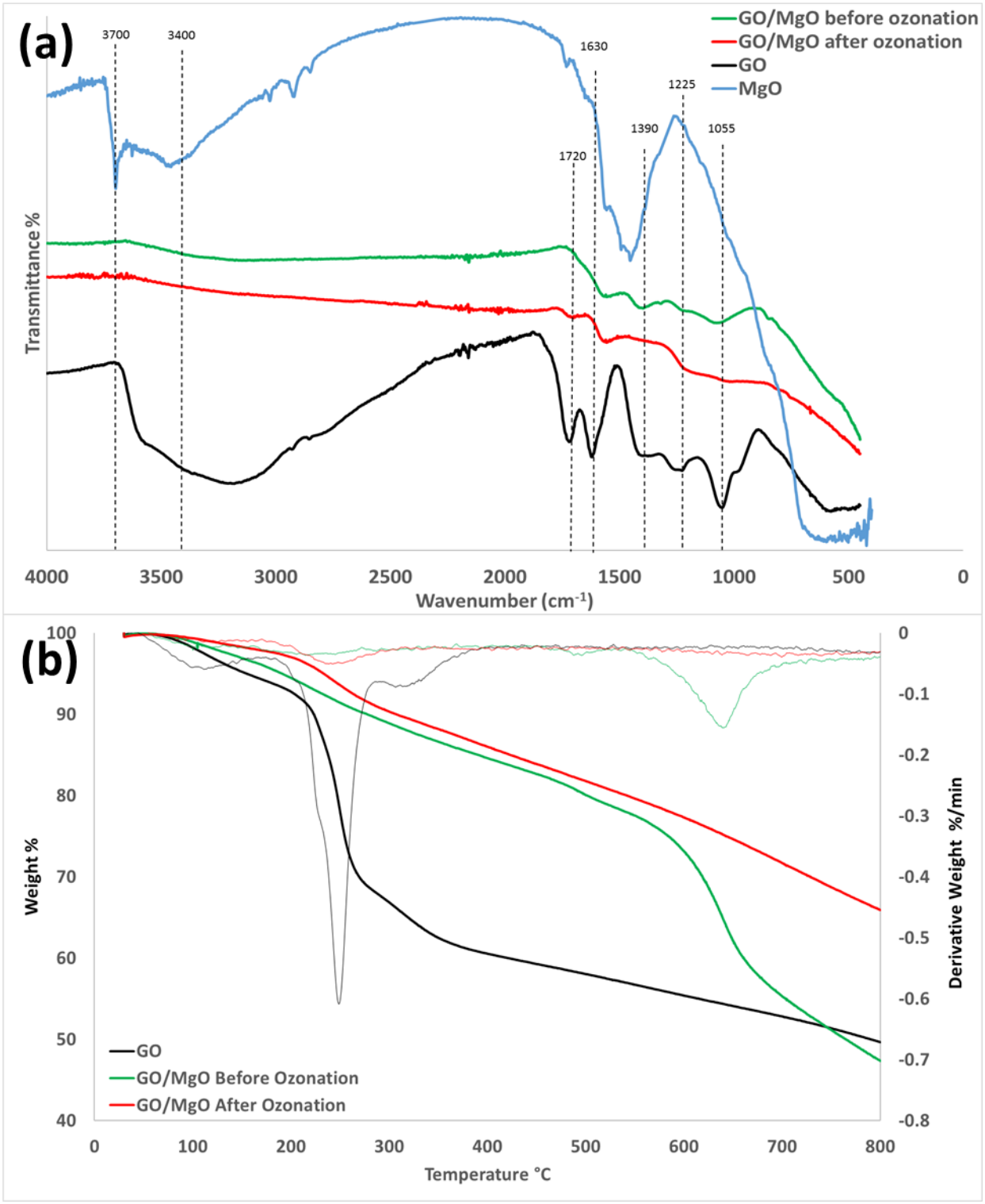

Figure 2.5 a) FTIR spectra of GO and GO/MgO NCs before and after ozonation. b) Thermal gravimetric analysis (TGA) of GO, and GO/MgO NCs before and after catalytic ozonation process

While the prior discussed pathways highlight GO interactions to promote free radicals, other pathways are likely important. Metal oxides such as MgO have the ability to exchanges ligands on their Lewis acid sites ($MgO-S$) and donate sites for reaction with ozone [45,85] . The following mechanisms are suggested for the oxidation of phenol in catalytic ozonation:

$$MgO-S+\ O_3 \rightarrow MgO-S^{O_3} \quad (2\text{-}10)$$

$$MgO-S^{O_3} \rightarrow\ MgO-S^{O^{\bullet}}+\ O_2 \quad (2\text{-}11)$$

$$MgO-S^{O^{\bullet}}+2H_2O\ +\ O_3 \rightarrow\ MgO-S^{^{\bullet}OH}+3^{\bullet}\mathrm{OH}+O_2 \quad (2\text{-}12)$$

$$MgO-S^{O^{\bullet}}+phenol\ \rightarrow\ CO_2+\ H_2O+intermediates \quad (2\text{-}13)$$

According to Equations (2-10)-(2-13), ozone molecules and hydroxyl groups on MgO surface form hydrogen bonds [105,106]. Thereafter, the bonded ozone partly decomposes to atomic oxygen that can expedite phenol degradation [106].

2.3.4 Effect of ozone dosage on catalytic ozonation process

The effect of ozone dosage on the catalytic ozonation of phenol, with a dosage range from 20 to 120 mg/h was investigated, and the results are presented in Figure 2.6(a). It is shown that the removal of phenol increased with the increase of ozone dosage. Ozone can decompose phenol and also is the initiator for the production of reactive oxygen species. Therefore, an increased amount of ozone in the presence of GO/MgO NCs makes more ozone molecules available to contribute to the reaction and enhancement of ROS production. Based on the data shown in Figure 2.6(a), phenol

degradation in the O_3/GO/MgO process at 60 minutes increased from around 31.1% at the ozone dosage of 20 mg/h to 84.4% when the dosage of ozone was increased to 85 mg/h. After a further increase in ozone dosage from 85 to 100 and 125 mg/h, however, the phenol removal percentage remained almost unchanged. Hence, the optimum catalyst dosages for removal of 500 mg/L of phenol was selected at 85 mg/h of ozone and used in the following experiments.

2.3.5 Effect of GO/MgO NCs dosage on catalytic ozonation process

The performance of catalytic ozonation for removal of phenol was studied in the presence of various dosage of GO/MgO NCs, in the range of 0-1 g/L. According to Fig 3.6b, GO/MgO NCs as a catalyst improved the oxidation of phenol in the ozonation process. The phenol removal increased from 60.8% in the absence of the catalyst to 90.9% in the presence of 0.5 g/L GO/MgO NCs. Thereafter, it improved slightly to over 94% when the GO/MgO NCs dosage was increased to 0.75 g/L. Similarly, other researchers have reported increased oxidation efficiency in graphene oxide[96] and metal-based [105] catalytic oxidation process with an increase of catalyst dosage. A further increase in GO/MgO NCs dosage to 1 g/L did not increase the phenol removal efficiency. This can be explained that when the catalyst amount was above the optimal value during catalytic ozonation, GO/MgO NCs may block the ozone mass transfer process or excess GO/MgO NCs may quench the active species, such as $^{\bullet}OH$ [96,107]. According to experimental results, 0.5 g/L of GO/MgO NCs was selected as the optimum catalyst dosage for the removal of phenol in catalytic ozonation for the subsequent experiments.

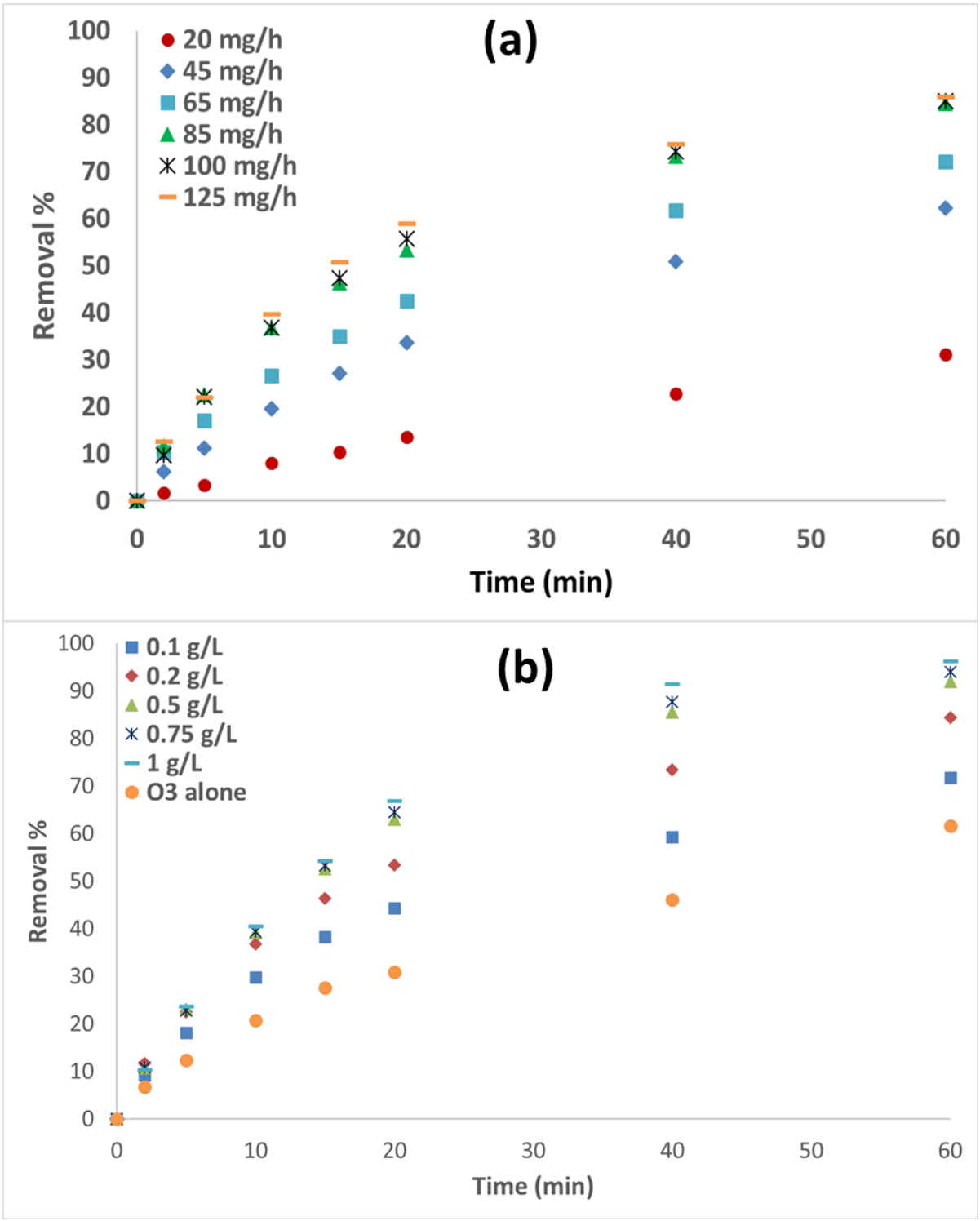

Figure 2.6 a) Effect of ozone dosage on phenol removal in the O_3/GO/MgO process (experimental conditions: GO/MgO: 0.2 g/L, phenol concentration: 500 mg/L, Volume: 100 mL, Temperature: 20 °C, and pH: uncontrolled). b) Effect of catalyst dosage on phenol removal in the O_3/GO/MgO

process (experimental conditions: the flowing rate of O_3: 85 mg/h, phenol concentration: 500 mg/L, Volume: 100 mL, Temperature: 20 °C, and pH: uncontrolled).

2.3.6 Kinetic of degradation of phenol in catalytic ozonation using GO/MgO as a catalyst

Based on experimental data, the efficiency of phenol removal after an increase in ozone dosage of 85 mg/h and catalyst dosage of 0.5 g/L was insignificant, therefore they were considered as the optimum dosages. The kinetic of degradation of phenol in catalytic ozonation process was investigated at the selected experimental conditions (the flow rate of O_3: 85 mg/h, GO/MgO NCs dosage: 0.5 g/L, respectively; pH: uncontrolled, phenol concentration: 500 mg/L, and reaction time: 0-60 min). The pseudo-first order reaction model is used to represent the ozonation and catalytic ozonation by the following Equation (2-14) [27]:

$$kC_A = -dC_A/dt \quad (2\text{-}14)$$

where k (min^{-1}) is the kinetic constant of the pseudo-first order catalytic ozonation, and C_A is the concentration of phenol. The logarithmic plot of the concentration of phenol is shown in Figure 2.7.

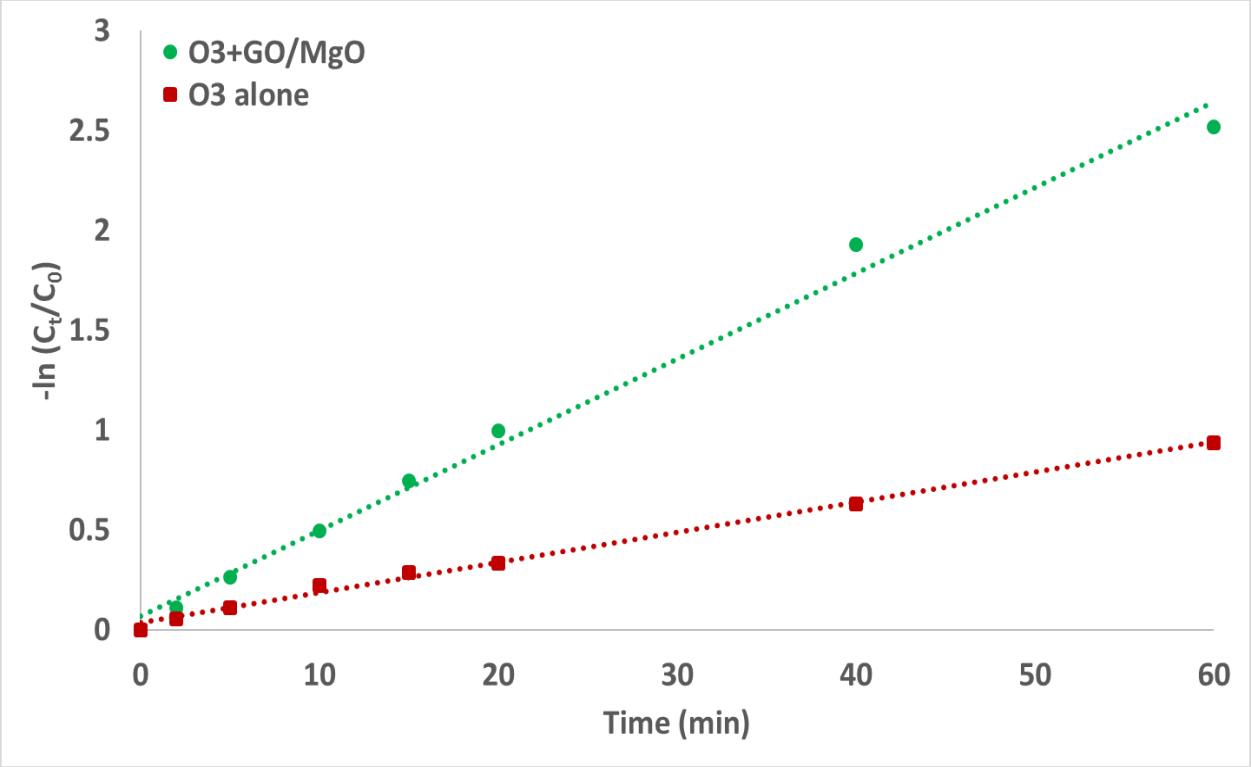

Figure 2.7 Pseudo-first order kinetics for phenol degradation in ozonation and catalytic ozonation processes (experimental conditions: the flowing rate of O_3: 85 mg/h, GO/MgO NCs dosage: 0.5 g/L, phenol concentration: 500 mg/L, Volume: 100 mL, Temperature: 20 °C, and pH: uncontrolled)

The determination coefficient (r^2) was higher than 0.99 for both ozonation and catalytic ozonation processes. Based on the experiment data the k values were determined 0.0151 and 0.0566 min^{-1} for ozonation alone and catalytic ozonation using GO/MgO as a catalyst, respectively. Apparently, the kinetic constant of GO/MgO catalyst is about 2.8 times as high as that of ozonation alone. These results suggest that the synthesized GO/MgO NCs can be used as an effective catalyst for the ozonation degradation of phenol with the high catalytic ability.

2.3.7 Effect of pH on the catalytic ozonation process

The pH is an important parameter affecting catalyst surface property, mechanism of ozone decomposition, and ozone stability [108–110]. Specifically, at higher pHs ozone decomposition

and hydroxyl radical generation accelerate [36]. Therefore, it is necessary to examine the influence of pH on phenol removal during the O_3/GO/MgO process. When pH was uncontrolled, the initial pH of the solution was increased to ≥ 7.6 after adding GO/MgO NCs. It was also variable during the catalytic ozonation process. Figure 2.8(a) shows the pH of the solution during different reaction times. The pH value decreased gradually to 2.9 after 60 minutes, that is attributed to the breaking of the aromatic ring of phenol into small chain fatty acids such as acrylic acid, malonic acid, acetic acid, and oxalic acid [111]. The degradation status of phenol by the O_3/GO/MgO process at different pH conditions is shown in Figure 2.8(b). It can be seen that the removal of phenol was quite similar at pH of 5, 6, 7, and 8. As the pH increases, the removal of phenol increased from 82.8% to 88.6, 92.6, and 97.4 % at pH of 9, 10, and 11, respectively. Similar results were reported that the high solution pH enhanced the removal efficiency of *p*-CNB in sole ozonation and catalytic ozonation [112]. Ozone decomposition significantly accelerated at higher pH because OH^- ions enhance ozone molecules transformation into $^{\bullet}OH$ and $^{\bullet}O$-GO radicals (Eqs.7-9). Therefore, more ROS participate in the catalytic ozonation process and the oxidation rate of the target contaminants could be increased [113].

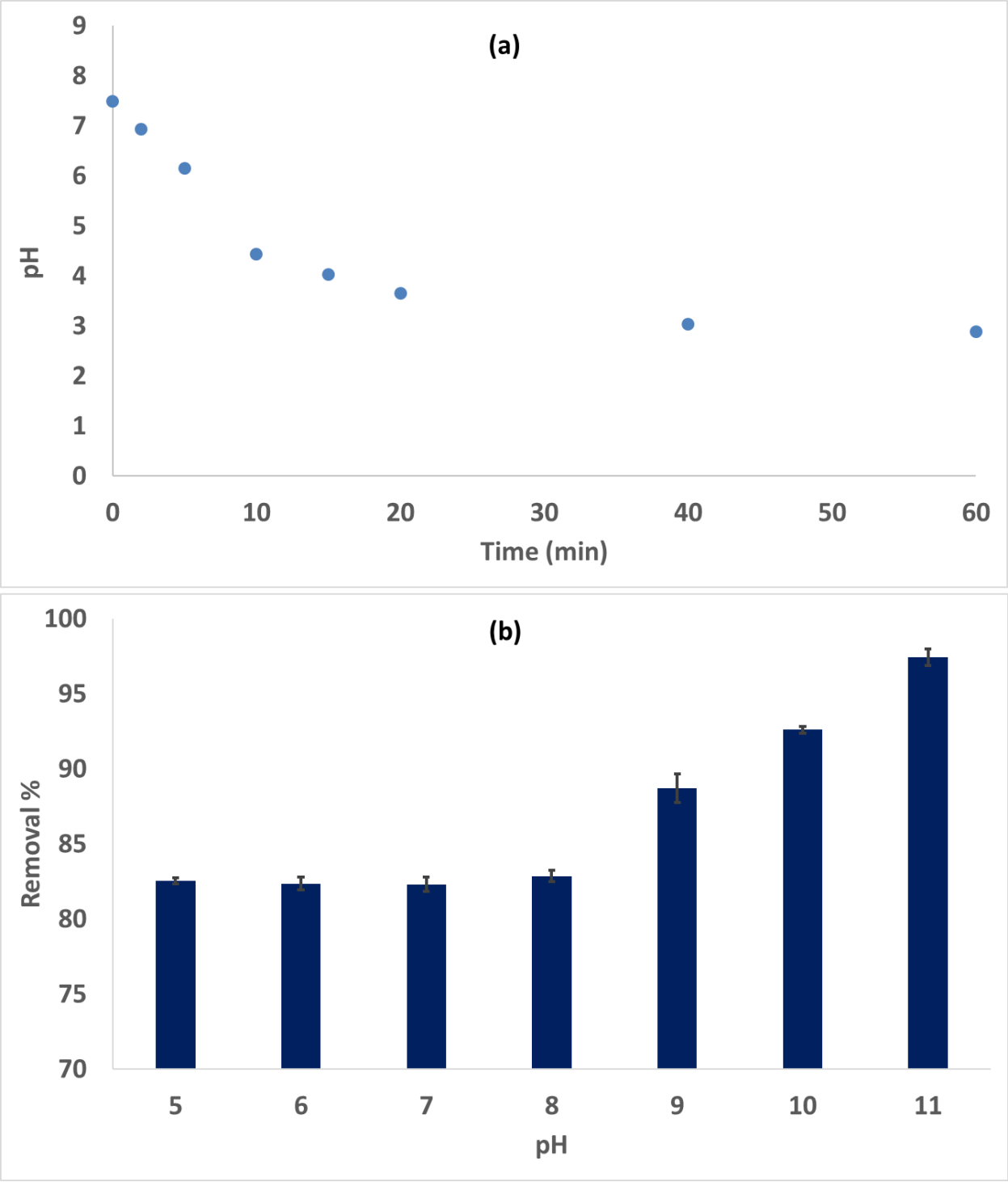

Figure 2.8 (a) Variation of pH value for the phenol solutions during O_3/GO/MgO process. The initial pH is uncontrolled. (b) Removal of phenol in O_3/GO/MgO process at various pH values. (experimental conditions: the flowing rate of O_3: 85 mg/h, GO/MgO dosage: 0.5 g/L, phenol concentration: 500 mg/L, Volume: 100 mL, Temperature: 20 °C)

2.4 Conclusion

In this chapter, GO/MgO NCs were applied as a catalyst for the ozonation process for removal of phenol. The experimental results confirmed GO/MgO NCs as a catalyst significantly increased phenol degradation relative to controls in the ozonation process. The analysis of reactive oxygen species in catalytic ozonation showed both $^{\bullet}OH$ and $^{1}O_2$ are the dominant reactive species in the reactions. A pseudo-first order reaction model was applied to represent catalytic ozonation and the pseudo rate constant (k) of phenol degradation in this study was found to be 0.0566 min^{-1} under the following experimental conditions: phenol and GO/MgO NCs concentrations= 500 mg/L, 0.5 g/L, respectively; O_3 dose= 85 mg/h; reaction time = 60 min. In summary, this study shows that a GO/MgO/O_3 AOP is very efficient for the removal of potentially toxic and treatment inhibitory compounds such as phenol. Such a process can thus be considered as a viable treatment option in wastewaters bearing such compounds.

CHAPTER 4

Central composite design and surface response methodology for catalytic advanced oxidation of phenol using GO/MgO nanocomposites

3.1 Introduction

In Chapter 3, the effect of certain parameters on the degradation of phenol in catalytic ozonation using GO/MgO NCs as a catalyst was investigated individually. To investigate the effect of each parameter on the removal of phenol, more than two hundred tests were performed. In each set of experiments, changes in the value of one parameter were studied while the other parameters are constant. Then, the optimal value was selected based on the results of experiments. In this method, the phenol removal was calculated without considering the interaction between parameters. Therefore, each parameter has been studied individually, which gives less information on the relationship between experimental parameters. In the following study, we are evaluating the relationship between independent parameters time, ozone dosage, and catalyst dosage as a function of phenol removal (%). For this purpose, the design of experiments (DOE) which is introduced by Fisher [114] combined with response surface methodology (RSM) was applied using Minitab 18 software.

DOE gives a meaningful comparison between so-called classical experimental design (one factor at a time) and statistically designed experiments. DOE is a planned approach for determining cause and effect relationships. Therefore, DOE helps to (a) reduce the number of experiments or trials, (b) simultaneously change all factors that affect the results, and (c) select a clear strategy

that gives reliable solutions to be obtained after each sequence of experiments [115]. The design and statistical analysis of experiments have resulted in the development of RSM used for process optimization. RSM is the applicable design of experiments in the chemical industry [116]. RSM is a hybrid of mathematical and statistical methods helpful for designing experiments, creating models and evaluating the problems in which an output of interest is impacted by various independent variables while the optimum conditions are determined from desirable output. This method combined with Analysis of Variance (ANOVA) gives very constructive and useful information about the main effects and interactions between variables and their contribution to the response.

ANOVA is one of the most widely used statistical methods for hypothesis testing. ANOVA tests the hypothesis that the means of two or more populations are equal. ANOVAs assess the importance of one or more factors by comparing the response variable means at different factor levels. The null hypothesis states that all population means (factor level means) are equal while the alternative hypothesis states that at least one is different [117]. To determine whether any of the differences between the means are statistically significant, the probability value (*P*-value) is compared to the significance level to assess the null hypothesis. The null hypothesis states that the population means are all equal. Usually, a significance level (α) of 0.05 works well. A significance level of 0.05 indicates a 5% risk of concluding that a difference exists when there is no actual difference. An ANOVA with a 95% confidence level shows the significance of the independence of variables and their interactions [118].

3.2 Methods

To understand the relationship between effective parameters for removal of phenol a second-degree polynomial equation was applied. Three design factors were selected, namely, time (t),

ozone dosage (O_3), and catalyst dosage (C) using the response surface methodology coupled with central composite design (CCD) to study optimization of phenol removal (%). The RSM coordinated with CCD is a common methodology due to lower relative error in terms of experimental combinations and it expresses well the complex functions of the response[119]. As is shown in Table 3.1 Design factor levels were coded -α (Lowest), -1 (low), 0 (central point), +1 (high) and +α (highest). This RSM was applied to the experimental data obtained using the statistical software, Minitab® 18 [120]. The summary of the design of experiments is presented in

Table 3.2.

Table 3.1 Design matrix for the CCD for the catalytic ozonation of phenol

Factor	Unit	Levels				
		-α	-1	0	+1	+α
Time	min	26.36	40	60	80	93.6
Ozone	mg/h	46.3	60	80	100	113.6
Catalyst	g/L	0.33	0.4	0.5	0.6	0.66

Table 3.2 Summary of experimental design

Run	**Ozone (mg/h)**	**Time (min)**	**Catalyst (g/L)**
1	100	80	0.6
2	80	60	0.5
3	60	40	0.6
4	80	60	0.5

5	80	60	0.5
6	60	40	0.6
7	80	60	0.5
8	80	60	0.5
9	100	80	0.6
10	80	93.6	0.5
11	113.6	60	0.5
12	100	40	0.6
13	100	80	0.4
14	100	40	0.6
15	46.3	60	0.5
16	80	93.6	0.5
17	100	40	0.4
18	60	40	0.4
19	80	60	0.5
20	80	60	0.5
21	80	60	0.66
22	80	26.3	0.5
23	80	60	0.33
24	60	80	0.4
25	80	60	0.5
26	80	60	0.33
27	80	26.3	0.5
28	80	60	0.66
29	100	80	0.4
30	100	40	0.4
31	60	80	0.4
32	80	60	0.5
33	60	40	0.4
34	80	60	0.5
35	80	60	0.5

36	60	80	0.6
37	46.3	60	0.5
38	80	60	0.5
39	113.6	60	0.5
40	60	80	0.6

The generalized second-order polynomial model proposed for the response surface analysis was given as follows (Equation (3-1)) [121]:

$$y = \beta_0 + \sum_{i=1}^{k} \beta_i x_i + \sum_{j=1}^{k} \sum_{i=1}^{k} \beta_{ij} x_i x_j + \sum_{i=1}^{k} \beta_{ii} x_i^2 + \varepsilon \quad (3\text{-}1)$$

where y is the predicted response, x_i, x_j are the coded values of the independent variables, β_0 is the regression coefficient for the intercept, β_i are the linear regression coefficients, β_{ij} are the regression coefficients for interaction terms, β_{ii} are the quadratic regression coefficients, ε represents the random error, and k is the number of factors. In this study, phenol removal (%) is the predicted response. The regression equation for removal with three studied variables as shown in Equation (3-2):

$$\widehat{\%} = \beta_0 + \beta_1 C + \beta_2 O_3 + \beta_3 t + \beta_4 (C.O_3) + \beta_5 (C.t) + \beta_6 (O_3.t) + \beta_7 O_3^2 + \beta_8 C^2 + \beta_9 t^2 \quad (3\text{-}2)$$

ANOVA testing was used to examine the quality of the model by determining the degree of confidence in the results. In statistical hypothesis testing, the *P*-value is the probability when the null hypothesis is true, the statistical summary would be greater than or equal to the actual observed results. Based on the *P*-value, the coefficients are chosen, then each quadratic equation is written according to the obtained coefficients. When the *P*-value ≤ α, the differences between

some of the means are statistically significant. If the *P*-value is less than or equal to the significance level, the null hypothesis is rejected and it is concluded that not all of the variable means are equal. When the *P*-value > α, the differences between the means are not statistically significant. If the *P*-value is greater than the significance level, there is not enough evidence to reject the null hypothesis that the variable means are all equal. The $P < 0.05$ indicates that the model terms were significant. Some concepts of regression are listed in Equations (3-3)-(3-9) :

$$SSR = \sum(\hat{Y}_i - \bar{Y})^2 \quad (3\text{-}3)$$

$$SSE = \sum(Y_i - \hat{Y}_i)^2 \quad (3\text{-}4)$$

$$SST = SSR + SSE \quad (3\text{-}5)$$

$$SST = \sum(Y_i - \bar{Y})^2 \quad (3\text{-}6)$$

$$R^2 = SSR/SST \quad (3\text{-}7)$$

$$DF = n - k - 1 \quad (3\text{-}8)$$

$$Adjusted\ R^2 = 1 - (1 - R^2)\ \frac{n-1}{n-k-1} \quad (3\text{-}9)$$

$$MS = SS/DF \quad (3\text{-}10)$$

In Equation (3-3), *SSR* is the sum of squares due to regression, it is the sum of the difference between the predicted value and the mean of the dependent variable, $\hat{Y}$ is the predicted value of *Y* for a given value of *X* variables, $\bar{Y}$ is the mean value of *Y* (observation). *SSE* is the sum of squares due to error (Equation (3-4)). In Equations (3-5)-(3-6), *SST* is the sum of squares total. *DF* is the degrees of freedom in Equation (3-8), where *n* is the number of observations, *k* is the number of

explanatory (*X*) variables. As *DF* decreases (i.e. more variables added to a given model) R^2 will only increase (Equation (3-9)). In Equation (3-10), mean square represent by *MS* and equal to ratio of the *SS* and *DF*.

The quality of the model was justified based on the R^2 value. A high R^2 value close to one shows a good agreement between the calculated and observed results within the range of the experiment and also shows desirable and reasonable agreement with the *adjusted*-R^2 value [122]. R^2 determines how well the model fits the data. The higher the R^2 value, the better the model fits the data. *Adjusted*-R^2 is the percentage of the variation in the response that is explained by the model and it is less than R^2.

3.3 Results and discussion

The Minitab 2018 software was used in this study to develop a quadratic polynomial equation that links the response phenol removal (%) with three studied variables as shown below in Equation (3-11). The coefficients and the *P*-Value for each term are shown in

$$\text{Removal \%} = 26.6 + 0.175\ O_3 + 1.306\ t - 81.9\ C - 0.00043\ O_3.O_3 - 0.00547\ t.t + 46.5\ C.C - 0.00285\ O_3.t + 0.659\ O_3.C + 0.040\ t.C \quad (3\text{-}11)$$

Table 3.3.

Table 3.3 Coefficient and *P*-value for the terms

Term	**Coef**	***P*-value**
Constant	26.6	0.000

Ozone	0.175	0.000
Time	1.306	0.000
Catalyst	-81.9	0.000
Ozone*Ozone	-0.00043	0.701
Time*Time	-0.00547	0.000
Catalyst*Catalyst	46.5	0.302
Ozone*Time	-0.00285	0.064
Ozone*Catalyst	0.659	0.034
Time*Catalyst	0.040	0.893

The results indicate that the R^2 value is more than 0.94 and *Adjusted-*R^2 is in a reasonable agreement with R^2. The *Predicted-*R^2 value was found 0.89 that is close to *Adjusted-*R^2 which was 0.93. This result confirms the existence of a good correlation between the data involved in the adopted model [123].

Figure 3.1(a) shows the residuals vs. the fitted plot. Plotting residuals versus the value of a fitted model verify the assumption that the residuals are randomly distributed and have constant variance. Ideally, the points should fall randomly on both sides of 0, with no recognizable patterns in the residual data. As is shown, the residual data that are evenly and randomly distributed about the "0" axis. Figure 3.1(b) shows a normal probability plot of the residuals. The normal probability plot displays the residuals versus their expected values when the distribution is normal. This plot verifies the assumption that the residuals are normally distributed. The normal probability plot of the residuals should approximately follow a straight line. Figure 3.1(b) shows the results are normal and the outliers are absent in the model. Figure 3.1(c) is a histogram of the residual versus

frequency. The histogram of the residuals can be used to check whether the variance is normally distributed. The symmetric bell-shaped histogram, which is evenly distributed around zero, indicates that the normality assumption is likely correct. The figure shows a normal distribution of residuals produced by the model for the removal of phenol (%). This means that in that the model explains all trends in the dataset. Figure 3.1(d) shows residuals versus order. Independent residuals show no trends or patterns when displayed in time order. Patterns in the data may indicate that residuals near each other may be correlated, and thus, not independent. Preferably, the residuals on the plot should fall randomly around the centre line. As it is shown in Figure 3.1(d), no trend is observed.

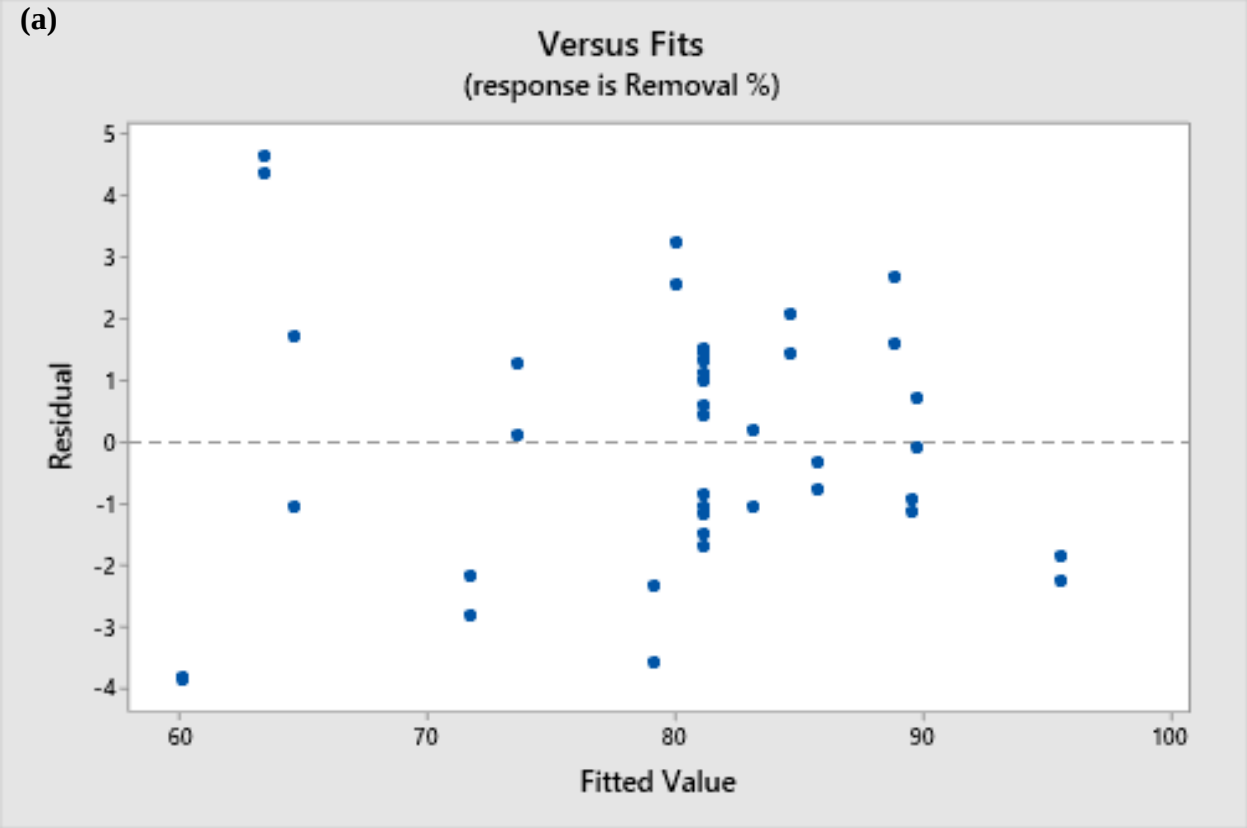

(b)

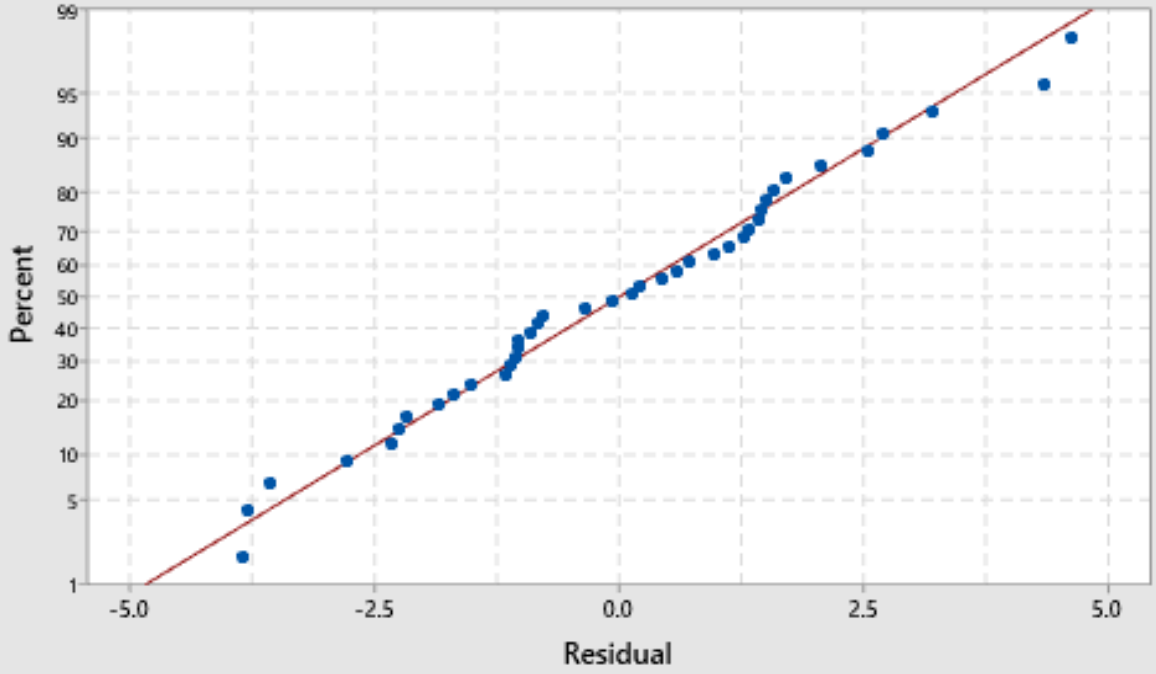
Normal Probability Plot
(response is Removal %)
Percent
99
95
90
80
70
60
50
40
30
20
10
5
1
-5.0
-2.5
0.0
2.5
5.0
Residual

(c)

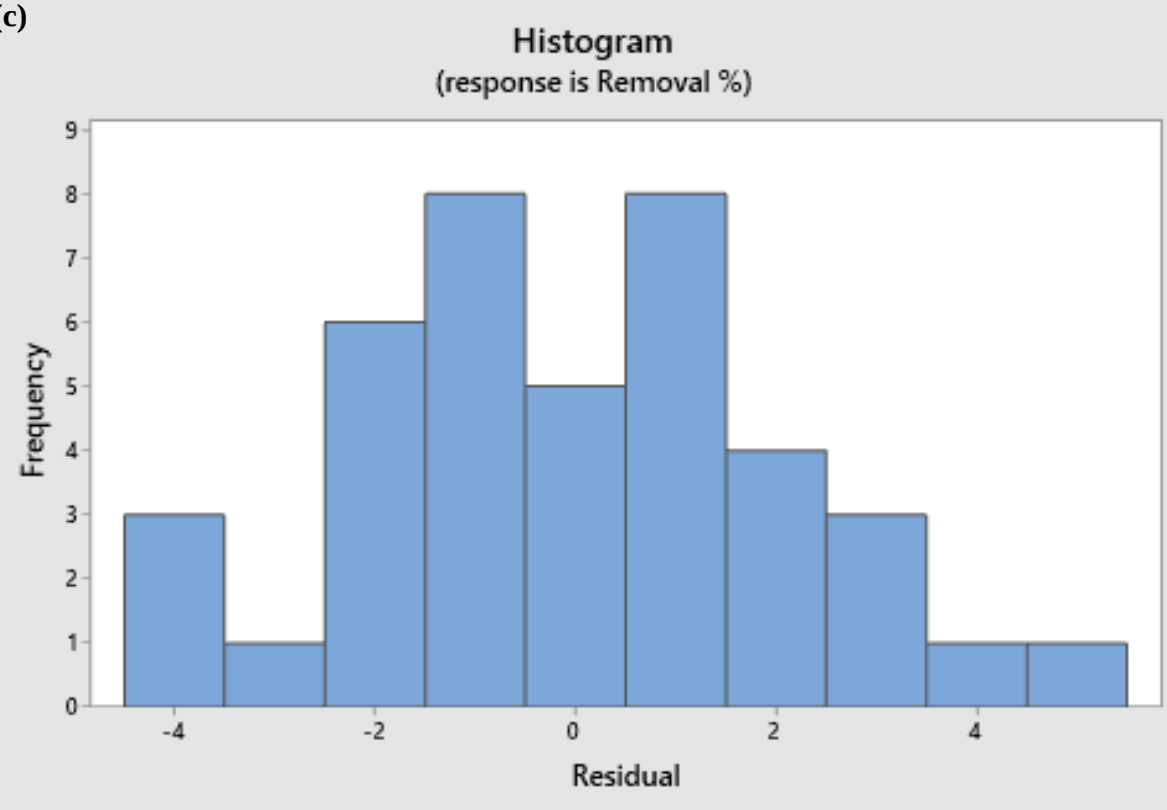
Histogram
(response is Removal %)
Frequency
9
8
7
6
5
4
3
2
1
0
-4
-2
0
2
4
Residual

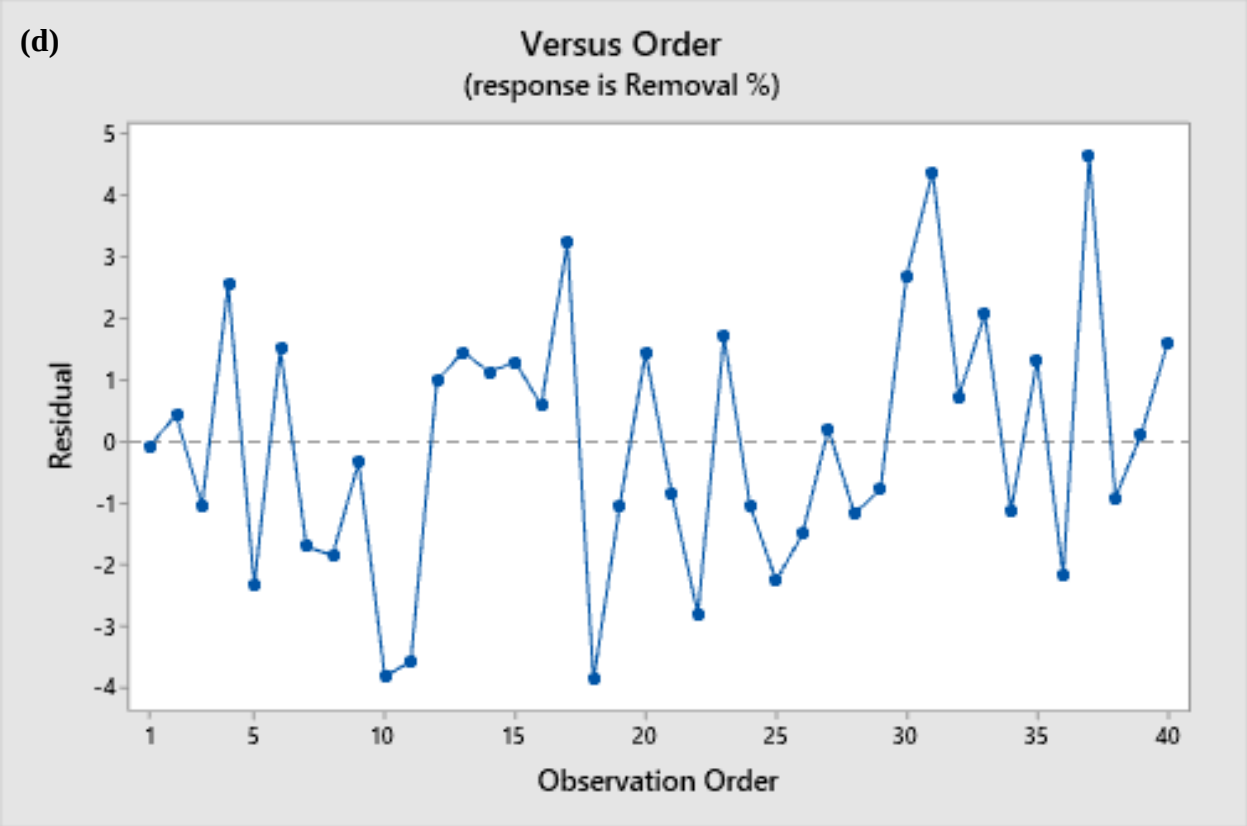

Figure 3.1 Plot of raw residuals vs case number (a), Probability as a function of residual (b), Histogram graph (c), and observation order vs residual (d)

The variables of the ANOVA are shown in Table 3.4. *F*-value and *P*-value were used to represent the importance of the variables in the quadratic model. In addition, the sum of squares (*SS*), degree of freedom (*DF*), and mean squares (*MS*) were calculated. The *MS* value of a model term in an ANOVA table is obtained by dividing SS over *DF* and *F*-value is obtained by dividing *MS* due to the model term by MS due to error. A larger *F*-value and lower *P*-value of a model term in an ANOVA indicate good significance of the term over other variables [124].

Table 3.4 Analysis of variance for the removal of the phenol in the catalytic advanced oxidation process

Source	**DF**	**SS**	**MS**	**F-value**	**P-value**
Model	9	3204.76	356.08	62.99	0.000
Linear	3	3004.55	1001.52	177.15	0.000
Ozone	1	767.11	767.11	135.69	0.000
Time	1	2130.64	2130.64	376.87	0.000
Catalyst	1	106.80	106.80	18.89	0.000
Square	3	151.44	50.48	8.93	0.000
Ozone*Ozone	1	0.85	0.85	0.15	0.701
Time*Time	1	137.87	137.87	24.39	0.000
Catalyst*Catalyst	1	6.24	6.24	1.10	0.302
2-Way Interaction	3	48.77	16.26	2.88	0.053
Ozone*Time	1	20.86	20.86	3.69	0.064
Ozone*Catalyst	1	27.80	27.80	4.92	0.034
Time*Catalyst	1	0.10	0.10	0.02	0.893
Error	30	169.60	5.65		
Lack-of-Fit	5	144.73	28.95		
Pure Error	25	24.88	1.00		
Total	39	3374.36			

In Table 3.4, the *F*-value (62.99) for the model indicates the goodness and usefulness of the presented model. As the significance level is $\alpha = 0.05$, there are 9 degrees (*DF* Model) of

freedom in the numerator, and 30 (*DF* Error) degrees of freedom in the denominator, then the critical *F*-value is equal to 2.21 obtained from *F*-distribution table (Appendix A).

Also, the critical *F*-value is calculated for each factor and equal to 4.17 because the degree of freedom for each factor is equal to 1 and the degree of freedom for the residual is 30. Therefore, an *F*-value greater than the critical *F*-value (4.17) is equivalent to a *P*-value less than α and both mean that the factor is impactful. Pareto chart determines the magnetite and importance of the effect of variables [125,126]. It reveals that factors time, ozone, time*time, catalyst, and ozone*catalyst are the most powerful factors for the removal of phenol in a catalytic advanced oxidation process in a quadratic polynomial equation. Figure 3.2 shows the standardized main effect Pareto chart. The red line on the Pareto chart is drawn at *t*-distribution with degrees of freedom equal to the degrees of freedom for the error term. According to the *t*-distribution table (Appendix B), the *t-value* (the red line) is equal to 2.04 where the degrees of freedom of error term is 30 and α = 0.05. The *t*-value greater than the critical value (2.04) means that the factor is controlling in the equations. The other factors were removed in the model. Finally, the postulated model is validated and can be used for the prediction of responses within the experimental domain as given in Equation (3-12) :

$$\text{Phenol removal \%} = 26.6 + 0.175\ O_3 + 1.306\ t - 81.9\ C - 0.00547\ t*t + 0.659\ O_3*C \quad (3\text{-}12)$$

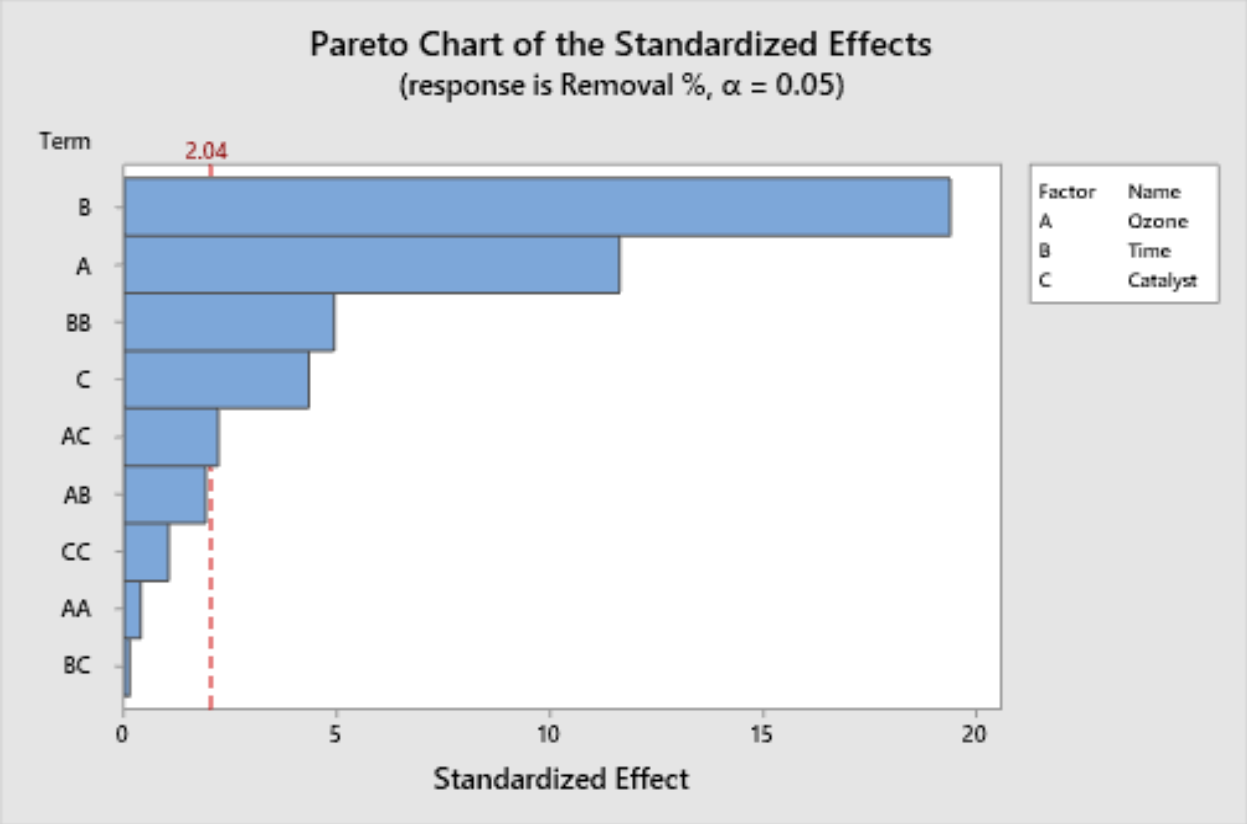

Figure 3.2 Standardized main effect Pareto chart for the Central Composite Design of removal of phenol

Figure 3.3(a) demonstrates the main effect plot for removal. This plot is used to examine the differences between level means for one or more factors. There is the main effect when different levels of a factor affect the response differently. As shown in the Fig 4.3a, ozone = 80 mg/h, time = 60 minutes, and catalyst = 0.5 g/L are effective parameters for removal of 80% of phenol in a catalytic advanced oxidation process.

Figure 3.3(b) shows fitted response surface and contour plots for the removal (%) across variables. The bent nature of the curves is a good indication of the interaction between parameters. In each plot, the interaction of any two variables on the adsorption process is studied keeping the other variables constant.

(a)


Main Effects Plot for Removal %
Data Means
Ozone
Time
Catalyst
Mean
90
85
80
75
70
65
60
55
46 60 80 100 114
26 40 60 80 94
0.33 0.40 0.50 0.60 0.67

(b)


Interaction Plot for Removal %
Data Means
46 60 80 100 114
Catalyst
Ozone
Time
90
75
60
0.33 0.40 0.50 0.60 0.67
26 40 60 80 94
Catalyst
0.33
0.40
0.50
0.60
0.67
Ozone
46
60
80
100
114
Time
26
40
60
80
94

Figure 3.3 Main effects plot and interaction plot for removal of phenol

Figure 3.4 demonstrates the fitted response surface and contour plots for the removal (%) across variables. The bent nature of the curves is a good indication of the interaction between parameters. According to Figure 3.4(a) and Figure 3.4(b), the response surface plots show the relation among the ozone and time, while the catalyst dosage is constant at 0.5 g/L. The increase in phenol removal (%) is observed with rising ozone dosage and time. Figure 3.4(c) and Figure 3.4(d), the response surface plots of the relation among the ozone and catalyst, while the time is constant at 60 minutes. The graphs show phenol removal (%) increases with the increase of ozone and catalyst dosage. Figure 3.4(e) and Figure 3.4(f), the response surface plots of the relation among the time and catalyst. The ozone dosage is constant at 80 mg/h for Figure 3.4(e) and Figure 3.4(f). The graphs show phenol removal (%) increases with the increase of time and catalyst dosage.

(a)

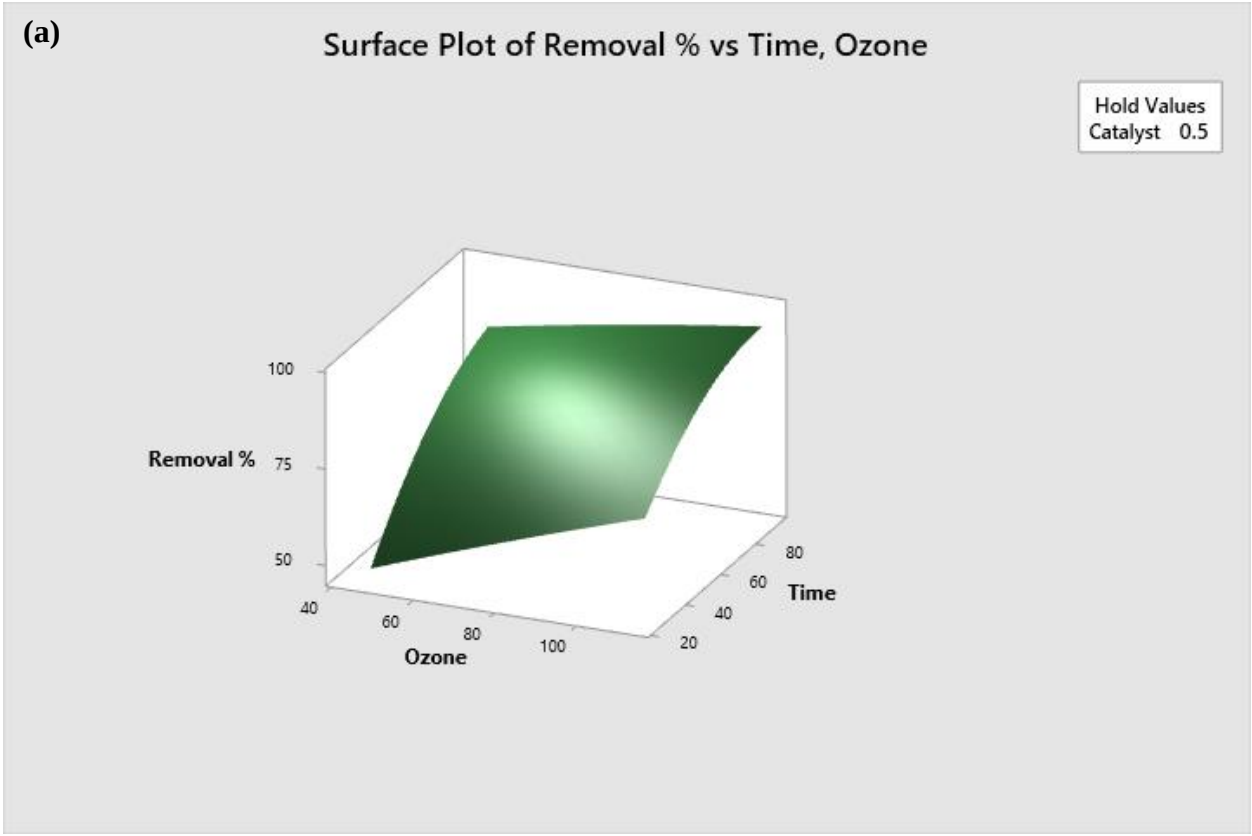
Surface Plot of Removal % vs Time, Ozone
Hold Values
Catalyst 0.5
Removal %
100
75
50
40
60
80
100
Ozone
20
40
60
80
Time

(b)

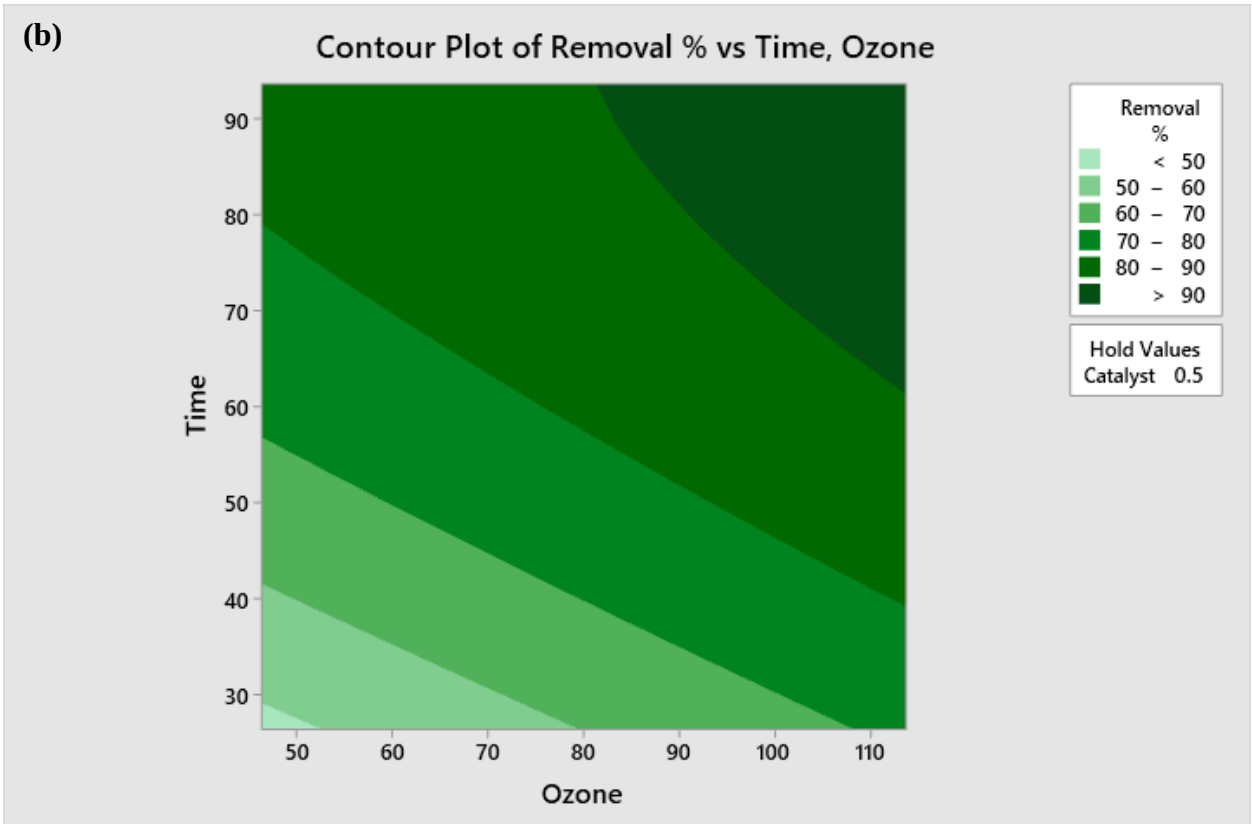
Contour Plot of Removal % vs Time, Ozone
Removal %
< 50
50 – 60
60 – 70
70 – 80
80 – 90
> 90
Hold Values
Catalyst 0.5
Time
90
80
70
60
50
40
30
50
60
70
80
90
100
110
Ozone

(c)

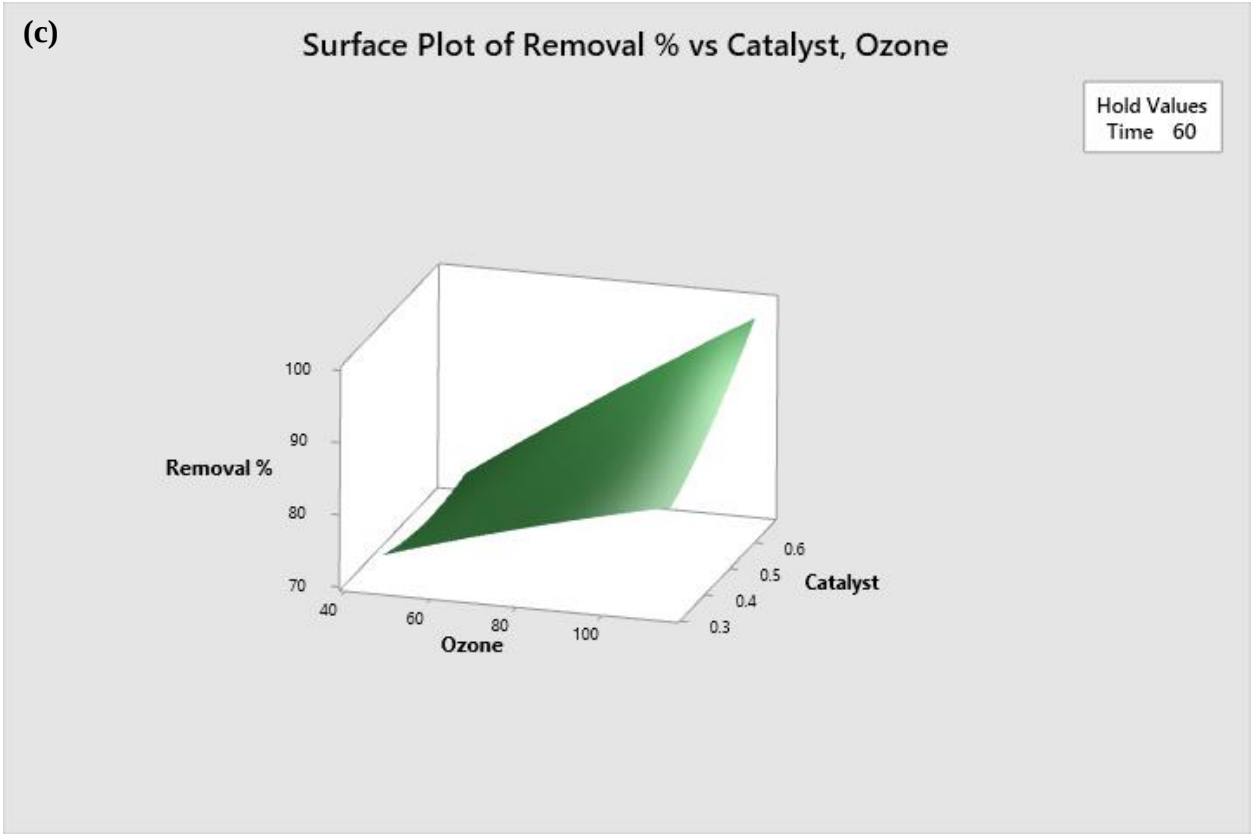
Surface Plot of Removal % vs Catalyst, Ozone
Hold Values
Time 60
Removal %
100
90
80
70
40
60
80
100
Ozone
0.3
0.4
0.5
0.6
Catalyst

(d)

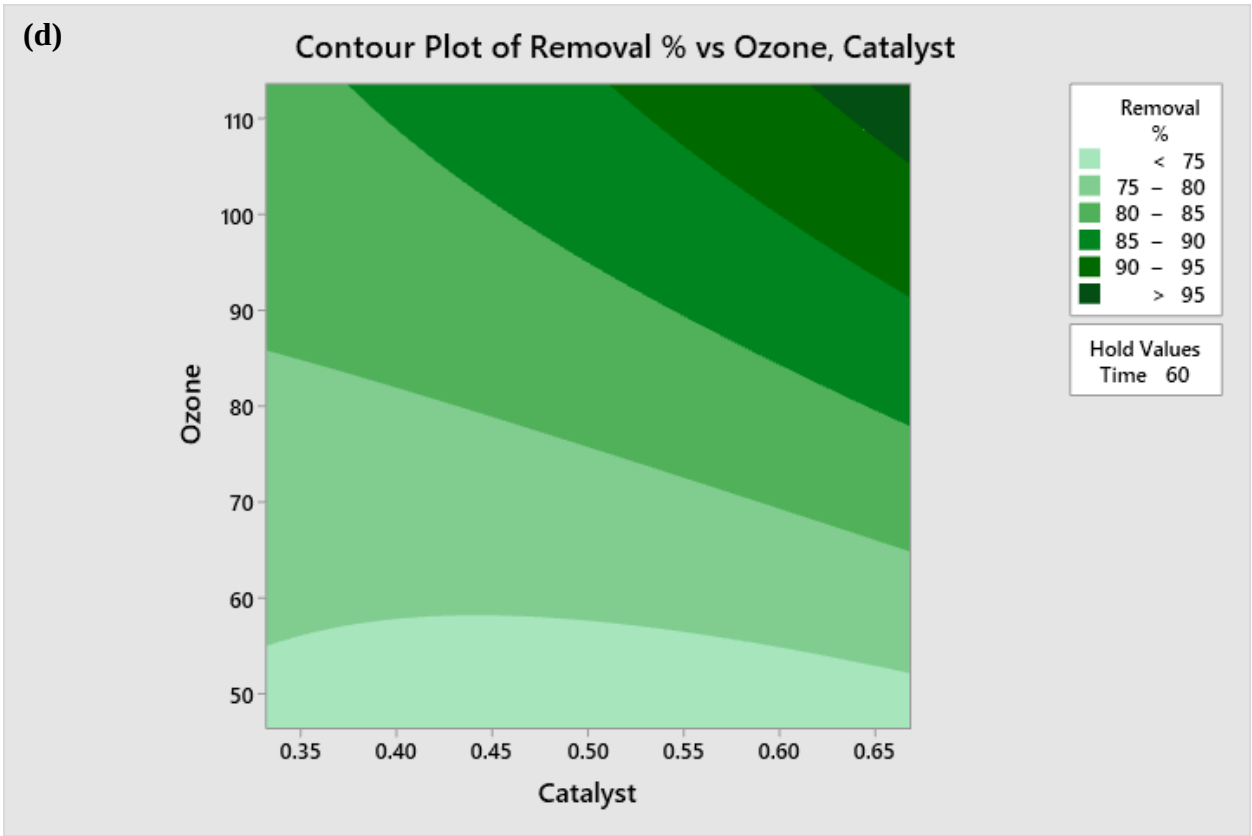
Contour Plot of Removal % vs Ozone, Catalyst
Removal %
< 75
75 – 80
80 – 85
85 – 90
90 – 95
> 95
Hold Values
Time 60
Ozone
110
100
90
80
70
60
50
0.35
0.40
0.45
0.50
0.55
0.60
0.65
Catalyst

(e)

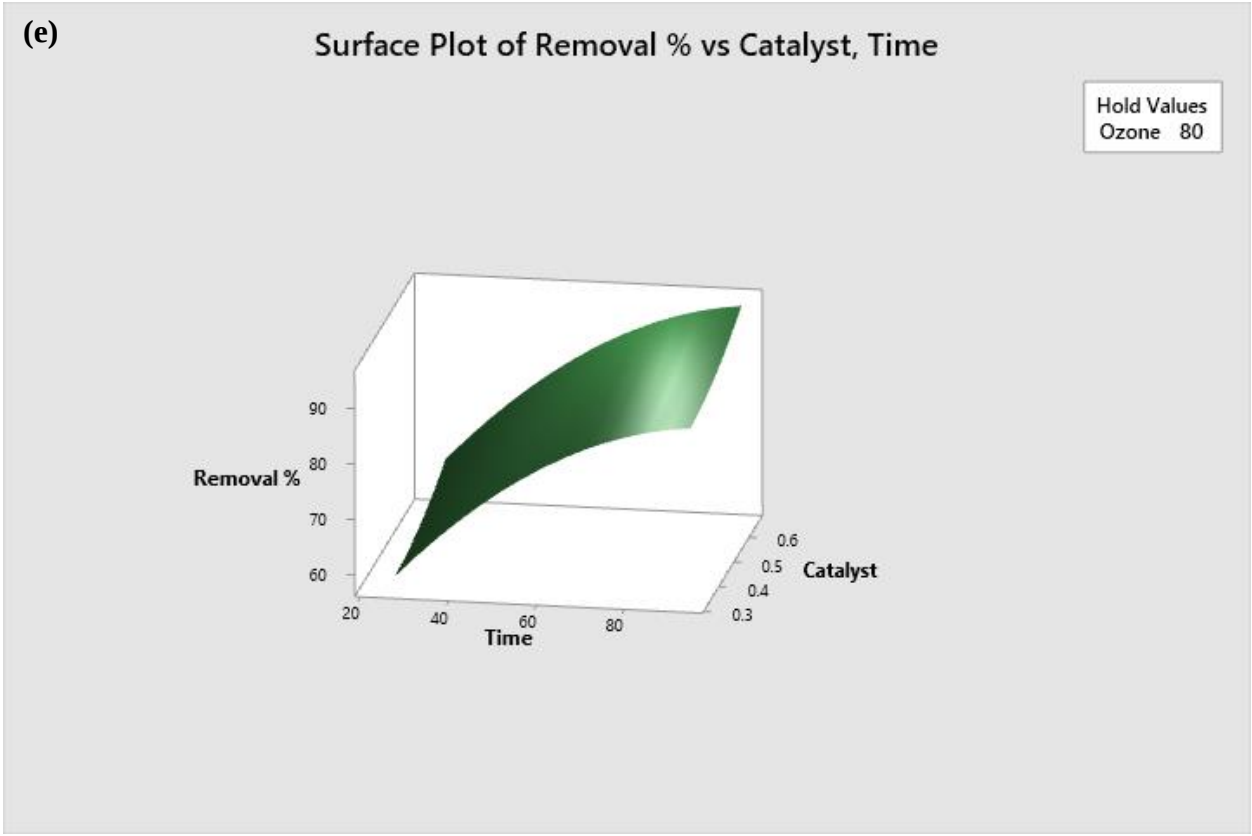
Surface Plot of Removal % vs Catalyst, Time
Hold Values
Ozone 80
Removal %
90
80
70
60
20
40
60
80
Time
0.6
0.5
0.4
0.3
Catalyst

(f)

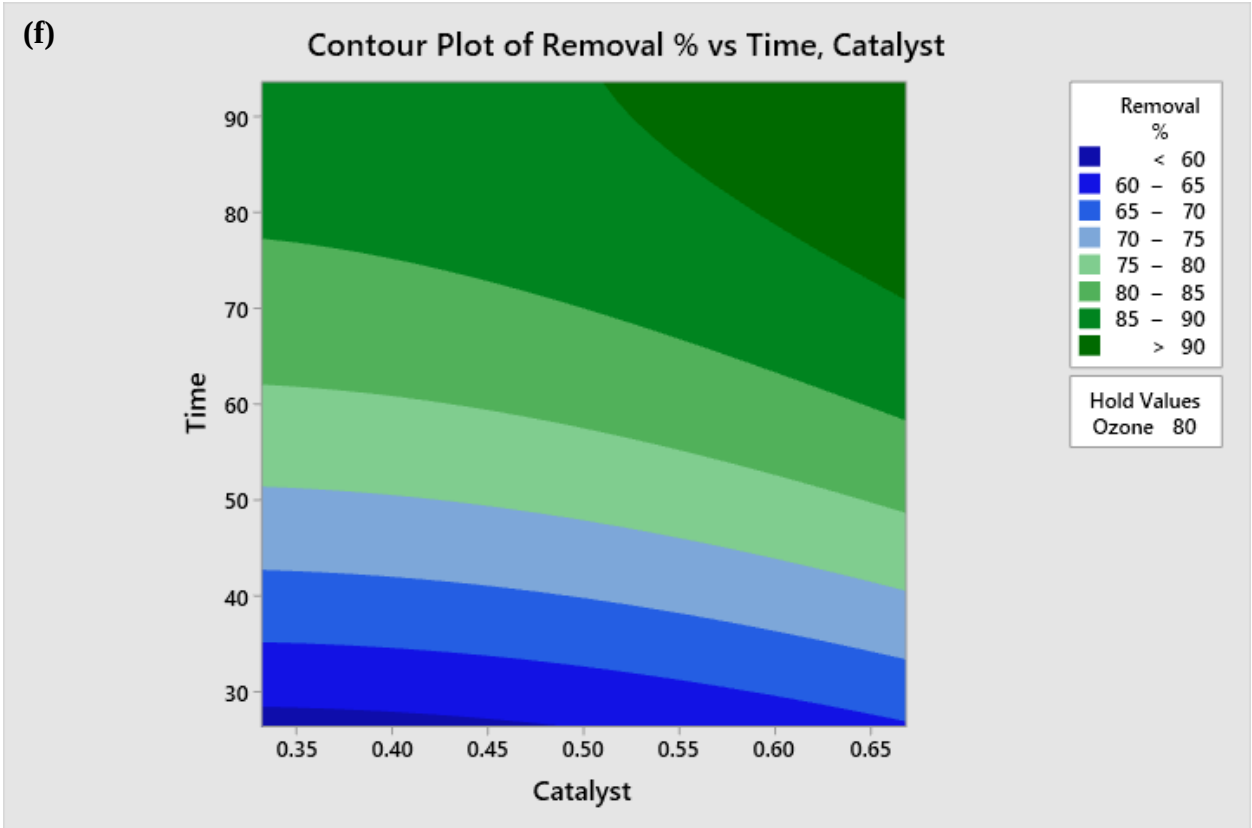
Contour Plot of Removal % vs Time, Catalyst
Time
90
80
70
60
50
40
30
0.35
0.40
0.45
0.50
0.55
0.60
0.65
Catalyst
Removal %
< 60
60 – 65
65 – 70
70 – 75
75 – 80
80 – 85
85 – 90
> 90
Hold Values
Ozone 80

Figure 3.4 Surface plot and contour plot of phenol removal across variables

3.4 Conclusion

In this chapter, a second-degree polynomial equation was applied to study the relationship between ozone, time, and catalyst for the removal of phenol in an advanced oxidation process, specifically, using GO/MgO NCs as a catalyst during ozonation. The RSM coupled with a CCD was applied to investigate the optimization of phenol removal. The optimization procedure produced high and significant R^2 (0.94) and *Adjusted-*R^2 (0.93) values for phenol removal, giving good accordance between the model and experimental data. The results also prove that RSM is a powerful tool for optimizing the operational conditions of phenol removal efficiency using the GO/MgO NCs as a catalyst in the advanced oxidation process.

CHAPTER 5

Summary and future research

This dissertation introduces a new NC material for the removal of pollutants from wastewater via an adsorption process or as a catalyst in the advanced oxidation processes. To show the capabilities of the synthesized GO/MgO NC, it was used as an adsorbent for removal of Methylene Blue and as a catalyst in advanced oxidation of phenol. Also, central composite design and surface response methodology was applied to study the optimization and modelling of phenol removal in advanced oxidation processes.

4.1 Summary of the current work

In the first part of this dissertation, a series of graphene oxide/magnesium oxide nanocomposites (GO/MgO NCs) were synthesized and applied for the removal of Methylene Blue (MB) from aqueous solutions. The prepared NCs were characterized using scanning electron microscopy, transmission electron microscopy, X-ray diffraction, Fourier transform infrared spectroscopy, X-ray photoelectron spectroscopy, and thermogravimetric analysis. The results showed that MgO particles were successfully adhered on GO. The impacts of different experimental variables on the removal of MB including GO/MgO NCs dosage, pH, contact time, and initial MB concentration were then investigated. A Langmuir isotherm model best fit the experimental analysis of adsorption isotherms. Among the three different synthesized weight ratios of GO/MgO (5:1, 1:1, and 1:5), 5:1 ratio showed the maximum adsorption capacity as 833 mg/g, which is higher than any previously reported GO-based composites. The synthesized GO/MgO NC is also observed to have higher adsorption capacity for MB removal, in comparison with pure GO and MgO. The kinetic adsorption data were best described by a pseudo-second-order kinetic

model. The pH of point of zero charge (pHpzc) of GO/MgO NCs was determined to be 9.7, 10.5, and 10.5 for ratios 5:1, 1:1, and 1:5, respectively. The results revealed that electrostatic attraction can be the dominant mechanism of adsorption between GO/MgO NCs and MB for pH values above the pHpzc; whereas for values below the pHpzc, other adsorption mechanisms, such as hydrogen bonding and π–π interactions, are likely.

In the second part of this dissertation, we investigated the mechanism and kinetics of the ozonation process in the presence of GO/MgO NCs as a catalyst for the degradation of phenol. The generation of reactive oxygen species, such as hydroxyl radicals ($^{\bullet}OH$) and singlet oxygens ($^1O_2$), was studied during catalytic ozonation using tert-Butyl alcohol and sodium azide as radical specific scavengers. The mechanism and reaction pathways of phenol degradation under catalytic ozonation were studied. Figure 4.1 illustrates the oxidation mechanisms of phenol oxidation in the catalytic advanced oxidation process using GO/MgO as a catalyst. GO/MgO NCs before and after ozonation process were characterized by FTIR and TGA-DTG. The effects of different experimental variables on the degradation of phenol including GO/MgO NCs dosage, ozone dosage, and pH were investigated. The results showed the optimum dosage of the catalyst and ozone for removal of 500 mg/L of phenol were found at 0.5 g/L and 85 mg/h, respectively. Kinetic experiments resulted in GO/MgO NCs catalyzed the decomposition of phenol at a significantly higher rate (0.0566 min^{-1}) when compared with ozonation alone (0.0151 min^{-1}).

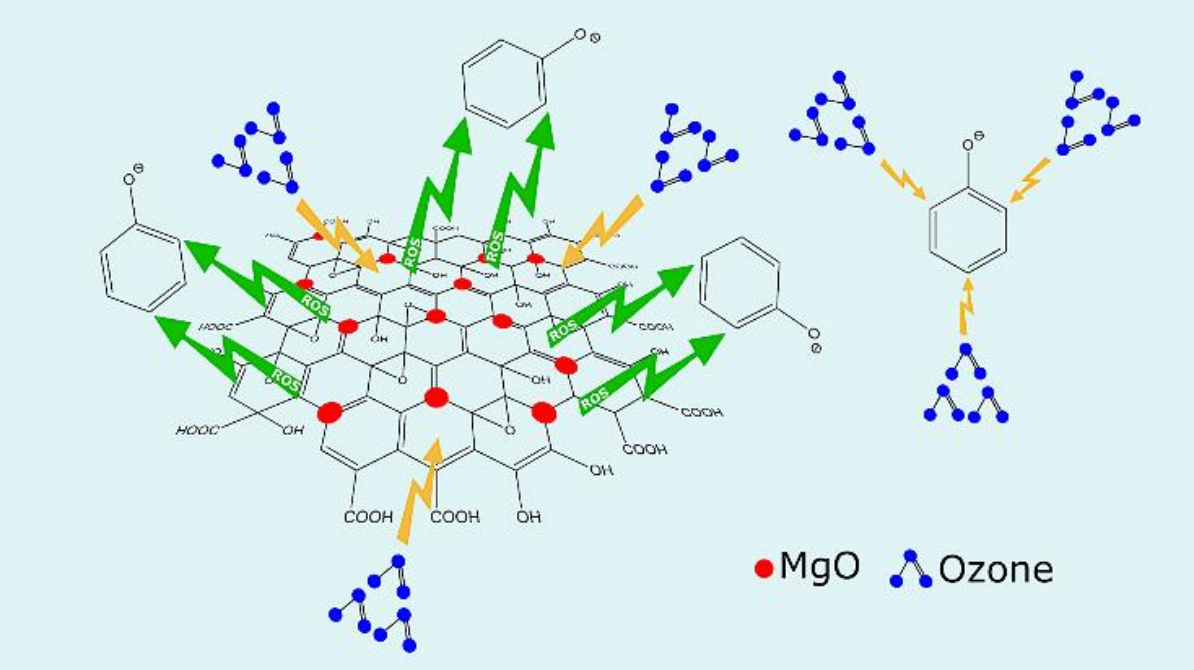

Figure 4.1 The schematic of the phenol oxidation under ozonation in the presence of GO/MgO

Finally, in the last part of this dissertation, the relationship between the parameters for the removal of phenol in catalytic advanced oxidation processes was studied. For this purpose, a second-degree polynomial equation was applied. Three design factors were selected, time, ozone dosage, and catalyst dosage using the response surface methodology coupled with CCD to study optimization of phenol removal. The results indicate that the R^2 value was more than 0.94. *Adjusted-*R^2 and *Predicted-*R^2 were found 0.093 and 0.89, respectively, showing that they are in reasonable agreement with R^2. These results confirm the existence of a good correlation between the data involved in the adopted model.

4.2 Future work

One of the outstanding questions regarding the application of the new material in the treatment of water and wastewater is if the new material is economical to produce and use for the

removal of pollutants from water and wastewater. The new technique addresses the long-standing challenge of an efficient process for large-scale production of graphene and paves the way for sustainable synthesis of the material. Recently, researchers have introduced cheap methods such as using dishwashing liquid and blender [127] or a water-phase non-dispersion exfoliation method to synthesise graphene [128] to decrease the cost of production. Therefore, we suggest studying the cost of graphene and magnesium oxide and comparison of the cost of the new synthesized NCs with other adsorbents such as activated carbon and titanium oxide. Also, we suggest a study of the removal of emerging contaminants like pharmaceutical and personal care products pollutants from wastewater in an activated sludge process. These pollutants enter the environment mainly via regular domestic use. They are potential problems for human health and should be removed before they enter the environment. They would provide an excellent follow-up to the studies here to test the breadth of application.

BIBLIOGRAPHY

[1] J.N. Tiwari, K. Mahesh, N.H. Le, K.C. Kemp, R. Timilsina, R.N. Tiwari, K.S. Kim, Reduced graphene oxide-based hydrogels for the efficient capture of dye pollutants from aqueous solutions, Carbon. 56 (2013) 173–182. doi:10.1016/j.carbon.2013.01.001.

[2] M. Hamadanian, V. Jabbari, M. Shamshiri, M. Asad, I. Mutlay, Preparation of novel hetero-nanostructures and high efficient visible light-active photocatalyst using incorporation of CNT as an electron-transfer channel into the support TiO2 and PbS, Journal of the Taiwan Institute of Chemical Engineers. 44 (2013) 748–757. doi:10.1016/j.jtice.2013.01.018.

[3] M. Hamadanian, A. Akbari, V. Jabbari, Electrospun titanium dioxide nanofibers: Fabrication, properties and its application in photo-oxidative degradation of methyl orange (MO), Fibers Polym. 12 (2011) 880–885. doi:10.1007/s12221-011-0880-z.

[4] T. Robinson, G. McMullan, R. Marchant, P. Nigam, Remediation of dyes in textile effluent: a critical review on current treatment technologies with a proposed alternative, Bioresource Technology. 77 (2001) 247–255. doi:10.1016/S0960-8524(00)00080-8.

[5] F.P. van der Zee, S. Villaverde, Combined anaerobic–aerobic treatment of azo dyes—A short review of bioreactor studies, Water Research. 39 (2005) 1425–1440. doi:10.1016/j.watres.2005.03.007.

[6] Mohd. Rafatullah, O. Sulaiman, R. Hashim, A. Ahmad, Adsorption of methylene blue on low-cost adsorbents: A review, Journal of Hazardous Materials. 177 (2010) 70–80. doi:10.1016/j.jhazmat.2009.12.047.

[7] X. Qu, J. Brame, Q. Li, P.J.J. Alvarez, Nanotechnology for a Safe and Sustainable Water Supply: Enabling Integrated Water Treatment and Reuse, Acc. Chem. Res. 46 (2013) 834–843. doi:10.1021/ar300029v.

[8] A. Tayyebi, M. Outokesh, S. Moradi, A. Doram, Synthesis and characterization of ultrasound assisted “graphene oxide–magnetite” hybrid, and investigation of its adsorption properties for Sr(II) and Co(II) ions, Applied Surface Science. 353 (2015) 350–362. doi:10.1016/j.apsusc.2015.06.087.

[9] S. Wang, H. Sun, H.M. Ang, M.O. Tadé, Adsorptive remediation of environmental pollutants using novel graphene-based nanomaterials, Chemical Engineering Journal. 226 (2013) 336–347. doi:10.1016/j.cej.2013.04.070.

[10] G. Moussavi, M. Mahmoudi, Removal of azo and anthraquinone reactive dyes from industrial wastewaters using MgO nanoparticles, Journal of Hazardous Materials. 168 (2009) 806–812. doi:10.1016/j.jhazmat.2009.02.097.

[11] G. Moussavi, M. Mahmoudi, Degradation and biodegradability improvement of the reactive red 198 azo dye using catalytic ozonation with MgO nanocrystals, Chemical Engineering Journal. 152 (2009) 1–7. doi:10.1016/j.cej.2009.03.014.

[12] M.J. Allen, V.C. Tung, R.B. Kaner, Honeycomb Carbon: A Review of Graphene, Chem. Rev. 110 (2010) 132–145. doi:10.1021/cr900070d.

[13] O.G. Apul, Q. Wang, Y. Zhou, T. Karanfil, Adsorption of aromatic organic contaminants by graphene nanosheets: Comparison with carbon nanotubes and activated carbon, Water Research. 47 (2013) 1648–1654. doi:10.1016/j.watres.2012.12.031.

[14] P. Sharma, B.K. Saikia, M.R. Das, Removal of methyl green dye molecule from aqueous system using reduced graphene oxide as an efficient adsorbent: Kinetics, isotherm and

thermodynamic parameters, Colloids and Surfaces A: Physicochemical and Engineering Aspects. 457 (2014) 125–133. doi:10.1016/j.colsurfa.2014.05.054.

[15] A. Tayyebi, M.M. Tavakoli, M. Outokesh, A. Shafiekhani, A. (Arash) Simchi, Supercritical Synthesis and Characterization of Graphene–PbS Quantum Dots Composite with Enhanced Photovoltaic Properties, Ind. Eng. Chem. Res. 54 (2015) 7382–7392. doi:10.1021/acs.iecr.5b00008.

[16] C. Wang, C. Feng, Y. Gao, X. Ma, Q. Wu, Z. Wang, Preparation of a graphene-based magnetic nanocomposite for the removal of an organic dye from aqueous solution, Chemical Engineering Journal. 173 (2011) 92–97. doi:10.1016/j.cej.2011.07.041.

[17] G. Jiang, Z. Lin, C. Chen, L. Zhu, Q. Chang, N. Wang, W. Wei, H. Tang, TiO2 nanoparticles assembled on graphene oxide nanosheets with high photocatalytic activity for removal of pollutants, Carbon. 49 (2011) 2693–2701. doi:10.1016/j.carbon.2011.02.059.

[18] J.D. Roy-Mayhew, D.J. Bozym, C. Punckt, I.A. Aksay, Functionalized Graphene as a Catalytic Counter Electrode in Dye-Sensitized Solar Cells, ACS Nano. 4 (2010) 6203–6211. doi:10.1021/nn1016428.

[19] F. Schwierz, Graphene transistors, Nature Nanotechnology. 5 (2010) 487–496. doi:10.1038/nnano.2010.89.

[20] Z. Yang, H. Yan, H. Yang, H. Li, A. Li, R. Cheng, Flocculation performance and mechanism of graphene oxide for removal of various contaminants from water, Water Research. 47 (2013) 3037–3046. doi:10.1016/j.watres.2013.03.027.

[21] G. Moussavi, Z. Hossaini, M. Pourakbar, High-rate adsorption of acetaminophen from the contaminated water onto double-oxidized graphene oxide, Chemical Engineering Journal. 287 (2016) 665–673. doi:10.1016/j.cej.2015.11.025.

[22] J.-H. Deng, X.-R. Zhang, G.-M. Zeng, J.-L. Gong, Q.-Y. Niu, J. Liang, Simultaneous removal of Cd(II) and ionic dyes from aqueous solution using magnetic graphene oxide nanocomposite as an adsorbent, Chemical Engineering Journal. 226 (2013) 189–200. doi:10.1016/j.cej.2013.04.045.

[23] G. Moussavi, A. Yazdanbakhsh, M. Heidarizad, The removal of formaldehyde from concentrated synthetic wastewater using O3/MgO/H2O2 process integrated with the biological treatment, Journal of Hazardous Materials. 171 (2009) 907–913. doi:10.1016/j.jhazmat.2009.06.090.

[24] J. Wu, L. Ma, Y. Chen, Y. Cheng, Y. Liu, X. Zha, Catalytic ozonation of organic pollutants from bio-treated dyeing and finishing wastewater using recycled waste iron shavings as a catalyst: Removal and pathways, Water Research. 92 (2016) 140–148. doi:10.1016/j.watres.2016.01.053.

[25] H. Zhang, F. Ji, Y. Zhang, Z. Pan, B. Lai, Catalytic ozonation of N,N-dimethylacetamide (DMAC) in aqueous solution using nanoscaled magnetic CuFe2O4, Separation and Purification Technology. 193 (2018) 368–377. doi:10.1016/j.seppur.2017.10.028.

[26] R.P. Rocha, A.G. Gonçalves, L.M. Pastrana-Martínez, B.C. Bordoni, O.S.G.P. Soares, J.J.M. Órfão, J.L. Faria, J.L. Figueiredo, A.M.T. Silva, M.F.R. Pereira, Nitrogen-doped graphene-based materials for advanced oxidation processes, Catalysis Today. 249 (2015) 192–198. doi:10.1016/j.cattod.2014.10.046.

[27] G. Li, Y. Lu, C. Lu, M. Zhu, C. Zhai, Y. Du, P. Yang, Efficient catalytic ozonation of bisphenol-A over reduced graphene oxide modified sea urchin-like α-MnO2 architectures, Journal of Hazardous Materials. 294 (2015) 201–208. doi:10.1016/j.jhazmat.2015.03.045.

[28] S. Li, Y. Tang, W. Chen, Z. Hu, X. Li, L. Li, Heterogeneous catalytic ozonation of clofibric acid using Ce/MCM-48: Preparation, reaction mechanism, comparison with Ce/MCM-41, Journal of Colloid and Interface Science. 504 (2017) 238–246. doi:10.1016/j.jcis.2017.05.042.

[29] Y. Huang, C. Cui, D. Zhang, L. Li, D. Pan, Heterogeneous catalytic ozonation of dibutyl phthalate in aqueous solution in the presence of iron-loaded activated carbon, Chemosphere. 119 (2015) 295–301. doi:10.1016/j.chemosphere.2014.06.060.

[30] Y. Zhang, P. Zhao, J. Li, D. Hou, J. Wang, H. Liu, A hybrid process combining homogeneous catalytic ozonation and membrane distillation for wastewater treatment, Chemosphere. 160 (2016) 134–140. doi:10.1016/j.chemosphere.2016.06.070.

[31] M. Hammad Khan, J.Y. Jung, Ozonation catalyzed by homogeneous and heterogeneous catalysts for degradation of DEHP in aqueous phase, Chemosphere. 72 (2008) 690–696. doi:10.1016/j.chemosphere.2008.02.037.

[32] Y. Wang, Y. Xie, H. Sun, J. Xiao, H. Cao, S. Wang, Efficient Catalytic Ozonation over Reduced Graphene Oxide for p-Hydroxylbenzoic Acid (PHBA) Destruction: Active Site and Mechanism, ACS Appl. Mater. Interfaces. 8 (2016) 9710–9720. doi:10.1021/acsami.6b01175.

[33] G. Moussavi, A. Alahabadi, K. Yaghmaeian, Investigating the potential of carbon activated with NH4Cl for catalyzing the degradation and mineralization of antibiotics in ozonation process, Chemical Engineering Research and Design. 97 (2015) 91–99. doi:10.1016/j.cherd.2015.03.011.

[34] K. Yaghmaeian, G. Moussavi, A. Alahabadi, Removal of amoxicillin from contaminated water using NH4Cl-activated carbon: Continuous flow fixed-bed adsorption and catalytic

ozonation regeneration, Chemical Engineering Journal. 236 (2014) 538–544. doi:10.1016/j.cej.2013.08.118.

[35] S. Song, Z. Liu, Z. He, A. Zhang, J. Chen, Y. Yang, X. Xu, Impacts of Morphology and Crystallite Phases of Titanium Oxide on the Catalytic Ozonation of Phenol, Environ. Sci. Technol. 44 (2010) 3913–3918. doi:10.1021/es100456n.

[36] T. Zhang, W. Li, J.-P. Croué, Catalytic Ozonation of Oxalate with a Cerium Supported Palladium Oxide: An Efficient Degradation Not Relying on Hydroxyl Radical Oxidation, (2011). doi:10.1021/es202209j.

[37] M. Heidarizad, S.S. Şengör, Synthesis of graphene oxide/magnesium oxide nanocomposites with high-rate adsorption of methylene blue, Journal of Molecular Liquids. 224, Part A (2016) 607–617. doi:10.1016/j.molliq.2016.09.049.

[38] M. Hamadanian, V. Jabbari, M. Shamshiri, M. Asad, I. Mutlay, Preparation of novel hetero-nanostructures and high efficient visible light-active photocatalyst using incorporation of CNT as an electron-transfer channel into the support TiO2 and PbS, Journal of the Taiwan Institute of Chemical Engineers. 44 (2013) 748–757. doi:10.1016/j.jtice.2013.01.018.

[39] M. Hamadanian, A. Akbari, V. Jabbari, Electrospun titanium dioxide nanofibers: Fabrication, properties and its application in photo-oxidative degradation of methyl orange (MO), Fibers Polym. 12 (2011) 880. doi:10.1007/s12221-011-0880-z.

[40] T. Robinson, G. McMullan, R. Marchant, P. Nigam, Remediation of dyes in textile effluent: a critical review on current treatment technologies with a proposed alternative, Bioresource Technology. 77 (2001) 247–255. doi:10.1016/S0960-8524(00)00080-8.

[41] F.P. van der Zee, S. Villaverde, Combined anaerobic–aerobic treatment of azo dyes—A short review of bioreactor studies, Water Research. 39 (2005) 1425–1440. doi:10.1016/j.watres.2005.03.007.

[42] Mohd. Rafatullah, O. Sulaiman, R. Hashim, A. Ahmad, Adsorption of methylene blue on low-cost adsorbents: A review, Journal of Hazardous Materials. 177 (2010) 70–80. doi:10.1016/j.jhazmat.2009.12.047.

[43] I.V. Mishakov, A.F. Bedilo, R.M. Richards, V.V. Chesnokov, A.M. Volodin, V.I. Zaikovskii, R.A. Buyanov, K.J. Klabunde, Nanocrystalline MgO as a Dehydrohalogenation Catalyst, Journal of Catalysis. 206 (2002) 40–48. doi:10.1006/jcat.2001.3474.

[44] L.-X. Li, D. Xu, X.-Q. Li, W.-C. Liu, Y. Jia, Excellent fluoride removal properties of porous hollow MgO microspheres, New Journal of Chemistry. 38 (2014) 5445–5452. doi:10.1039/C4NJ01361A.

[45] G. Moussavi, A. khavanin, R. Alizadeh, The integration of ozonation catalyzed with MgO nanocrystals and the biodegradation for the removal of phenol from saline wastewater, Applied Catalysis B: Environmental. 97 (2010) 160–167. doi:10.1016/j.apcatb.2010.03.036.

[46] M.M. Tavakoli, A. Tayyebi, A. Simchi, H. Aashuri, M. Outokesh, Z. Fan, Physicochemical properties of hybrid graphene–lead sulfide quantum dots prepared by supercritical ethanol, J Nanopart Res. 17 (2015) 9. doi:10.1007/s11051-014-2854-8.

[47] A. Kumar, J. Kumar, On the synthesis and optical absorption studies of nano-size magnesium oxide powder, Journal of Physics and Chemistry of Solids. 69 (2008) 2764–2772. doi:10.1016/j.jpcs.2008.06.143.

[48] W.E. Federation, A.P.H. Association, Standard methods for the examination of water and wastewater, American Public Health Association (APHA): Washington, DC, USA. (2005).

[49] H.A. Becerril, J. Mao, Z. Liu, R.M. Stoltenberg, Z. Bao, Y. Chen, Evaluation of Solution-Processed Reduced Graphene Oxide Films as Transparent Conductors, ACS Nano. 2 (2008) 463–470. doi:10.1021/nn700375n.

[50] Y. Tang, H. Guo, L. Xiao, S. Yu, N. Gao, Y. Wang, Synthesis of reduced graphene oxide/magnetite composites and investigation of their adsorption performance of fluoroquinolone antibiotics, Colloids and Surfaces A: Physicochemical and Engineering Aspects. 424 (2013) 74–80. doi:10.1016/j.colsurfa.2013.02.030.

[51] L. Fan, C. Luo, X. Li, F. Lu, H. Qiu, M. Sun, Fabrication of novel magnetic chitosan grafted with graphene oxide to enhance adsorption properties for methyl blue, Journal of Hazardous Materials. 215–216 (2012) 272–279. doi:10.1016/j.jhazmat.2012.02.068.

[52] J. Ma, Z. Zhang, M. Yang, Y. Wu, X. Feng, L. Liu, X. Zhang, Z. Tong, Intercalated methylene blue between calcium niobate nanosheets by ESD technique for electrocatalytic oxidation of ascorbic acid, Microporous and Mesoporous Materials. 221 (2016) 123–127. doi:10.1016/j.micromeso.2015.09.030.

[53] V. Jabbari, J.M. Veleta, M. Zarei-Chaleshtori, J. Gardea-Torresdey, D. Villagrán, Green synthesis of magnetic MOF@GO and MOF@CNT hybrid nanocomposites with high adsorption capacity towards organic pollutants, Chemical Engineering Journal. 304 (2016) 774–783. doi:10.1016/j.cej.2016.06.034.

[54] H. Pang, G. Ning, W. Gong, J. Ye, Y. Lin, Direct synthesis of hexagonal Mg(OH)2 nanoplates from natural brucite without dissolution procedure, Chem. Commun. 47 (2011) 6317–6319. doi:10.1039/C1CC10279F.

[55] M. Wojtoniszak, B. Zielinska, R.J. Kalenczuk, E. Mijowska, Photocatalytic performance of titania nanospheres deposited on graphene in coumarin oxidation reaction, Mater Sci-Pol. 30 (2012) 32–38. doi:10.2478/s13536-012-0008-1.

[56] M. Khan, A.H. Al-Marri, M. Khan, N. Mohri, S.F. Adil, A. Al-Warthan, M.R.H. Siddiqui, H.Z. Alkhathlan, R. Berger, W. Tremel, M.N. Tahir, Pulicaria glutinosa plant extract: a green and eco-friendly reducing agent for the preparation of highly reduced graphene oxide, RSC Adv. 4 (2014) 24119–24125. doi:10.1039/C4RA01296H.

[57] A. Tayyebi, M. outokesh, M. Tayebi, A. Shafikhani, S.S. Şengör, ZnO quantum dots-graphene composites: Formation mechanism and enhanced photocatalytic activity for degradation of methyl orange dye, Journal of Alloys and Compounds. 663 (2016) 738–749. doi:10.1016/j.jallcom.2015.12.169.

[58] Y. Wu, H. Luo, H. Wang, C. Wang, J. Zhang, Z. Zhang, Adsorption of hexavalent chromium from aqueous solutions by graphene modified with cetyltrimethylammonium bromide, Journal of Colloid and Interface Science. 394 (2013) 183–191. doi:10.1016/j.jcis.2012.11.049.

[59] B. Li, H. Cao, G. Yin, Mg(OH)2@reduced graphene oxide composite for removal of dyes from water, J. Mater. Chem. 21 (2011) 13765–13768. doi:10.1039/C1JM13368C.

[60] M.T. Azar, M. Leili, F. Taherkhani, A. Bhatnagar, A comparative study for the removal of aniline from aqueous solutions using modified bentonite and activated carbon, Desalination and Water Treatment. 57 (2016) 24430–24443. doi:10.1080/19443994.2016.1138890.

[61] A. Tayyebi, M. Outokesh, Supercritical synthesis of a magnetite-reduced graphene oxide hybrid with enhanced adsorption properties toward cobalt & strontium ions, RSC Adv. 6 (2016) 13898–13913. doi:10.1039/C5RA19057F.

[62] Y.S. Al-Degs, M.I. El-Barghouthi, A.H. El-Sheikh, G.M. Walker, Effect of solution pH, ionic strength, and temperature on adsorption behavior of reactive dyes on activated carbon, Dyes and Pigments. 77 (2008) 16–23. doi:10.1016/j.dyepig.2007.03.001.

[63] G. Zhao, J. Li, X. Ren, C. Chen, X. Wang, Few-Layered Graphene Oxide Nanosheets As Superior Sorbents for Heavy Metal Ion Pollution Management, Environ. Sci. Technol. 45 (2011) 10454–10462. doi:10.1021/es203439v.

[64] T. Wu, X. Cai, S. Tan, H. Li, J. Liu, W. Yang, Adsorption characteristics of acrylonitrile, p-toluenesulfonic acid, 1-naphthalenesulfonic acid and methyl blue on graphene in aqueous solutions, Chemical Engineering Journal. 173 (2011) 144–149. doi:10.1016/j.cej.2011.07.050.

[65] S.-T. Yang, S. Chen, Y. Chang, A. Cao, Y. Liu, H. Wang, Removal of methylene blue from aqueous solution by graphene oxide, Journal of Colloid and Interface Science. 359 (2011) 24–29. doi:10.1016/j.jcis.2011.02.064.

[66] G.K. Ramesha, A. Vijaya Kumara, H.B. Muralidhara, S. Sampath, Graphene and graphene oxide as effective adsorbents toward anionic and cationic dyes, Journal of Colloid and Interface Science. 361 (2011) 270–277. doi:10.1016/j.jcis.2011.05.050.

[67] L. Ai, C. Zhang, Z. Chen, Removal of methylene blue from aqueous solution by a solvothermal-synthesized graphene/magnetite composite, Journal of Hazardous Materials. 192 (2011) 1515–1524. doi:10.1016/j.jhazmat.2011.06.068.

[68] T. Liu, Y. Li, Q. Du, J. Sun, Y. Jiao, G. Yang, Z. Wang, Y. Xia, W. Zhang, K. Wang, H. Zhu, D. Wu, Adsorption of methylene blue from aqueous solution by graphene, Colloids and Surfaces B: Biointerfaces. 90 (2012) 197–203. doi:10.1016/j.colsurfb.2011.10.019.

[69] Y. Li, Q. Du, T. Liu, X. Peng, J. Wang, J. Sun, Y. Wang, S. Wu, Z. Wang, Y. Xia, L. Xia, Comparative study of methylene blue dye adsorption onto activated carbon, graphene oxide, and carbon nanotubes, Chemical Engineering Research and Design. 91 (2013) 361–368. doi:10.1016/j.cherd.2012.07.007.

[70] Y. Li, Q. Du, T. Liu, J. Sun, Y. Wang, S. Wu, Z. Wang, Y. Xia, L. Xia, Methylene blue adsorption on graphene oxide/calcium alginate composites, Carbohydrate Polymers. 95 (2013) 501–507. doi:10.1016/j.carbpol.2013.01.094.

[71] M. Toor, B. Jin, Adsorption characteristics, isotherm, kinetics, and diffusion of modified natural bentonite for removing diazo dye, Chemical Engineering Journal. 187 (2012) 79–88. doi:10.1016/j.cej.2012.01.089.

[72] A. Behnamfard, M.M. Salarirad, Equilibrium and kinetic studies on free cyanide adsorption from aqueous solution by activated carbon, Journal of Hazardous Materials. 170 (2009) 127–133. doi:10.1016/j.jhazmat.2009.04.124.

[73] Q. Bao, K.S. Hui, J.G. Duh, Promoting catalytic ozonation of phenol over graphene through nitrogenation and Co3O4 compositing, Journal of Environmental Sciences. 50 (2016) 38–48. doi:10.1016/j.jes.2016.03.029.

[74] L. Jothinathan, J. Hu, Kinetic evaluation of graphene oxide based heterogenous catalytic ozonation for the removal of ibuprofen, Water Research. 134 (2018) 63–73. doi:10.1016/j.watres.2018.01.033.

[75] A. Mashayekh-Salehi, G. Moussavi, K. Yaghmaeian, Preparation, characterization and catalytic activity of a novel mesoporous nanocrystalline MgO nanoparticle for ozonation of acetaminophen as an emerging water contaminant, Chemical Engineering Journal. 310 (2017) 157–169. doi:10.1016/j.cej.2016.10.096.

[76] H. Zhu, W. Ma, H. Han, Y. Han, W. Ma, Catalytic ozonation of quinoline using nano-MgO: Efficacy, pathways, mechanisms and its application to real biologically pretreated coal gasification wastewater, Chemical Engineering Journal. 327 (2017) 91–99. doi:10.1016/j.cej.2017.06.025.

[77] M. Heidarizad, S.S. Sengör, Graphene Oxide/Magnesium Oxide Nanocomposites as Superior Sorbents for Methylene Blue Removal from Aqueous Solutions, US20170369333A1, 2017. https://patents.google.com/patent/US20170369333/en (accessed March 7, 2018).

[78] N. Azbar, A. Bayram, A. Filibeli, A. Muezzinoglu, F. SEngul, A. Ozer, A Review of Waste Management Options in Olive Oil Production, Critical Reviews in Environmental Science and Technology. 34 (2004) 209–247. doi:10.1080/10643380490279932.

[79] G. Moussavi, M. Heidarizad, Biodegradation of mixture of phenol and formaldehyde in wastewater using a single-basin MSCR process, Journal of Biotechnology. 150 (2010) 240–245. doi:10.1016/j.jbiotec.2010.08.012.

[80] G. Moussavi, M. Heidarizad, The performance of SBR, SCR, and MSCR for simultaneous biodegradation of high concentrations of formaldehyde and ammonia, Separation and Purification Technology. 77 (2011) 187–195. doi:10.1016/j.seppur.2010.11.028.

[81] X. Qu, J. Zheng, Y. Zhang, Catalytic ozonation of phenolic wastewater with activated carbon fiber in a fluid bed reactor, Journal of Colloid and Interface Science. 309 (2007) 429–434. doi:10.1016/j.jcis.2007.01.034.

[82] Z. Wu, H. Zhong, X. Yuan, H. Wang, L. Wang, X. Chen, G. Zeng, Y. Wu, Adsorptive removal of methylene blue by rhamnolipid-functionalized graphene oxide from wastewater, Water Research. 67 (2014) 330–344. doi:10.1016/j.watres.2014.09.026.

[83] A. Tayyebi, S. Moradi, F. Azizi, M. Outokesh, K. Shadanfar, S.S. Mousavi, Fabrication of new magnetite-graphene nanocomposite and comparison of its laser-hyperthermia properties with conventionally prepared magnetite-graphene hybrid, Materials Science and Engineering: C. 75 (2017) 572–581. doi:10.1016/j.msec.2017.02.086.

[84] G. Moussavi, M. Mahmoudi, Removal of azo and anthraquinone reactive dyes from industrial wastewaters using MgO nanoparticles, Journal of Hazardous Materials. 168 (2009) 806–812. doi:10.1016/j.jhazmat.2009.02.097.

[85] B. Kasprzyk-Hordern, M. Ziółek, J. Nawrocki, Catalytic ozonation and methods of enhancing molecular ozone reactions in water treatment, Applied Catalysis B: Environmental. 46 (2003) 639–669. doi:10.1016/S0926-3373(03)00326-6.

[86] T. Nöthe, H. Fahlenkamp, C. von Sonntag, Ozonation of Wastewater: Rate of Ozone Consumption and Hydroxyl Radical Yield, Environ. Sci. Technol. 43 (2009) 5990–5995. doi:10.1021/es900825f.

[87] G.V. Buxton, C.L. Greenstock, W.P. Helman, A.B. Ross, Critical Review of rate constants for reactions of hydrated electrons, hydrogen atoms and hydroxyl radicals (·OH/·O− in Aqueous Solution, Journal of Physical and Chemical Reference Data. 17 (1988) 513–886. doi:10.1063/1.555805.

[88] A. Jawad, X. Lu, Z. Chen, G. Yin, Degradation of Chlorophenols by Supported Co–Mg–Al Layered Double Hydrotalcite with Bicarbonate Activated Hydrogen Peroxide, J. Phys. Chem. A. 118 (2014) 10028–10035. doi:10.1021/jp5085313.

[89] S.O. Baumann, J. Schneider, A. Sternig, D. Thomele, S. Stankic, T. Berger, H. Grönbeck, O. Diwald, Size Effects in MgO Cube Dissolution, Langmuir. 31 (2015) 2770–2776. doi:10.1021/la504651v.

[90] J. Hoigné, H. Bader, Rate constants of reactions of ozone with organic and inorganic compounds in water—II: Dissociating organic compounds, Water Research. 17 (1983) 185–194. doi:10.1016/0043-1354(83)90099-4.

[91] M. Lee, Prediction of transformation products during ozonation of micropollutant-containing waters, Lausanne, EPFL. (2016). doi:10.5075/epfl-thesis-7177.

[92] F. Muñoz, E. Mvula, S.E. Braslavsky, C. von Sonntag, Singlet dioxygen formation in ozone reactions in aqueous solution, J. Chem. Soc., Perkin Trans. 2. 0 (2001) 1109–1116. doi:10.1039/B101230O.

[93] F.E. Scully, J. Hoigné, Rate constants for reactions of singlet oxygen with phenols and other compounds in water, Chemosphere. 16 (1987) 681–694. doi:10.1016/0045-6535(87)90004-X.

[94] P.R. Tentscher, M. Bourgin, U. von Gunten, Ozonation of Para-Substituted Phenolic Compounds Yields p-Benzoquinones, Other Cyclic α,β-Unsaturated Ketones, and Substituted Catechols, Environ. Sci. Technol. (2018). doi:10.1021/acs.est.8b00011.

[95] K. Turhan, S. Uzman, Removal of phenol from water using ozone, Desalination. 229 (2008) 257–263. doi:10.1016/j.desal.2007.09.012.

[96] J.-N. Liu, Z. Chen, Q.-Y. Wu, A. Li, H.-Y. Hu, C. Yang, Ozone/graphene oxide catalytic oxidation: a novel method to degrade emerging organic contaminant N, N-diethyl-m-toluamide (DEET), Sci Rep. 6 (2016). doi:10.1038/srep31405.

[97] A. Tayyebi, T. Soltani, B.-K. Lee, M. Outokesh, M. Tayebi, Novel Visible Light Photocatalytic and Photoelectrochemical (PEC) Activity of Carbon-doped Zinc Oxide/Reduced Graphene Oxide: Supercritical Methanol Synthesis with Enhanced

Photocorrosion Suppression, Journal of Alloys and Compounds. 723 (2017) 1001–1010. doi:10.1016/j.jallcom.2017.06.316.

[98] Y. Yoon, H. Oh, Y.-T. Ahn, M. Kwon, Y. Jung, W.K. Park, T.-M. Hwang, W.S. Yang, J.-W. Kang, Evaluation of the O3/graphene-based materials catalytic process: pH effect and iopromide removal, Catalysis Today. 282, Part 1 (2017) 77–85. doi:10.1016/j.cattod.2016.03.014.

[99] D. Hou, Q. Liu, X. Wang, Y. Quan, Z. Qiao, L. Yu, S. Ding, Facile synthesis of graphene via reduction of graphene oxide by artemisinin in ethanol, Journal of Materiomics. (2018). doi:10.1016/j.jmat.2018.01.002.

[100] Z. Fan, K. Wang, T. Wei, J. Yan, L. Song, B. Shao, An environmentally friendly and efficient route for the reduction of graphene oxide by aluminum powder, Carbon. 48 (2010) 1686–1689. doi:10.1016/j.carbon.2009.12.063.

[101] N. Hong, Y. Pan, J. Zhan, B. Wang, K. Zhou, L. Song, Y. Hu, Fabrication of graphene/Ni–Ce mixed oxide with excellent performance for reducing fire hazard of polypropylene, RSC Adv. 3 (2013) 16440–16448. doi:10.1039/C3RA42095G.

[102] M. Cobos, B. González, M.J. Fernández, M.D. Fernández, Study on the effect of graphene and glycerol plasticizer on the properties of chitosan-graphene nanocomposites via in situ green chemical reduction of graphene oxide, International Journal of Biological Macromolecules. 114 (2018) 599–613. doi:10.1016/j.ijbiomac.2018.03.129.

[103] P. Cui, J. Lee, E. Hwang, H. Lee, One-pot reduction of graphene oxide at subzero temperatures, Chemical Communications. 47 (2011) 12370–12372. doi:10.1039/C1CC15569E.

[104] S. Dubin, S. Gilje, K. Wang, V.C. Tung, K. Cha, A.S. Hall, J. Farrar, R. Varshneya, Y. Yang, R.B. Kaner, A One-Step, Solvothermal Reduction Method for Producing Reduced Graphene Oxide Dispersions in Organic Solvents, ACS Nano. 4 (2010) 3845–3852. doi:10.1021/nn100511a.

[105] G. Moussavi, M. Mahmoudi, Degradation and biodegradability improvement of the reactive red 198 azo dye using catalytic ozonation with MgO nanocrystals, Chemical Engineering Journal. 152 (2009) 1–7. doi:10.1016/j.cej.2009.03.014.

[106] H.C. Wang, S.H. Chang, P.C. Hung, J.F. Hwang, M.B. Chang, Synergistic effect of transition metal oxides and ozone on PCDD/F destruction, Journal of Hazardous Materials. 164 (2009) 1452–1459. doi:10.1016/j.jhazmat.2008.09.093.

[107] H.M. Jalali, Kinetic study of antibiotic ciprofloxacin ozonation by MWCNT/MnO2 using Monte Carlo simulation, Materials Science and Engineering: C. 59 (2016) 924–929. doi:10.1016/j.msec.2015.10.085.

[108] L. Filho, F. A, Ozone application in water sources: effects of operational parameters and water quality variables on ozone residual profiles and decay rates, Brazilian Journal of Chemical Engineering. 27 (2010) 545–554. doi:10.1590/S0104-66322010000400006.

[109] L. Xing, Y. Xie, H. Cao, D. Minakata, Y. Zhang, J.C. Crittenden, Activated carbon-enhanced ozonation of oxalate attributed to HO oxidation in bulk solution and surface oxidation: Effects of the type and number of basic sites, Chemical Engineering Journal. 245 (2014) 71–79. doi:10.1016/j.cej.2014.01.104.

[110] X. Zhai, Z. Chen, S. Zhao, H. Wang, L. Yang, Enhanced ozonation of dichloroacetic acid in aqueous solution using nanometer ZnO powders, Journal of Environmental Sciences. 22 (2010) 1527–1533. doi:10.1016/S1001-0742(09)60284-9.

[111] L.F. Liotta, M. Gruttadauria, G. Di Carlo, G. Perrini, V. Librando, Heterogeneous catalytic degradation of phenolic substrates: Catalysts activity, Journal of Hazardous Materials. 162 (2009) 588–606. doi:10.1016/j.jhazmat.2008.05.115.

[112] L. Yuan, J. Shen, Z. Chen, X. Guan, Role of Fe/pumice composition and structure in promoting ozonation reactions, Applied Catalysis B: Environmental. 180 (2016) 707–714. doi:10.1016/j.apcatb.2015.07.016.

[113] M. Ahmadi, B. Kakavandi, N. Jaafarzadeh, A. Akbar Babaei, Catalytic ozonation of high saline petrochemical wastewater using PAC@FeIIFe2IIIO4: Optimization, mechanisms and biodegradability studies, Separation and Purification Technology. 177 (2017) 293–303. doi:10.1016/j.seppur.2017.01.008.

[114] A.M. Ghaedi, M. Ghaedi, A. Vafaei, N. Iravani, M. Keshavarz, M. Rad, I. Tyagi, S. Agarwal, V.K. Gupta, Adsorption of copper (II) using modified activated carbon prepared from Pomegranate wood: Optimization by bee algorithm and response surface methodology, Journal of Molecular Liquids. 206 (2015) 195–206. doi:10.1016/j.molliq.2015.02.029.

[115] Z.R. Lazic, Design of Experiments in Chemical Engineering: A Practical Guide, John Wiley & Sons, 2006.

[116] T.K. Dora, Y.K. Mohanty, G.K. Roy, B. Sarangi, Adsorption studies of As(III) from wastewater with a novel adsorbent in a three-phase fluidized bed by using response surface method, Journal of Environmental Chemical Engineering. 1 (2013) 150–158. doi:10.1016/j.jece.2013.04.011.

[117] L. St»hle, S. Wold, Analysis of variance (ANOVA), Chemometrics and Intelligent Laboratory Systems. 6 (1989) 259–272. doi:10.1016/0169-7439(89)80095-4.

[118] M. Dastkhoon, M. Ghaedi, A. Asfaram, A. Goudarzi, S.M. Langroodi, I. Tyagi, S. Agarwal, V.K. Gupta, Ultrasound assisted adsorption of malachite green dye onto ZnS:Cu-NP-AC: Equilibrium isotherms and kinetic studies – Response surface optimization, Separation and Purification Technology. 156 (2015) 780–788. doi:10.1016/j.seppur.2015.11.001.

[119] M. Zbair, Z. Anfar, H. Ait Ahsaine, N. El Alem, M. Ezahri, Acridine orange adsorption by zinc oxide/almond shell activated carbon composite: Operational factors, mechanism and performance optimization using central composite design and surface modeling, Journal of Environmental Management. 206 (2018) 383–397. doi:10.1016/j.jenvman.2017.10.058.

[120] Minitab® Statistical Software, Minitab, LLC, 2018.

[121] A. Asfaram, M. Ghaedi, A. Goudarzi, M. Rajabi, Response surface methodology approach for optimization of simultaneous dye and metal ion ultrasound-assisted adsorption onto Mn doped Fe 3 O 4 -NPs loaded on AC: kinetic and isothermal studies, Dalton Transactions. 44 (2015) 14707–14723. doi:10.1039/C5DT01504A.

[122] M.Y. Noordin, V.C. Venkatesh, S. Sharif, S. Elting, A. Abdullah, Application of response surface methodology in describing the performance of coated carbide tools when turning AISI 1045 steel, Journal of Materials Processing Technology. 145 (2004) 46–58. doi:10.1016/S0924-0136(03)00861-6.

[123] T. Arshad, S.A. Khan, M. Faisal, Z. Shah, K. Akhtar, A.M. Asiri, A.A. Ismail, B.G. Alhogbi, S.B. Khan, Cerium based photocatalysts for the degradation of acridine orange in visible light, Journal of Molecular Liquids. 241 (2017) 20–26. doi:10.1016/j.molliq.2017.05.079.

[124] P. Sudamalla, P. Saravanan, M. Matheswaran, Optimization of operating parameters using response surface methodology for adsorption of crystal violet by activated carbon prepared from mango kernel, Environ. Res. 22 (2012) 1–7.

[125] A. Hannachi, S. Hammami, N. Raouafi, H. Maghraoui-Meherzi, Preparation of manganese sulfide (MnS) thin films by chemical bath deposition: Application of the experimental design methodology, Journal of Alloys and Compounds. 663 (2016) 507–515. doi:10.1016/j.jallcom.2015.11.058.

[126] K.P. Singh, A.K. Singh, S. Gupta, S. Sinha, Optimization of Cr(VI) reduction by zero-valent bimetallic nanoparticles using the response surface modeling approach, Desalination. 270 (2011) 275–284. doi:10.1016/j.desal.2010.11.056.

[127] K.R. Paton, E. Varrla, C. Backes, R.J. Smith, U. Khan, A. O'Neill, C. Boland, M. Lotya, O.M. Istrate, P. King, Scalable production of large quantities of defect-free few-layer graphene by shear exfoliation in liquids, Nature Materials. 13 (2014) 624.

[128] L. Dong, Z. Chen, X. Zhao, J. Ma, S. Lin, M. Li, Y. Bao, L. Chu, K. Leng, H. Lu, K.P. Loh, A non-dispersion strategy for large-scale production of ultra-high concentration graphene slurries in water, Nature Communications. 9 (2018) 76. doi:10.1038/s41467-017-02580-3.

Appendix

Appendix A. *F*-distribution table

Upper 5% points

ν_2 \ ν_1	1	2	3	4	5	6	7	8	9	10	12	15	20	24	30	40	60	120	∞
1	161·4	199·5	215·7	224·6	230·2	234·0	236·8	238·9	240·5	241·9	243·9	245·9	248·0	249·1	250·1	251·1	252·2	253·3	254·3
2	18·51	19·00	19·16	19·25	19·30	19·33	19·35	19·37	19·38	19·40	19·41	19·43	19·45	19·45	19·46	19·47	19·48	19·49	19·50
3	10·13	9·55	9·28	9·12	9·01	8·94	8·89	8·85	8·81	8·79	8·74	8·70	8·66	8·64	8·62	8·59	8·57	8·55	8·53
4	7·71	6·94	6·59	6·39	6·26	6·16	6·09	6·04	6·00	5·96	5·91	5·86	5·80	5·77	5·75	5·72	5·69	5·66	5·63
5	6·61	5·79	5·41	5·19	5·05	4·95	4·88	4·82	4·77	4·74	4·68	4·62	4·56	4·53	4·50	4·46	4·43	4·40	4·36
6	5·99	5·14	4·76	4·53	4·39	4·28	4·21	4·15	4·10	4·06	4·00	3·94	3·87	3·84	3·81	3·77	3·74	3·70	3·67
7	5·59	4·74	4·35	4·12	3·97	3·87	3·79	3·73	3·68	3·64	3·57	3·51	3·44	3·41	3·38	3·34	3·30	3·27	3·23
8	5·32	4·46	4·07	3·84	3·69	3·58	3·50	3·44	3·39	3·35	3·28	3·22	3·15	3·12	3·08	3·04	3·01	2·97	2·93
9	5·12	4·26	3·86	3·63	3·48	3·37	3·29	3·23	3·18	3·14	3·07	3·01	2·94	2·90	2·86	2·83	2·79	2·75	2·71
10	4·96	4·10	3·71	3·48	3·33	3·22	3·14	3·07	3·02	2·98	2·91	2·85	2·77	2·74	2·70	2·66	2·62	2·58	2·54
11	4·84	3·98	3·59	3·36	3·20	3·09	3·01	2·95	2·90	2·85	2·79	2·72	2·65	2·61	2·57	2·53	2·49	2·45	2·40
12	4·75	3·89	3·49	3·26	3·11	3·00	2·91	2·85	2·80	2·75	2·69	2·62	2·54	2·51	2·47	2·43	2·38	2·34	2·30
13	4·67	3·81	3·41	3·18	3·03	2·92	2·83	2·77	2·71	2·67	2·60	2·53	2·46	2·42	2·38	2·34	2·30	2·25	2·21
14	4·60	3·74	3·34	3·11	2·96	2·85	2·76	2·70	2·65	2·60	2·53	2·46	2·39	2·35	2·31	2·27	2·22	2·18	2·13
15	4·54	3·68	3·29	3·06	2·90	2·79	2·71	2·64	2·59	2·54	2·48	2·40	2·33	2·29	2·25	2·20	2·16	2·11	2·07
16	4·49	3·63	3·24	3·01	2·85	2·74	2·66	2·59	2·54	2·49	2·42	2·35	2·28	2·24	2·19	2·15	2·11	2·06	2·01
17	4·45	3·59	3·20	2·96	2·81	2·70	2·61	2·55	2·49	2·45	2·38	2·31	2·23	2·19	2·15	2·10	2·06	2·01	1·96
18	4·41	3·55	3·16	2·93	2·77	2·66	2·58	2·51	2·46	2·41	2·34	2·27	2·19	2·15	2·11	2·06	2·02	1·97	1·92
19	4·38	3·52	3·13	2·90	2·74	2·63	2·54	2·48	2·42	2·38	2·31	2·23	2·16	2·11	2·07	2·03	1·98	1·93	1·88
20	4·35	3·49	3·10	2·87	2·71	2·60	2·51	2·45	2·39	2·35	2·28	2·20	2·12	2·08	2·04	1·99	1·95	1·90	1·84
21	4·32	3·47	3·07	2·84	2·68	2·57	2·49	2·42	2·37	2·32	2·25	2·18	2·10	2·05	2·01	1·96	1·92	1·87	1·81
22	4·30	3·44	3·05	2·82	2·66	2·55	2·46	2·40	2·34	2·30	2·23	2·15	2·07	2·03	1·98	1·94	1·89	1·84	1·78
23	4·28	3·42	3·03	2·80	2·64	2·53	2·44	2·37	2·32	2·27	2·20	2·13	2·05	2·01	1·96	1·91	1·86	1·81	1·76
24	4·26	3·40	3·01	2·78	2·62	2·51	2·42	2·36	2·30	2·25	2·18	2·11	2·03	1·98	1·94	1·89	1·84	1·79	1·73
25	4·24	3·39	2·99	2·76	2·60	2·49	2·40	2·34	2·28	2·24	2·16	2·09	2·01	1·96	1·92	1·87	1·82	1·77	1·71
26	4·23	3·37	2·98	2·74	2·59	2·47	2·39	2·32	2·27	2·22	2·15	2·07	1·99	1·95	1·90	1·85	1·80	1·75	1·69
27	4·21	3·35	2·96	2·73	2·57	2·46	2·37	2·31	2·25	2·20	2·13	2·06	1·97	1·93	1·88	1·84	1·79	1·73	1·67
28	4·20	3·34	2·95	2·71	2·56	2·45	2·36	2·29	2·24	2·19	2·12	2·04	1·96	1·91	1·87	1·82	1·77	1·71	1·65
29	4·18	3·33	2·93	2·70	2·55	2·43	2·35	2·28	2·22	2·18	2·10	2·03	1·94	1·90	1·85	1·81	1·75	1·70	1·64
30	4·17	3·32	2·92	2·69	2·53	2·42	2·33	2·27	2·21	2·16	2·09	2·01	1·93	1·89	1·84	1·79	1·74	1·68	1·62
40	4·08	3·23	2·84	2·61	2·45	2·34	2·25	2·18	2·12	2·08	2·00	1·92	1·84	1·79	1·74	1·69	1·64	1·58	1·51
60	4·00	3·15	2·76	2·53	2·37	2·25	2·17	2·10	2·04	1·99	1·92	1·84	1·75	1·70	1·65	1·59	1·53	1·47	1·39
120	3·92	3·07	2·68	2·45	2·29	2·17	2·09	2·02	1·96	1·91	1·83	1·75	1·66	1·61	1·55	1·50	1·43	1·35	1·25
∞	3·84	3·00	2·60	2·37	2·21	2·10	2·01	1·94	1·88	1·83	1·75	1·67	1·57	1·52	1·46	1·39	1·32	1·22	1·00

$F = \dfrac{s_1^2}{s_2^2} = \dfrac{S_1}{\nu_1} \Big/ \dfrac{S_2}{\nu_2}$, where $s_1^2 = S_1/\nu_1$ and $s_2^2 = S_2/\nu_2$ are independent mean squares estimating a common variance σ^2 and based on ν_1 and ν_2 degrees of freedom, respectively.

Appendix B. *t*-distribution table

Student's t Distribution Table

For example, the t value for 18 degrees of freedom is 2.101 for 95% confidence interval (**2-Tail** $\alpha = 0.05$).

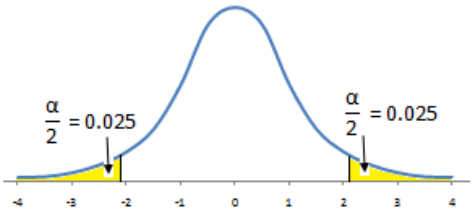

	90%	95%	97.5%	99%	99.5%	99.95%	1-Tail Confidence Level
	80%	90%	95%	98%	99%	99.9%	2-Tail Confidence Level
	0.100	0.050	0.025	0.010	0.005	0.0005	1-Tail Alpha
df	0.20	0.10	0.05	0.02	0.01	0.001	2-Tail Alpha
1	3.0777	6.3138	12.7062	31.8205	63.6567	636.6192	
2	1.8856	2.9200	4.3027	6.9646	9.9248	31.5991	
3	1.6377	2.3534	3.1824	4.5407	5.8409	12.9240	
4	1.5332	2.1318	2.7764	3.7469	4.6041	8.6103	
5	1.4759	2.0150	2.5706	3.3649	4.0321	6.8688	
6	1.4398	1.9432	2.4469	3.1427	3.7074	5.9588	
7	1.4149	1.8946	2.3646	2.9980	3.4995	5.4079	
8	1.3968	1.8595	2.3060	2.8965	3.3554	5.0413	
9	1.3830	1.8331	2.2622	2.8214	3.2498	4.7809	
10	1.3722	1.8125	2.2281	2.7638	3.1693	4.5869	
11	1.3634	1.7959	2.2010	2.7181	3.1058	4.4370	
12	1.3562	1.7823	2.1788	2.6810	3.0545	4.3178	
13	1.3502	1.7709	2.1604	2.6503	3.0123	4.2208	
14	1.3450	1.7613	2.1448	2.6245	2.9768	4.1405	
15	1.3406	1.7531	2.1314	2.6025	2.9467	4.0728	
16	1.3368	1.7459	2.1199	2.5835	2.9208	4.0150	
17	1.3334	1.7396	2.1098	2.5669	2.8982	3.9651	
18	1.3304	1.7341	2.1009	2.5524	2.8784	3.9216	
19	1.3277	1.7291	2.0930	2.5395	2.8609	3.8834	
20	1.3253	1.7247	2.0860	2.5280	2.8453	3.8495	
21	1.3232	1.7207	2.0796	2.5176	2.8314	3.8193	
22	1.3212	1.7171	2.0739	2.5083	2.8188	3.7921	
23	1.3195	1.7139	2.0687	2.4999	2.8073	3.7676	
24	1.3178	1.7109	2.0639	2.4922	2.7969	3.7454	
25	1.3163	1.7081	2.0595	2.4851	2.7874	3.7251	
26	1.3150	1.7056	2.0555	2.4786	2.7787	3.7066	
27	1.3137	1.7033	2.0518	2.4727	2.7707	3.6896	
28	1.3125	1.7011	2.0484	2.4671	2.7633	3.6739	
29	1.3114	1.6991	2.0452	2.4620	2.7564	3.6594	
30	1.3104	1.6973	2.0423	2.4573	2.7500	3.6460	